STEATY-STATE SEDIMENTATION OF NON-BROWNIAN PARTICLES WITH FINITE REYNOLDS NUMBER

Esa Kuusela

Laboratory of Physics
Helsinki University of Technology
Espoo, Finland

Dissertation for the degree of Doctor of Science in Technology to be presented with due permission of the Department of Engineering Physics and Mathematics, Helsinki University of Technology for public examination and debate in Auditorium E at Helsinki University of Technology (Espoo, Finland) on the 26th of April, 2005, at 12 o'clock noon.

Dissertations of Laboratory of Physics, Helsinki University of Technology
ISSN 1455-1802

Dissertation 131 (2005):
Esa Kuusela: Steady-State Sedimentation of Non-Brownian Particles with Finite Reynolds Number
ISBN 951-22-7621-6 (print)
ISBN 951-22-7622-4 (electronic)

OTAMEDIA OY
ESPOO 2005

Abstract

The sedimentation of non-Brownian particles has been studied extensively, both experimentally and through computer simulations. Currently there is quite a good understanding of statistical properties of sedimentation of spherical particles under low Reynolds number conditions. The research of the effects of finite Reynolds number is, however, quite limited.

The aim of this thesis is to study the significance of inertial effects in steady state sedimentation under conditions where the particle size based Reynolds number is small but significant. The known analytical results for single or few sedimenting bodies show that the inertial effects affect some quantities only by an additional correction term that is proportional to the Reynolds number. There are, however, certain type of interactions that entirely vanish in the zero Reynolds number limit.

In this thesis the many-body sedimentation is studied by numerical simulations. From the large variety of possible simulation techniques an immersed boundary method has been used since it allows the study of finite Reynolds number sedimentation efficiently and does not restrict the shape of the suspended particles. The method is based on solving the partial differential equations governing the time evolution of the continuum fluid phase. The embedded solid particles are not treated by explicite boundary conditions but by introducing an equivalent force density to the fluid.

First, we study the case of spherical particles in a system with periodic boundaries in all directions. We show that the velocity distribution of the particles is non-Gaussian and explain this as an effect arising from the local fluctuations in the density of the suspension. Next, we consider the effect of system size by confining the suspension in one horizontal dimension by solid walls. We show the effect of the wall to the particle density and discuss how the system size affects the velocity fluctuations. Finally we consider the sedimentation of spheroidal particles where the orientation of the particles plays an important role altering the average sedimentation velocity significantly from the one measured for spherical particles. We show a transition in the orientational behavior of the spheroids when the volume fraction of the particles is increased and show how it depends on the Reynolds number. This transition is also connected to observed increase in the density fluctuations.

Preface

This thesis has been prepared in the Laboratory of Physics at the Helsinki Institute of Technology. I'm very grateful for my supervisor Prof. Tapio Ala-Nissilä for the guidance and support during the whole process. He and Prof. Risto Nieminen have both been very forbearance concerning the slow progress of the research. I would also like to thank Dr. Stefan Schwarzer who was the third vital person concerning the research reported here. His help with the simulation methods was indispensable and I'm equally grateful for his effort to explain me the basic concepts about the sedimentation.

Many others have contributed to the work too. I would like to thank first Dr. Jukka Lahtinen with whom I have published the majority of the work presented here. I'm also very grateful to Dr. Kai Höfler. Prof. Levent Kurnaz and Prof. Kari Laasonen were kind enough to do the pre-examination of this thesis and I greatly appreciate their constructive comments. I would also like to give my special thanks to Prof. Juhani von Boehm for his comments concerning the classical hydrodynamics. Unfortunately I have no space here to thank all the current and former colleagues by name but I would like to mention especially current and former roommates Dr. Sami Majaniemi, Dr. Jarkko Heinonen, Dr. Marko Rusanen, MSc Mika Jahma, MSc Sampsa Jaatinen, and MSc A-P Hynninen for the great company. Finally I would like thank all the referees of the articles presented here.

Financial support from Finnish Cultural Foundation and Magnus Ehrnrooth Foundation is acknowledged. I would also like to thank the resources given to me by the Finnish IT Center for Science and by the Institute of Computer Applications, University of Stuttgart.

Finally I would like tho thank my wife Katriina, and my parents Eeva and Jokke, and also Leena for all the encouragement and support. And my brothers Kalle, Olli, and Antti for helping me to keep feet on the ground.

Espoo, April 2005

Esa Kuusela

Contents

List of Publications

This thesis consists of an overview and the following publications:

1. E. Kuusela and T. Ala-Nissilä, *"Velocity correlations and diffusion during sedimentation",* Phys. Rev. E **63**, 061505 (2001).

2. E. Kuusela, K. Höfler, and S. Schwarzer, *"Computation of particle settling speed and orientation distribution in suspensions of prolate spheroids",* J. Eng. Math. **41**, 221 (2001).

3. E. Kuusela, J.M. Lahtinen, and T. Ala-Nissilä, *"Collective effects in settling of spheroids under steady-state sedimentation",* Phys. Rev. Lett. **90**, 094502 (2003).

4. E. Kuusela, J.M. Lahtinen, and T. Ala-Nissilä, *"Origin of non-Gaussian velocity distributions in steady-state sedimentation",* Europhys. Lett. **65**, 13 (2004).

5. E. Kuusela, J.M. Lahtinen, and T. Ala-Nissilä, *"Sedimentation dynamics of spherical particles in confined geometries",* Phys. Rev. E **69**, 066310 (2004).

The author has had an active role in all stages of the research work reported in this thesis. He has been involved to the development of the used simulation methods. He has performed all the numerical simulations in publications 1-3, and most of the simulations in publication 5. He has performed all the numerical analysis in publications 1-4 and most of the analysis in publication 5. The author has written publications 1,3,4,5 and contributed actively to the writing of the publication 2.

Chapter 1

Introduction

Sedimentation is a process that occurs in a mixture of liquid and solid granular matter when the two phases have different densities and thus the gravity force drives one phase relative to the other. For example, as shown in Fig. 1.1, if fine grained sand is added to a water container and the container is first shaken vigorously and then left intact, the sand grains start to sedimentate to the bottom of the container. It is characteristic to sedimentation that the single settling particles influence the motion of each other since the surrounding fluid disperses their momentum far away from them.

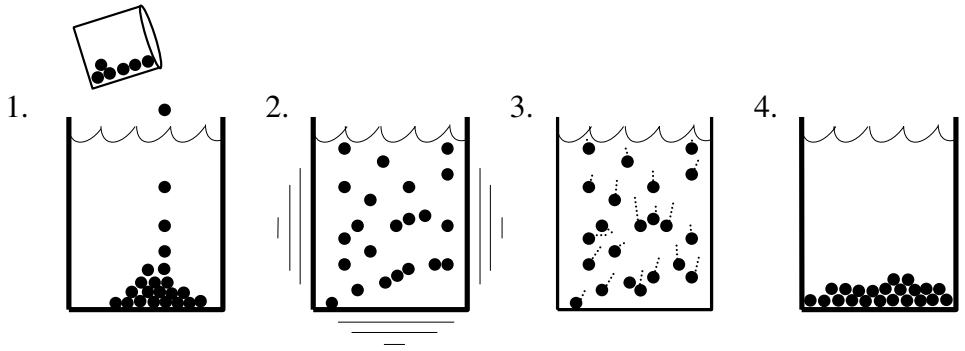

Figure 1.1: A cartoon description on sedimentation: (a) a mixture of solid particles and fluid, (b) after vigorous shaking a homogeneous suspension is obtained, (c) from this intial configuration sedimentation starts and continues until (d) all particles rest in the bottom of the container.

The sedimentation process is common in nature and it affects *e.g.* the formation of geological structures and the migration of biological matter in water systems. It is also used in many industrial processes as ore beneficiation [178] and waste water treatment [163]. Sedimentation rate is used to measure the properties of the sedimenting matter *e.g.* the size distribution of granular matter [4] or to detect several deceases from the human blood [82].

The sedimentation process requires very low level of technology. Still it provides easy method to study the properties of suspension or to separate different compounds of granular matter. It is thus understandable that sedimentation has a long history as an object of laboratory and theoretical research [39, 148] and in certain conditions its statistical properties are understood quite well [127]. In most of the cases the phenomenon is not, however, understood in detail (such as in the case of non-spherical particles). It is thus possible that the sedimentation process has a vast unused potential.

The reason for the lack of theoretical understanding of sedimentation process is, in great part, the complexity of the problem which makes analytical approaches unfruitful in all but the most simple cases [10]. Recently, the increase of computational capacity and the development of novel numerical techniques has made it possible to tackle these kind of problems also through computer simulations.

To put the sedimentation into a larger context of physical phenomena we can consider it as a certain process that occurs in a suspension *i.e.* in a mixture of fluid and solid matter. If the densities of the two phases are matched gravity does no work on the system and it is possible to obtain equilibrium condition, where the motion of the suspended particles is created by thermal fluctuations of the fluid and the statistical properties of the particle distribution are same as in the equilibrium conditions of molecules in simple hard sphere liquids [20, 67]. Naturally, the equilibrium of the neutral suspension can be distorted in other ways *e.g.* by imposing a flow to the fluid. The way how the suspension react to these distortions is studied in *rheology,* where the goal is often to try to understand the suspension as a new form of continuum matter, where the embedded solid particles alter the macroscopic properties of the original fluid phase [40, 134].

In this work we will, however, concentrate on the case where the density of the solid phase is larger than the density of the fluid phase and no other

forces are driving the system. Further, we restrict to study systems where the solid particles are non-Brownian and their Reynolds number is finite but small, and the motion has reached a steady state.

Declaring the particles to be non-Brownian means that the gravity force acting to the particles due to the density difference is so large that the thermal motion of the particles is negligible. In practice this requires that the suspended particles are large enough and bigger than typical colloidal particles.

With a finite Reynolds number (Re) we mean that the inertial effects are important even though the system is evolving slowly. Often sedimentation studies are performed in the limit where the Reynolds number is zero indicating that inertial effects are neglected altogether. In experiments this limit is reached by using very stiff fluid *i.e.* liquid with a large viscosity. Studying this limit is merely a practical choice and does not reflect the importance of zero Reynolds number conditions in real life sedimentation. Quite for the contrary, in many practically important situations the Reynolds number is clearly finite. The complexity of the theoretical description is, however, crucially reduced by the $\mathrm{Re} = 0$ approximation and many works so far have been done in this limit. On the other hand a very large Reynolds number would lead to a turbulent fluid flow around the particles.

Since sedimentation is a non-equilibrium phenomenon the statistical properties of an ensemble of sedimentating systems would in principle depend on the time passed from the initial state of the system. It is, however, possible to adjust the system so that it reaches a steady-state condition where the time dependence disappears. In practice steady-state is reached in fluidization experiments [59], where the average downward motion of the particles is compensated by upward fluid flow. In computer simulations it is also possible to use periodic boundary conditions in the direction of gravity.

To begin our theoretical study on sedimentation we need to describe the sedimentation in more exact way. Our aim is to construct a model that could be used to produce numerical simulations about the sedimentation dynamics of a given particle configuration. To obtain the statistical properties of the steady state sedimentation, we could then choose one initial configuration (or several configurations with same conserved quantities, such as the particle number), then let it evolve to steady state, and finally calculate a time average of the desired quantity. On the other hand we are also seeking general understanding about the interaction effects in these interacting

many-particle systems.

Since we are restricted to study the suspension of non-Brownian particles it is possible to build our physical model by using a continuum approximation for the fluid, which means that the molecular fine structure of the fluid is neglected and the macroscopic properties are described directly by equations of state. We give a brief review of this traditional approach in Chapter 2. In the center of the continuum description is the partial differential Navier-Stokes equation that describes the local conservation of momentum. The presence of embedded solid bodies is taken account by appropriate boundary conditions [112]. This description makes the basis of our simulation method but unfortunately the analytical solutions of the Navier-Stokes equation are very rare even though it has been under active study for a very long time [111]. Now the benefit of studying zero Reynolds number becomes evident since in this limit the Navier-Stokes equation is reduced to a much simplified form and the interaction between moving solid body (with high degree of symmetry) and the fluid can be solved analytically. Our strategy to get theoretical understanding of the sedimentation in low Reynolds number conditions is to start from the zero Re case and then study the influence of the inertial effects. Thus in Chapter 2 we have also listed some of the most important results in the zero Re limit concerning the hydrodynamic interactions between few solid bodies. Usually these results are valid with small corrections also in the case where Reynolds number is finite but small, but there are also some new phenomena.

In this work we are restricted to study *monodisperse* sedimentation where, in contrast to the polydisperse sedimentation, all suspended particles are equal in size and shape. Thus in addition to the material parameters the only parameter we need to characterize the suspension is the *volume fraction* which describes the proportion of the total volume occupied by the particles. In addition the statistical properties of sedimentation could depend on the dimensions of the container. In Chapter 3 we will review the previous theoretical and experimental works related to the most important statistical properties of sedimentation, such as the particle velocity distributions (particularly the first few moments such as the average sedimentation velocity and average velocity fluctuations), and the spatial distribution of the particles. Majority of the work is done in the limit where inertial effects are not important.

In Chapter 4 we give a review about the simulation methods suitable to study sedimentation. Some of the methods are based to the continuum

description explained in Chapter 2. In such methods the crucial question is usually how to deal with the boundary conditions between the fluid and the solid bodies. Other type of methods are based on the molecular structure of the fluid or to kinetic descriptions. In all cases the essential part of the method is the conservation of momentum. We will also describe in detail the immersed boundary kind of method that we have used in our simulations. The central idea in the method is to circumvent the need to fulfill the boundary conditions explicitly by forcing the fluid to move like rigid bodies in the interior of the particles. The method makes it possible to implement arbitrary shaped suspended particles.

Finally, in Chapter 5 we present our most important results. We have studied the particle velocity distributions of spherical particles in a system with periodic boundaries in all directions, and we have also systematically considered the effect of the system size if the suspension is confined in one direction between two parallel walls. We have also studied the sedimentation of spheroidal particles where the changing orientation of the particles makes an additional effects to the particle velocity distributions and spatial distributions as well.

We will show that in the case of spherical particles the finite Reynolds number alters the spatial structures of the steady-state. This is seen both in the pair distribution function of spheres in fully periodic system and in the particle density differences in the vicinity of a solid container wall, and it also affects the average sedimentation rate. A more detailed study of the particle velocity distribution reveals that the velocity fluctuations are non-Gaussian which can be explained as the effect of the particle density in the local neighborhood of a test particle. In the confined geometry we report how the velocity fluctuations depend on the the different dimensions of the system size. We studied also the velocity autocorrelation function and the diffusive motion of the sedimenting particles in a two-dimensional simulation.

In the case of spheroidal particles we show how the previously observed anomalous behavior of the average sedimentation velocity of prolate spheroids can be explained by the observed changes in the orientation distribution and the pair correlation function. We will explain the transition in the orientation transition and show how it scales as the function of the Reynolds number. We will also give an explanation for the observed pair correlation function that is valid in a system with finite Reynolds numbers. We will also study the effect of the shape of the spheroid and give results for oblate

spheroids.

To summarize, this work contains studies of monodisperse sedimentation in the limit where thermal motion is negligible and the inertial effects are small but not omitted. We have implemented a numerical method that is capable to model sedimentation of spheroidal particles. Our main conclusions are that finite Reynolds number affects the sedimentation in ways that cannot be considered just as small corrections. Also, we show that the sedimentation of non-spherical particles will alter the picture significantly and explain the behavior of a suspension of spheroidal particles under sedimentation.

Chapter 2

Fluid dynamics

Unlike in dry granular media where direct interparticle collisions dominate the physical processes, in suspension the dynamics of the fluid produces a long-range interaction between the suspended particles and thus dominates the process. Since the scope of this thesis is to study macroscopic, non-colloidal suspended bodies, it is reasonable to use classical continuum description for the fluid. In this chapter the basic concepts of continuum fluid mechanics are presented. In particular, we will discuss the behavior of an immersed rigid body and the hydrodynamic interaction between several bodies. The criterion for the use of a continuum description of the fluid is also discussed.

2.1 Newtonian fluid

In the continuum limit it is assumed that the myriad microscopic degrees of freedom of the fluid molecules can be reduced to only few slowly varying fields describing the collective motion of the fluid molecules around a given location. This is rationalized by assuming that the fast molecular-scale processes will drive a non-equilibrium system instantaneously to local equilibrium and the only thing left is the slow evolution of the conserved quantities such as energy, momentum and mass [150]. The spatial distributions of these quantities are described by fields such as pressure p, velocity $\mathbf{u}$ and temperature and their evolution is governed by *the balance equations.* The details of the molecular interactions, which in the first hand do determine the behavior of the matter, are confined to *the equations of state* and

to the *transport coefficients*. The equations of state define how the stress $\boldsymbol{\sigma}$ and the density ρ_l of the fluid depend on the fields [112].

The balance equation for mass is obtained by noting that since mass cannot be created or destroyed the change rate of mass inside any volume has to be equal to the mass flux through the surface of that volume. This leads to *the equation of continuity* [112]

$$\frac{\partial \rho_l}{\partial t} + \nabla \cdot (\rho_l \mathbf{u}) = 0. \tag{2.1}$$

We will now assume that fluid density ρ_l is simply a constant and does not depend on pressure. For incompressible fluid Eq. (2.1) can be simplified to a form

$$\nabla \cdot \mathbf{u} = 0. \tag{2.2}$$

Before writing the balance equation for the momentum we have to define the stress tensor $\boldsymbol{\sigma}$. Intuitively the difference between a fluid and a solid matter is that in fluid the stress depends on the rate of deformation, not the deformation itself. In the scope of this work it is enough to study the most simple fluid, *the Newtonian fluid*, for which the equation of state describing the stress tensor is [112]

$$\boldsymbol{\sigma} = -p\mathbf{1} + \eta\left(\nabla\mathbf{u} + \nabla\mathbf{u}^T\right) + \left(\zeta - \eta\frac{2}{3}\right)\mathbf{1}(\nabla \cdot \mathbf{u}), \tag{2.3}$$

where $\mathbf{1}$ is the second rank unit tensor and $\nabla\mathbf{u}^T$ describes the transpose of $\nabla\mathbf{u}$[112]. For Newtonian fluid the ratio between stress and the deformation rate, *the viscosity* (one of the transport coefficients) η is assumed to be a constant. For a real fluid, η would be a function of p and temperature. Also non-linear terms would be present. In many cases, however, these effects are small enough that the fluid can be considered as Newtonian. For incompressible fluid the last term of the rhs. of Eq. (2.3) vanishes and thus *the second viscosity coefficient* ζ does not affect the stress.

Once the form of $\boldsymbol{\sigma}$ is chosen, the equation of motion for the fluid, *i.e.* the balance equation for momentum, can be written as [164]

$$\rho_l \frac{D\mathbf{u}}{Dt} = \nabla \cdot \boldsymbol{\sigma} + \rho_l \mathbf{f}. \tag{2.4}$$

Here $\mathbf{f}$ is the external force field acting on the fluid. We have now made an further assumption that the temperature varies slowly enough that thermal

convection does not occur. The time derivative of $\mathbf{u}$ is material *i.e.* it is written for a certain fluid element. It is usually, however, more convenient to write Eq. (2.4) in a laboratory coordinates. By combining Eq. (2.3) and Eq. (2.4) we get

$$\frac{\partial \mathbf{u}}{\partial t} + (\mathbf{u} \cdot \nabla)\mathbf{u} = -\rho_l^{-1}\nabla p + \frac{\eta}{\rho_l}\nabla^2\mathbf{u} + \mathbf{f}, \tag{2.5}$$

which is called the Navier-Stokes equation for incompressible Newtonian fluid.

To complete the equations (2.2) and (2.5) the boundary condition at the interface of the fluid is needed. Usually it is assumed that a *non-slip* boundary condition

$$\mathbf{u}(\mathbf{r}) = \mathbf{v}^b + \boldsymbol{\omega}^b \times (\mathbf{r} - \mathbf{r}^b) \tag{2.6}$$

holds at every point $\mathbf{r}$ that lies on the surface of a rigid body. Here $\mathbf{v}^b$ and $\boldsymbol{\omega}^b$ are the velocity and angular velocity of the body b, and $\mathbf{r}^b$ is the vector pointing to the center of mass of the body [112].

Unfortunately Eq. (2.5) is non-linear. The strength of the non-linearity is described by the dimensionless Reynolds number

$$\mathrm{Re} = \frac{UL\rho_l}{\eta}, \tag{2.7}$$

where U and L denote typical velocity and length scales in the system. Physical interpretation for Re is that it is the ratio between inertia and viscous forces. As long as Re is smaller than a critical Reynolds number $\mathrm{Re}_{\mathrm{cr}}$ the flow field is smooth and no vortices, peculiar to a turbulent flow, are produced. Such a flow is called *laminar.* The value of $\mathrm{Re}_{\mathrm{cr}}$ depends on the actual geometry of the problem but typically $10 \lesssim \mathrm{Re}_{\mathrm{cr}} \lesssim 100$ [112].

If $\mathrm{Re} \ll 1$ the non-linear term from Eq. (2.5) can be neglected and the equation is simplified to the *Stokes' equation*

$$\eta\nabla^2\mathbf{u} = \nabla p - \rho_l\mathbf{f}. \tag{2.8}$$

This simplification means that no inertial effects are taken account. Actually, discarding the partial derivative of the velocity field requires also that the equation is used only to systems where the ratio between the smallest relevant time scale and the time scale where bodies have moved about their diameter is much larger than the Reynolds number. Otherwise the first

term on the lhs. of Eq. (2.5) cannot be neglected. Equation (2.8) is also called *quasi-static* to underline that velocities are directly adjusted to the interaction.

In the scope of this work we are dealing with systems with $\mathrm{Re} > 0$. The quasi-static limit, however, is the starting point for most analytical work related to sedimentation of a single particle or particle suspension. Also, most numerical work is done in the low Re limit.

Equation (2.8) has a couple of properties that are important to note when discussing sedimentation. As already mentioned, the equation is linear. The other property is that it is invariant under time reversal, if also the pressure gradient is reversed. In many cases this simple property is all that is needed to derive the hydrodynamic interaction between particles.

2.2 Suspended particle

Under the assumption that the continuum description holds, a rigid body suspended into the fluid is treated as a new boundary condition to it. In principle, the interaction between the fluid and a solid body can be calculated by first solving the stress tensor of the fluid in the presence of all boundary conditions - and initial conditions - and then calculating the total force and torque acting on the body at the time by considering the interaction of stress to a solid wall and integrating over the whole surface of the body.

In this section we discuss first the solution of a single particle in an unbounded fluid. Analytic solution is obtainable in the quasi static limit. Then we consider the interactions between several suspended bodies and finally dicuss the effects of a finite, but small, Reynolds number.

2.2.1 Analytic solution

In order to simplify the problem, we first assume that the fluid, in which the particle is suspended, is not otherwise bounded *i.e.* all space, except the interior of the particle, is occupied by the fluid. We further assume that the ambient fluid velocity $\mathbf{u}^{\infty}(\mathbf{x})$ describing the flow far away from the

immersed body can be written in the form

$$\mathbf{u}^{\infty}(\mathbf{x}) = \mathbf{v}^{\infty} + \boldsymbol{\omega}^{\infty} \times \mathbf{x} + \mathbf{E}^{\infty} \cdot \mathbf{x}, \tag{2.9}$$

where $\mathbf{v}^{\infty}$ is a constant ambient velocity. Similarly, $\boldsymbol{\omega}^{\infty}$ and $\mathbf{E}^{\infty}$ are the antisymmetric and symmetric second rank tensors defining a constant rotation and shear rate, respectively.

Without the presence of any solid body $\mathbf{u}^{\infty}(\mathbf{x})$ would give the velocity of the fluid everywhere. Inducing the new boundary condition the flow pattern will be changed and new velocity field can be expressed as

$$\mathbf{u}(\mathbf{x}) = \mathbf{u}^{\infty}(\mathbf{x}) + \mathbf{u}^{D}(\mathbf{x}), \tag{2.10}$$

where $\mathbf{u}^{D}(\mathbf{x})$ is the disturbance field due to the interaction of the solid body. Once the stress tensor $\boldsymbol{\sigma}$ is known, the hydrodynamic drag force produced by the fluid flow to a rigid suspended particle can be calculated with formula

$$\mathbf{F}^{\mathrm{h}} = \oint_S (\boldsymbol{\sigma} \cdot \hat{\mathbf{n}}) dS, \tag{2.11}$$

where the integral is taken over the surface of the solid body and $\hat{\mathbf{n}}$ is the surface normal pointing outward from the body [93]. Similarly, the torque acting to a suspended body is

$$\boldsymbol{\tau}^{\mathrm{h}} = \oint_S (\mathbf{r} - \mathbf{r}^{b}) \times (\boldsymbol{\sigma} \cdot \hat{\mathbf{n}}) dS. \tag{2.12}$$

In the quasi-static limit the inertial force is neglected and the sedimenting bodies are assumed to instantaneously adjust their motion so that the external force $\mathbf{F}^{\mathrm{ext}}$ and torque $\boldsymbol{\tau}^{\mathrm{ext}}$ matches $\mathbf{F}^{\mathrm{h}}$ and $\boldsymbol{\tau}^{\mathrm{h}}$. By considering the motion of a single body in an ambient flow $\mathbf{u}^{\infty}(\mathbf{x})$ we can either solve the motion if we know the external force acting on the particle (mobility problem) or the external force needed to produce the known motion (resistance problem).

We next consider a point-like force acting to an unbounded Newtonian fluid under the quasi-static approximation where the velocity and pressure fields satisfy Eq. (2.8) and (2.2). The former becomes

$$\nabla \cdot \boldsymbol{\sigma} = -\nabla p + \mu \nabla^2 \mathbf{u} = -\mathbf{F}\delta(\mathbf{x}), \tag{2.13}$$

where the location where the force $\mathbf{F}$ is acting has been chosen to the origin and $\delta(\mathbf{x})$ is Dirac's delta function. The solution for this problem is well-known:

$$\mathbf{u}^D(\mathbf{x}) = \mathbf{F} \cdot \frac{\mathcal{G}(\mathbf{x})}{8\pi\mu}, \tag{2.14}$$

where the *Oseen tensor* $\mathcal{G}(\mathbf{x})$ has the form

$$\mathcal{G}_{\alpha\beta}(\mathbf{x}) = r^{-1}\delta_{\alpha\beta} + r^{-3}x_\alpha x_\beta. \tag{2.15}$$

Here r is the distance between point $\mathbf{x}$ and the origin[93]. This solution is also known as the *Stokeslet*. The most remarkable fact is that the velocity of the fluid motion created by the point force decays as $1/r$.

The velocity field created by an arbitrary shaped rigid body can in principle be treated as a distribution of stokeslets

$$\mathbf{u}^D(\mathbf{x}) = \oint_S \mathcal{G}(\mathbf{x} - \boldsymbol{\xi})\mathbf{f}_{\text{ind}}(\boldsymbol{\xi})d\boldsymbol{\xi}, \tag{2.16}$$

where the induced force field $\mathbf{f}_{\text{ind}}$ is defined so that the no-slip boundary condition is satisfied (*i.e.* $\mathbf{u}^D(\mathbf{x}) + \mathbf{u}^\infty(\mathbf{x})$ satisfies Eq. (2.6)). It is now possible that either the translational and rotational motion of the body is known (the resistance problem), or instead the total force and torque acting to the body are known (the mobility problem)[93].

In the general case the velocity field created by this distribution can be treated as a multipole expansion by expanding $\mathcal{G}(\mathbf{x} - \boldsymbol{\xi})$ around the center of mass of the particle, similar to the case of an electric field created by a charge distribution. The coefficient of the first multipole field is the total hydrodynamic force given by Eq. (2.11) and, in the mobility problem, should be matched to $\mathbf{F}^{\text{ext}}$. The velocity field generated by the first term corresponds the Stokeslet solution and decays as r^{-1}. Similarly the anti-symmetric part of the coefficient of the second term should be matched by $\boldsymbol{\tau}^{\text{ext}}$ and the contribution to $\mathbf{u}^D(\mathbf{x})$ decays as r^{-2}[93].

The multipole expansion is not very useful to describe the velocity field around an arbitrary shaped particle due to the slow convergence of the multipole terms. However, since velocity field produced by the nth term from the multipole expansion decays as r^{-n}, the fluid field far away from the particle can be described by a reasonable accuracy by the first few terms. For particles with high symmetry the multipole expansion can be truncated

after a few terms. Next, we will give some well known results for certain types of bodies with a high degree of symmetry.

For spherical particles, with radius a, the velocity disturbance is given by the Rotne-Prager tensor[153]

$$\mathcal{G}^{\mathrm{RP}}_{\alpha\beta} = r^{-1}\delta_{\alpha\beta} + r^{-3}x_\alpha x_\beta + \frac{2a^2}{3r^3}\left(\delta_{\alpha\beta} - r^{-3}x_\alpha x_\beta\right), \tag{2.17}$$

which can be put into Eq. (2.14) (to replace the Oseen tensor) to obtain the velocity disturbance field around the sphere. Correspondingly, $\mathbf{F}^{\mathrm{h}}$ generated by an arbitrary velocity field $\mathbf{u}^\infty(\mathbf{x})$ to the sphere is[93]

$$\mathbf{F}^{\mathrm{h}} = (1 + \frac{a^2}{6}\nabla^2)\mathbf{u}^\infty(\mathbf{x}), \tag{2.18}$$

which is known as the Faxen law.

The force and torque on a sphere with velocity $\mathbf{v}$ and angular velocity $\boldsymbol{\omega}$ are given by [93]

$$\mathbf{F}^{\mathrm{h}} = -6\pi\mu a(\mathbf{v}^\infty - \mathbf{v}); \tag{2.19}$$

$$\boldsymbol{\tau}^{\mathrm{h}} = 8\pi\mu a^3(\boldsymbol{\omega}^\infty - \boldsymbol{\omega}). \tag{2.20}$$

Having the sedimentation problem in mind, it is important to find out the terminal velocity of a sphere with $\mathbf{u}^\infty = 0$. Thus we have a mobility problem with $\mathbf{F}^{\mathrm{ext}}$ as the gravity force of the buoyant mass of the body. Based on the previous result we get

$$V^a_\parallel = \frac{2}{9}\Delta\rho a^2 g\mu^{-1}, \tag{2.21}$$

where $\Delta\rho = \rho_p - \rho_f$ is the difference between the density of the body and the fluid, and g is the gravity coefficient. The subscript in $V^a_\parallel$ denotes that the terminal velocity is in the direction of gravity and the superscript that the velocity is calculated for a sphere with radius a. For spherical particles the terminal velocity is also called the *Stokes* velocity and is denoted by V_s.

For a spheroid, a body of revolution that is obtained by rotating an ellipse around its large (prolate spheroid) or small major axis (oblate spheroid), the force and torque depend also on the orientation relative to the direction of the motion. If $\mathbf{d}$ denotes the unit vector pointing to the direction of the

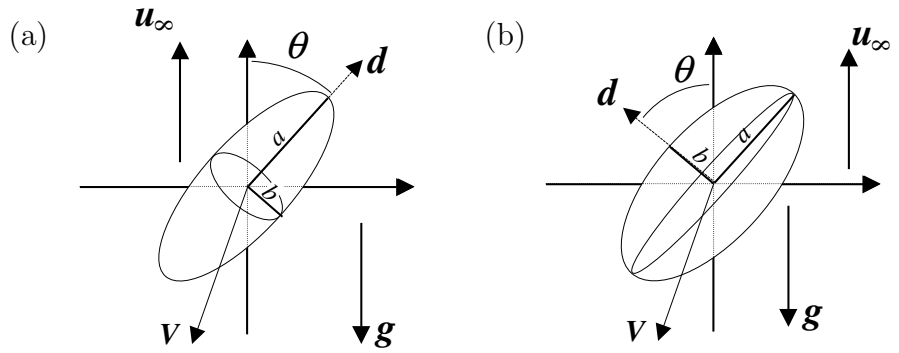

Figure 2.1: The orientation of (a) a prolate and (b) an oblate spheroid. The orientation is defined by the direction of the axis of revolution (**d**). Aspect ratio a_r is defined as the ratio between large and small radius.

axis of revolution (see Fig. 2.1), the resistance functions, for both prolate and oblate spheroid, are of the form[93]

$$F_\alpha = 6\pi\mu a[\mathcal{X}^A d_\alpha d_\beta + \mathcal{Y}^A(\delta_{\alpha\beta} - d_\alpha d_\beta)](\mathbf{v}_\beta^\infty - \mathbf{v}_\beta) \tag{2.22}$$

$$\tau_\alpha = 8\pi\mu a^3[\mathcal{X}^C d_\alpha d_\beta + \mathcal{Y}^C(\delta_{\alpha\beta} - d_\alpha d_\beta)](\boldsymbol{\omega}_\beta^\infty - \boldsymbol{\omega}_\beta) - 8\pi\mu a^3 \mathcal{Y}^H \varepsilon_{\alpha\beta\lambda} d_\lambda d_\kappa E_{\kappa\lambda}^\infty, \tag{2.23}$$

where we have used the Einstein summing convection and $\varepsilon_{\alpha\beta\lambda}$ is the Levi-Civita tensor. Here $\mathcal{X}^A$, $\mathcal{Y}^A$, $\mathcal{X}^C$, $\mathcal{Y}^A$ and $\mathcal{Y}^H$ are geometric coefficients depending only on the shape of the spheroid and they are given in Tables 2.1 (for prolate) and 2.2 (for oblate spheroids). The shape is defined by the aspect ratio $a_r = a/b$ which is the ratio between the large and small semi major axes of the spheroid (see Fig. 2.1).

The terminal velocity of spheroidal particles depends also on the orientation of the particle which we now express as an angle θ between the direction of gravity and the axis of symmetry. For a prolate spheroid the terminal velocity is[93]

$$V_\parallel(\theta) = V_\parallel^b \left(\frac{\sin^2\theta}{\mathcal{Y}^A} + \frac{\cos^2\theta}{\mathcal{X}^A} \right); \tag{2.24}$$

$$V_\perp(\theta) = V_\parallel^b \sin\theta\cos\theta(\mathcal{Y}^{A^{-1}} - \mathcal{X}^{A^{-1}}), \tag{2.25}$$

where $V_\parallel^b$ is a terminal velocity of a sphere with radius b. The direction of the component $V_\perp(\theta)$ is perpendicular to the direction of gravity and is in

Table 2.1: The geometric coefficients for prolate spheroid as a function of eccentricity $e = \sqrt{1 - a_r^{-2}}$.[93]

$$
\begin{aligned}
\mathcal{X}^A &= \frac{8}{3}e^3[-2e + (1+e^2)L]^{-1} \\
\mathcal{Y}^A &= \frac{16}{3}e^3[2e + (3e^2-1)L]^{-1} \\
\mathcal{X}^C &= \frac{4}{3}e^3(1-e^2)[2e - (1-e^2)L]^{-1} \\
\mathcal{Y}^C &= \frac{4}{3}e^3(2-e^2)[-2e + (1+e^2)L]^{-1} \\
\mathcal{Y}^H &= \frac{4}{3}e^5[-2e + (1+e^2)L]^{-1} \\
L &= \ln\left(\frac{1+e}{1-e}\right)
\end{aligned}
$$

Table 2.2: The geometric coefficients for oblate spheroid as a function of eccentricity $e = \sqrt{1 - a_r^{-2}}$.[93]

$$
\begin{aligned}
\mathcal{X}^A &= \frac{4}{3}e^3[(2e^2-1)C + e\sqrt{1-e^2}]^{-1} \\
\mathcal{Y}^A &= \frac{8}{3}e^3[(2e^2+1)C - e\sqrt{1-e^2}]^{-1} \\
\mathcal{X}^C &= \frac{2}{3}e^3[C - e\sqrt{1-e^2}]^{-1} \\
\mathcal{Y}^C &= \frac{2}{3}e^3(2-e^2)[e\sqrt{1-e^2} - (1-2e^2)C]^{-1} \\
\mathcal{Y}^H &= -\frac{2}{3}e^5[e\sqrt{1-e^2} - (1-2e^2)C]^{-1} \\
C &= \operatorname{arccot}\left(\frac{\sqrt{1-e^2}}{e}\right)
\end{aligned}
$$

the plane defined by the direction of gravity and the axis of symmetry of the particle. For an oblate spheroid the terminal velocity is[93]

$$V_{\parallel}(\theta) = V_{\parallel}^{b} a_r \left(\frac{\sin^2\theta}{\mathcal{Y}^A} + \frac{\cos^2\theta}{\mathcal{X}^A} \right) \tag{2.26}$$

$$V_{\perp}(\theta) = V_{\parallel}^{b} a_r \sin\theta\cos\theta(\mathcal{Y}^{A^{-1}} - \mathcal{X}^{A^{-1}}), \tag{2.27}$$

where the only difference to the perpendicular case is that the velocity is multiplied by the aspect ratio. It is important to note that for a prolate spheroid the terminal velocity reaches maximum when particle is oriented parallel to the direction of the gravity ($\theta = 0$) and minimum when orientation is perpendicular to it ($\theta = \pi/2$). For an oblate spheroid the situation is reversed. Second, the terminal velocity has a sideward component that is non-zero for all orientations other than $\theta = 0$ or $\theta = \pi/2$.

Another result that we are going to use in the future is the behavior of a freely moving prolate spheroid in a shear flow. Without any loss of generality the shear field can be assumed to have a form $\mathbf{v}^{\infty} = \dot{\gamma} y \hat{\mathbf{e}}_x$, where $\hat{\mathbf{e}}_x$ is a unit vector pointing in the x direction and $\dot{\gamma}$ is a constant describing the strength of the shear field[1]. Now let the orientation of the spheroid be described with angles ϕ and ψ where ϕ is the angle between the z axis and the axis of symmetry of the spheroid, and ψ is the azimuthal angle in the xy plane. If the torque is set to zero and the angular velocity is solved from Eq. (2.23) we get the following results[93]:

$$\dot{\phi} = -\left(\frac{a_r^2 - 1}{a_r^2 + 1} \right) \frac{\dot{\gamma}}{4} \sin 2\phi \sin 2\psi; \tag{2.28}$$

$$\dot{\psi} = -\frac{\dot{\gamma}}{a_r^2 + 1}(a_r^2 \cos^2\psi + \sin^2\psi), \tag{2.29}$$

where $\dot{\phi}$ and $\dot{\psi}$ are the time derivatives of ϕ and ψ. By integrating these equations one get the following equations:

$$\tan\psi = -a_r \tan\left(\frac{\dot{\gamma} t}{a_R + a_r^{-1}} \right); \tag{2.30}$$

$$\tan\phi = \frac{C a_r}{[a_r^2 \cos^2\psi + \sin^2\psi]^{1/2}}, \tag{2.31}$$

which are know as the *Jeffery orbitals*. Here C is a constant depending the initial orientation ϕ and t is the time. It is important to note that the rate of

[1]The shear field can be expressed also in the form $\boldsymbol{\omega}^{\infty} \times \mathbf{x} + \mathbf{E}^{\infty} \cdot \mathbf{x}$.

change of the azimuthal angle is not a constant, except when a_r reaches 1 *i.e.* for a sphere, but has a minimum when the spheroid is oriented with its broad side parallel to x and a maximum when its orientation is perpendicular to it. In other words the prolate spheroid spends most of its time with axis of revolution parallel to the shear flow.

We will close this subsection by emphasizing a couple of properties of the presented resistance functions: (1) the rotation of a settling sphere does not produce any contribution to the drag force and (2) the relative motion $(\mathbf{v}^\infty - \mathbf{v})$ of a spheroidal particle does not produce any contribution to the torque. The consequences are that no lift force occurs to a rotating sphere and for a sedimenting spheroid all orientations are stable. These results are valid only in the Re = 0 limit and could have been obtained also directly from the time-reversal symmetry of the Stokes equation.

2.2.2 Interaction between several bodies

In the presence of several solid bodies, each body produces a velocity field decaying as r^{-1} and thus influences the fluid velocity field at the location of the other particles, and vice versa, creating an effective hydrodynamic interaction between the particles. It is usually meaningful to divide the particle action to a long-range contribution, where only the lowest order terms from the monopole expansion matter, and to a short-range part. Again, there are two ways to consider the interaction. In the mobility picture the particle velocities are calculated based on the known forces and in the resistance picture the forces are calculated based on the known velocities.

Nominally the two-body hydrodynamic interaction can be expressed with a mobility tensor $\mathcal{M}$ or a resistance tensor $\mathcal{R}$:

$$\begin{pmatrix} \mathbf{v}_1 \\ \mathbf{v}_2 \\ \boldsymbol{\omega}_1 \\ \boldsymbol{\omega}_2 \end{pmatrix} = \mathcal{M} \begin{pmatrix} \mathbf{F}_1 \\ \mathbf{F}_2 \\ \boldsymbol{\tau}_1 \\ \boldsymbol{\tau}_2 \end{pmatrix}; \quad \begin{pmatrix} \mathbf{F}_1 \\ \mathbf{F}_2 \\ \boldsymbol{\tau}_1 \\ \boldsymbol{\tau}_2 \end{pmatrix} = \mathcal{R} \begin{pmatrix} \mathbf{v}_1 \\ \mathbf{v}_2 \\ \boldsymbol{\omega}_1 \\ \boldsymbol{\omega}_2 \end{pmatrix}. \tag{2.32}$$

To start the study of the interaction between two rigid bodies at distance R apart, with R much larger than the particle dimensions a, it is first assumed that the second particle is not present. Thus we obtain the disturbance velocity field $\mathbf{u}_1^D(\mathbf{x})$ of the particle 1 by using Eq. (2.14). If we now introduce

the second particle to the system, the total disturbance velocity created by particle 2 is $\mathbf{u}_2^D(\mathbf{x}) + \mathbf{u}_2^{(1)}(\mathbf{x})$, where the first term is the response to the ambient flow and the second to the disturbance field of particle 1. Since the same consideration can be done to particle 1, we need yet another term to take into account $\mathbf{u}_1^{(1)}(\mathbf{x})$ at the surface of particle 2 and so on.

The consequent recursive scheme is called the method of reflections since the n-th contribution $\mathbf{u}_1^{(n)}(\mathbf{x})$ in the disturbance velocity field of particle 1 can be thought to be a reflection of $\mathbf{u}_2^{(n-1)}(\mathbf{x})$. The magnitude of each new term is order $\mathcal{O}(R/a)$ smaller than the previous one[2] and series can be truncated once the desired accuracy is achieved. The reflection terms $\mathbf{u}^{(n)}(\mathbf{x})$ can be calculated relatively simply from a low order multipole expansion and the method is thus suitable to consider the far-field interaction of spheres or spheroids. The method of reflection can also be straightforwardly generalized to a system of more than two particles, where the term $\mathbf{u}_i^{(n-1)}(\mathbf{x})$ of the disturbance field of particle i just generates a reflection for all the other particles.

In the special case of two spheres Jeffrey and Onishi [86] have developed a direct method to generate the two particle hydrodynamic interaction. The basic idea is to do the multipole expansion directly to the pair of particles by using spherical harmonics. With this method it is possible to calculate the interaction also for closely placed pair of particles. Unfortunately the method could not be generalized to consider multi-particle effects and the interactions in a many-body system can only be taken account in the pairwise manner.

For two bodies almost contact, the interaction can be treated using lubrication theory [141, 93]. When the gap between the particle surfaces is much smaller than the particle diameter the interaction is strictly pairwise and the mutual resistance force scales as the inverse of the gap length for particles approaching to each others. For particles moving in such a manner that the gap length does not change the force scales as the logarithm of the inverse gap length. This diverging short range lubrication force would, according to the continuum approximation of the fluid, prevent particles from ever making contact. We want to note that here the continuum model breaks down once the gap between the particles is in the order of fluid molecule size and in molecular dynamic simulations the divergence force has not been

[2]In mobility problem each term is order $\mathcal{O}((R/a)^3)$ smaller than the previous one since the total force and torque created by each term has to vanish.

found [169].

Another type of interaction considered here is between a solid wall and a particle. Such an interaction is present in all real containers. In principle this can be considered in a same manner than the interaction between two particles. Such consideration could be, however, hard except in certain cases. Beenakker and Mazur [13] considered sedimentation of spherical particles in a spherical container, where the interaction of the particles with the container was modeled just as the interaction between two spherical particles. Here we will restrict our discussion to the case between a particle and an infinite plane wall with the absence of ambient flow relative to the wall. In such a system Blake [17] solved the disturbance field created by the particle by assuming an image force on the other side of the wall pointing to the opposite direction and by inducing an additional correction to satisfy the no-slip boundary condition at the wall. The main results were that no force perpendicular to the wall is present and that the velocity field produced by the particle decays as r^{-2} or faster in distances larger than the particle-wall distance. The presence of the wall will also give an $\mathcal{O}(a/l)$ correction to the hydrodynamic force acting to the body. Here l is the distance between the body and the wall. A spherical body that is free to rotate will have the angular velocity [68]

$$\omega = \frac{3v}{32a}\left(\frac{a}{l}\right)^4\left(1-\frac{3a}{8l}\right). \tag{2.33}$$

Liron and Mochon [115] generalized the treatment of Blake to the case of two parallel infinite walls where an infinite set of images is needed to take account the no-slip boundary condition at both walls. Now the disturbance velocity field decays as r^{-2} or faster if the distance r is larger than the distance to the nearest wall.

Periodic boundary conditions, which are often used in simulations, can be treated by assuming that each body is just a representative of an infinite cubic array of bodies and its mobility and resistance can be calculated by the disturbance field of all the images together. This has been done by Hasimoto [69] using Ewald's summation technique.

2.2.3 Finite Reynolds number results

In the case of a small but non-zero Reynolds number the motion of the fluid is still laminar, but the inertial effects will alter the results discussed in the

previous subsection. In most cases there is a small Re dependent correction to the results obtained in the quasi-static limit. There are, however, certain cases where the inertial effects will provide totally new interaction. To our purpose the most important cases are the force acting on a sphere in shear flow, the force between wall and a moving particle and a torque acting to a moving spheroid.

To measure the importance of inertial effects we use the *particle Reynolds number* where the typical length scale is set to a particle dimension (for sphere a radius a) and the typical velocity is set to the terminal settling velocity. In all considerations we are limited to the case where the flow is still laminar *i.e.* no eddies are formed to the wake of the particle. Experimentally the eddy-formation has been found to start once Re_p is greater than $\mathrm{Re}_{\mathrm{cr}}$. At that point, however, many of the theoretical corrections presented here have significant quantitative differences as compared to the experimentally measured results.

The disturbance field

The quasi-static approximation is not valid once the neglected inertial term is comparable with the viscous term in Eq. (2.8). Even if $\mathrm{Re}_p \ll 1$, Eq. (2.8) does not describe the fluid motion correctly further than $r \sim \mathrm{Re}_p^{-1} d$, where d is the typical particle dimension used in the definition of Re_p. Thus, with finite Re_p the velocity field produced by the particle decays as r^{-1} only inside this region and beyond this in the wake of the particle which has a width $\xi \approx \sqrt{yd}/\mathrm{Re}_p$. Here y is the distance from the particle measured directly donwstream. Elsewhere the velocity field decays faster, as r^{-2} [112].

Correction to the hydrodynamic drag force

In the quasi-static limit the transversal and rotational motion of the particles are not coupled, as can be seen in Eq. (2.19) and (2.20). In finite Re_p this is not the case and $\mathbf{F}^{\mathrm{h}}$ can be divided to the drag force, $\mathbf{F}^d$, rising from the translational motion of the particle and the lift force, $\mathbf{F}^{\mathrm{lift}}$, whose origin lies in the circulation. We will first consider the finite Re_p correction to the hydrodynamic drag force. It is customary to write the drag force in the form

$$F^d = \rho_l v^2 A C_d, \tag{2.34}$$

where A is an area of the largest cross-section of the particle perpendicular to the fluid flow and C_d is the *drag coefficient* that depends both on the particle shape and Re_p. If $\mathrm{Re}_p \ll 1$ the drag coefficient is inversely proportianal to Re_p, or to the velocity if other factors determining Re_p are not changed. For example, to a spherical particle the low Re_p limit result for C_d can be derived from Eq. (2.19) and is $6/\mathrm{Re}_p$. A leading correction to this has been calculated by Oseen [68] and is

$$C_d = 6\mathrm{Re}_p^{-1}(1 + \frac{3}{8}\mathrm{Re}_p). \tag{2.35}$$

For a spheroid with axis of symmetry parallel to the flow a similar correction was calculated by Breach [22]. The experimentally measured drag coefficients of a sphere have been found to follow Eq. (2.35) reasonably well as long as $\mathrm{Re}_p < 1$ although the phenomenological relation

$$C_d = 6\mathrm{Re}_p^{-1}(1 + 0.24\mathrm{Re}_p^{0.687}) \tag{2.36}$$

has been found to describe the experiments better [35].

Lift force

A well-known failure of the quasi-static approximation is that the rotation of a moving body does not give any contribution to the hydrodynamic force, as can be seen in Eq. (2.19). This kind of situation can occur if a particle is sedimenting in a flow that has an ambient shear field $\mathbf{u}^\infty = \dot{\gamma} x \hat{\mathbf{e}}_z$ where z is pointing to the direction of the particle motion. We will here present the lift force for a spherical particle in such a geometry as deduced by McLaughlin [125]. For significant lift force to occure it is important that the shear rate is large enough. To describe the importance of the inertial effect raising from the shear flow, the Reynolds number for the shear flow is defined as $\mathrm{Re}_{\dot{\gamma}} = 4\dot{\gamma}a^2\rho_l/\eta$. Now the criterion for a significant lift force to occur is that

$$\epsilon \equiv \frac{\sqrt{\mathrm{Re}_{\dot{\gamma}}}}{\mathrm{Re}_p} \gtrsim 1. \tag{2.37}$$

The inertial effects produce a lift force

$$F^{\mathrm{lift}} = 3.23\eta a v \sqrt{\mathrm{Re}_{\dot{\gamma}}}\frac{J(\epsilon)}{2.255} - \frac{11\pi\eta a v}{32}\mathrm{Re}_{\dot{\gamma}}, \tag{2.38}$$

where J is a known function of ϵ and has value 2.255 in the limit $\epsilon \to \infty$ and decreases rapidly with decreasing ϵ. Thus keeping the shear rate constant and decreasing Re_p will give a finite value of the lift force. As a concequence of the lift force a sphere moving parallel to a plane wall has a force pointing away from the wall.

Torque of a moving spheroid

We will end this subsection by considering the torque acting to a falling spheroid. It is a well known fact that moving spheroid (or any body with fore-aft symmetry) with finite Re_p tends to turn its broad side towards the direction of motion. Resently Galdi and Vaidya [57] have shown that for an off-diagonally falling body of revolution, with fore-aft symmetry, there is a torque acting on it with magnitude

$$\frac{1}{2}\mathrm{Re}v^{(1)}v^{(2)}G \leq 8a^3\rho_l\tau^{\mathrm{GV}} \leq \frac{3}{2}\mathrm{Re}v^{(1)}v^{(2)}G, \tag{2.39}$$

where $v^{(1)}$ and $v^{(2)}$ are the components of the relative velocity in the direction parallel and perpendicular to the long axis. The dimensionless coefficient G depends only on the shape of the body. It is note-worthy that values limiting τ^{GV} are proportional to Re_p. The torque depens also on the orientation of the body and vanishes if the body is parallel or perpendicular to the direction of its motion and has a maximum at certain angle $0 < \theta' < \pi/2$. Using Eqs. (2.24) and (2.25) and by assuming that the correct value of τ^{GV} is around the middle of the limits we get the torque of a freely settling spheroid as

$$\tau^{\mathrm{GV}} \approx \frac{8a^3\rho_l^2(V_\parallel^b)^3G}{\eta}\frac{\sin 2\theta}{2\mathcal{X}^A\mathcal{Y}^A}\sqrt{\frac{\sin^2\theta}{(\mathcal{Y}^A)^2}+\frac{\cos^2\theta}{(\mathcal{X}^A)^2}}. \tag{2.40}$$

According to Galdi and Vaidya the geometric factor G for a prolate spheroid vanishes in the limit of a sphere or a needle-like shape and has maximum around $a_r \sim 1.7$[57].

2.3 The thermal effects

So far we have taken it as granted that the continuum description holds and the thermal effects can be neglected. It is, however, important to note that

this restricts the use of the current description to non-colloidal bodies. In sedimentation the suspended bodies can have a large variety of size. The importance of thermal effects is described by a dimensionless *Péclet* number

$$\mathrm{Pe} = \frac{\hat{\gamma} a^2}{D_{\mathrm{Th}}}, \tag{2.41}$$

where $\hat{\gamma}$ is the typical macroscopic velocity gradient around the particle, a the dimension of the particle and D_{Th} the diffusion coefficient of thermal diffusion of a single embedded body [148]. Using Einstein's relation this can be expressed as $k_B T/\eta$, where T is the temperature of the fluid and k_B is Boltzmann's coefficient. In sedimentation we can assume that the fluid velocity gradient is produced by the settling motion of the body, which is produced by the gravity force. Thus we get $\mathrm{Pe} = m_b g a/k_B T$, where m_b is the buoyant mass of the body. The Péclet number can be considered as a measure of how far away from the equilibrium the system is. The limit $\mathrm{Pe} = 0$ corresponds the situation where no macroscopic velocity gradients are present and dynamics of the system is defined by the equilibrium Brownian motion. Correspondingly $\mathrm{Pe} \to \infty$ corresponds to the situation where the thermal motion is negligible compared to the effect of the non-equilibrium velocity gradient and the system is called non-colloidal. In practice the sedimentation is usually assumed to be non-colloidal if the particle diameter is larger than several tens of micrometers [107].

Chapter 3

Sedimentation of Macroscopic Particles

In the previous chapter we discussed the behavior of a single body (or a single pair of particles) in a fluid. In the present chapter we expand the consideration to a monodisperse sedimentation problem of N identical particles where an external gravity force is driving the particles downwards. Now our focus is on the statistical properties of the suspension *i.e.* the average structure and particle velocities. We give a brief review about the literature and explain the simulation methods that can be used to study sedimentation.

3.1 Particle Suspension

Let us consider the suspension of N solid particles with spatial and orientation co-ordinates $\{\mathbf{r}^i\}$ and $\{\boldsymbol{\zeta}^i\}$, and with transitional and rotational velocities $\{\mathbf{v}^i\}$ and $\{\boldsymbol{\omega}^i\}$. To describe the full microscopic state of this many-body system, we would also need to know the coordinates and velocities of the large number of fluid molecules present. In the absence of external forces or torques acting on the particles and no other macroscopic fluid velocity gradient induced by other boundary conditions, the system will eventually reach an equilibrium state. For such a state the motion of the particles is induced by the thermal motion of the fluid molecules and the statistical properties are independent from the time instant and, assuming ergodicity, they can be calculated as a time average of the system.

For a suspension of identical hard spheres many equilibrium properties are known [67]. Situation changes if, like in sedimentation, external force does work to the system. Then the statistical properties are either time dependent or we achieve a steady state, where mechanical energy flows through the system with a constant rate.

3.1.1 Monodisperse Non-Brownian Sedimentation

With sedimentation we refer to the non-equilibrium process occuring in a mixture of fluid and solid particles in the presence of gravity field $\mathbf{g}$ pointing to the negative z direction. If the density difference between the particle phase and the fluid phase $\Delta\rho$ is positive[1], each particle is influenced by an external force $\mathbf{F}_g = V_{\text{particle}}\Delta\rho\mathbf{g}$, which has been obtained as the difference between the gravity force and the buoyancy force. In this work we are restricted to monodisperse sedimentation, where each particle has the same volume, $V_{\text{particle}} = (4/3)\pi a^3$ where a is the radius of the particle. The more general case where the size of the particles can vary is referred as polydisperse sedimentation [79, 140]. In this work we do not consider the bottom layer eventually formed by the process or the layer formation [123, 100, 124]. Instead we study the complex dynamics the sedimentation itself causes by the long-range many-particle interactions carried by the fluid.

The sedimenting suspension is characterized by the *volume fraction* Φ that is the ratio between the volume occupied by the particles and the total volume of the suspension. Sometimes the particle density is described by the number density $n = \Phi/V_{\text{particle}}$. Another important quantity is the particle Reynolds number which in sedimentation is defined as $\text{Re}_p = V_s a\rho_l/\eta$, where V_s is the terminal velocity of a single sedimenting particle and a is the length scale of the particle (in the case of a sphere the radius). Provided that $\mathbf{F}_g$ is large enough Brownian motion does not affect significantly the particle motion and the Péclet number is very high. Thus thermal motion can be neglected and we can adopt the continuum description of the fluid presented in the previous chapter. Now the microscopic degrees of freedom are averaged over a region so that only the hydrodynamic modes are left from the motion of the fluid molecules. In the quasi static limit it is enough to know the $6N$ particle coordinates. In finite Re_p case the history of the particle motion is encoded into the fluid velocity field.

[1]There is a closely related problem of the dynamics of bubbly flow, where $\Delta\rho$ is negative [43, 26].

In reality the suspension is always bounded and fluid is confined to a solid container. In a cell experiment the container has solid walls with no-slip boundary conditions in all directions, with the possible exception in the top of the container. In such a geometry the sedimentation experiment is typically done by first stirring or shaking the container and then letting the particles to sediment towards the bottom. Another experimental setup is a fluidized bed, where fluid is pumped through the container with a constant flux upward so that the average fluid velocity counters the average sedimentation velocity of the particles. In theoretical considerations it is also possible to study unbounded sedimentation or to use periodic boundaries in some or all spatial directions. The size of the container provides another length scale to the problem and we can define a container Reynolds number that is based on this length scale.

3.1.2 The Steady State

Since sedimentation is a non-equilibrium process, its statistical properties do, in general, depend on the initial conditions and time instant studied. Thus to study such a process we need to consider an ensemble of initial conditions with same statistical properties and consider the averaged quantities of the sedimentation as a functions of time. This kind of situation occurs typically in a cell experiment where the sedimentation process can only occur a limited time until all particles have settled down.

Often the consideration of sedimentation is limited to *steady state conditions* where the statistical properties can be assumed to be independent of time. The steady state conditions can be achieved in a fluidized bed experiment, where it is possible to keep the process continuing for an arbitrary long time and achieve a state where time-averaged statistical properties do not change [66, 42] [2]. In simulations it is also possible to obtain steady state by using periodic boundary conditions in the direction of gravity. It has been also customary to assume that in a cell experiment sedimentation reaches a state that is close enough to steady state [107]. Recently, however, it has been shown that in many cases this is not true [162].

It is important to note that, in principle, the ensemble average should not be calculated over the equilibrium distribution of particle configurations

[2] In fact there is another kind of steady state which can be achieved too, *e.g.* by depositing particles to an open container with a constant rate [124].

in suspension. Rather, each configuration should be taken into account with the weight it appears during the sedimentation process. In this work we have restricted to study the statistical and dynamical processes under steady state sedimentation. We use the angular brackets $\langle\cdot\rangle$ to denote the steady state average properties of the particles. With the corresponding equilibrium state we refer to an otherwise similar system with no external forces.

3.2 Particle Distribution under Sedimentation

Before going to the dynamical properties of sedimentation we will briefly go through what is known about the distribution of the particles undergoing sedimentation. We will first study the pair distribution of the particles and then the particle density in the presence of container walls. Finally, previous studies of the spatial and orientational distributions of elongated particles are reviewed.

3.2.1 Pair Distribution Function

A practical starting point to study the properties of particle configurations is to study the pair distribution function

$$g(\mathbf{r}) = \langle (V/N^2) \sum_{i \neq j} \boldsymbol{\delta}(\mathbf{r} - (\mathbf{r}^i - \mathbf{r}^j)) \rangle, \tag{3.1}$$

where $\mathbf{r}^i$ and $\mathbf{r}^j$ are the positions of particles i and j and the summation goes over all values of i and j, except those with $i \neq j$. The pair distribution function is normalized so that unity corresponds to the average particle density in the suspension with N particles distributed to a volume V.

The equilibrium distribution of hard spheres $g_{eq}(r)$, *i.e.* in a suspension of particles with no density difference to the fluid, is known to follow the Percus-Yevick distribution [135] which approaches $g_0(r) = \theta(2a - r)$ in the low Φ limit. Here $\theta(r)$ is a step function giving value 1 if the argument is negative and 0 otherwise. In many theoretical studies considering steady state sedimentation with $\mathrm{Re}_p = 0$ it has been assumed that the steady state

pair distribution function $g(\mathbf{r})$ equals $g_{eq}(r)$ with reasonable accuracy [10, 107, 70]. There is, however, a theoretical study by Koch and Shaqfeh [95] where a three-body interaction during sedimentation is found to increase the net deficit of other particles around the test particle. Such net excess deficit was not found in the lattice-Boltzmann simulations of over 32 000 hard spheres done by Ladd [107, 108]. Instead Ladd found that with r close to the touching distance of the two spheres, $g_{st}(r)$ has a high but narrow peak which clearly exceeds the equilibrium distribution. Results are quantitatively similar to the Stokes dynamics simulations of colloidal hard spheres under shear flow done by Bossis and Brady [20]. With low Péclet number the measured pair distribution function was similar to $g_{eq}(r)$ but by increasing the shear rate, and thus Pe, a peak grew at distance $r = 2a$.

In the finite Re_p case, Koch has suggested that the two-body hydrodynamic interaction is enough to produce a depletion area to the wake of the test particle [96]: the shear field produced to the wake of the sedimenting test particle causes the following particles to rotate and thus creates a Lift force (Eq. (2.38)) force driving them sidewise away from the wake. Climent and Maxey have shown, in a good agreement with Koch's results, that the sedimenting particles are more evenly distributed during sedimentation if Re_p is increased [36].

3.2.2 The Effects of Walls to the Particle Density

In an infinite suspension the steady state particle density is, for symmetry reasons, uniform. In a finite container the solid walls could affect the particle density. We will next briefly discuss the case of steady state sedimentation with side walls and then go through how the bottom wall changes the situation.

If the suspension is confined by a wall with its normal perpendicular to gravity it has been assumed that the particle density $f(x) = V/N\langle\sum_{i=1}^{N}\delta(x - x^i)\rangle$, where x^i is the distance between particle i and the wall, corresponds again to the equilibrium distribution of hard spheres near a wall [135]. Brenner has also suggested that near a wall there is a region of larger $f(x)$ since the diffusivity of the particles is hindered and the wall is working as a kinetic trap for the spheres [23]. It is worth to note that if the walls are even slightly tilted the situation is very different and the sedimentation is affected by the Boycot effect [39].

The presence of the bottom wall affects the idealized steady state conditions assumed so far. Eventually the system will reach equilibrium with all the particles sedimented to the bottom of the container and it is not clear that system can be considered to be in steady state at any point of the container at any time. It was recently found that the particle density $f(z)$ as a function of height (as measured from the bottom wall) is not constant in the suspension but a finite density gradient will appear [110, 158, 162].

3.2.3 Elongated Particles

To widen the discussion to elongated particles two questions remain to be answered: First, at what extend the spherical particle results are valid for the pair distribution of the elongated particles? Second, what can be said about the orientation distribution of the particles?

The visual examination of the cell experiments done by Herzhaft and Guazzelli [73] indicates that unlike spheres, rodlike particles have a tendency to form clusters. More quantitatively the same has been seen in the quasi-static simulations of Mackaplow, Shaqfeh and Butler [118, 27] where they used a modification of the slender body approximation to model the particles [93]. They saw that the particles tend to form a stream, or a single elongated cluster which was also manifested in the pair distribution function as a broad maximum around $r = 0$. At a certain finite particle density the width of the maximum was minimized.

Herzhaft and Guazzelli also found that the sedimenting rods preferred orientation with the axis of the rod parallel to gravity [73]. The shape of the orientational distribution and also the dynamics of an orientation of individual rods hinted that rods were under motion similar to the Jeffery orbitals [93]. On the other hand changing the particle aspect ratio did not change the orientational distribution suggesting the opposite. The results also suggested that the preference of parallel orientation increases with increasing Φ. The same was more clearly seen in the simulations of Butler and Shaqfeh [27].

3.3 Average Settling Velocity

Since the early experimental studies of sedimenting spherical particles a common observation has been that the average sedimentation velocity of the sedimenting spheres obeys the phenomenological *Richardson-Zaki law* (RZ law)

$$\langle v_{\parallel} \rangle = V_s(1-\Phi)^n, \tag{3.2}$$

where the exponent n is a function of the particle Reynolds number and is around 5.5 in low Re_p limit [152]. Qualitatively $\langle v_{\parallel} \rangle$ is a monotonically decreasing function of Φ and does not exceed the terminal velocity of a single particle, V_s, at any volume fraction. In dilute suspensions the measured average sedimentation velocities are slightly less than predicted by the RZ law and thus other semi-empirical relations have been constructed [8], which are, however, not widely used since they are much more complex and provide only relatively modest improvement to the RZ law. The RZ law can also describe the finite particle Reynolds number sedimentation with a different exponent n [152].

In the $\mathrm{Re}_p = 0$ limit the average sedimentation velocity can be calculated analytically with reasonable accuracy [10, 108, 70]. There is also a weak system size dependence in $\langle v_{\parallel} \rangle$ produced by the *intrinsic convection.* We will also consider the average sedimentation velocity of elongated particles where the RZ-law does not hold [152].

3.3.1 Quasi-Static Sedimentation

In the low Reynolds number limit the average sedimentation velocity can be calculated analytically. Here we will generalize the treatment of hydrodynamic interaction that was presented in the previous chapter. Now the state of the system is fully described if we know the $6N$ coordinates (spatial and angular) of N particles, combined here to one $6N$ dimensional vector $\mathbf{X}$. If we also know the external forces and torques acting to the particles, we can nominally write the equation for the particle velocities (translational and rotational) as

$$\mathbf{V} = \mathcal{M}(\mathbf{X})\mathbf{F}, \tag{3.3}$$

where the $6N$ dimensional vector $\mathbf{V}$ contains the spatial and rotational velocity components of all the particles and $\mathbf{F}$ contains the external forces and torques acting to them. The $6N \times 6N$ matrix $\mathcal{M}$ depends only on

$\mathbf{X}$ and is called *the mobility tensor,* and Eq. (3.3) *the mobility equation.* Correspondingly, if the velocities are known, the external forces and torques required to produce $\mathbf{V}$ can be obtained from the *resistance equation*

$$\mathbf{F} = \mathcal{R}(\mathbf{X})\mathbf{V}, \tag{3.4}$$

where $\mathcal{R} \equiv \mathcal{M}^{-1}$ is called the resistance tensor. It is important to note that Eqs. (3.3) and (3.4) are only valid if the ambient velocity of the fluid is zero, which can be assumed to be the case in sedimentation. It would be, however, straightforward to generalize these equations to the case of non-zero ambient flow [93].

If the probability density $P(\mathbf{X})$ that the distribution $\mathbf{X}$ occurs during steady state sedimentation is known we can express the steady state average sedimentation velocity of Eq. (3.3) as

$$\langle \mathbf{V} \rangle = \int \mathcal{M}(\mathbf{X})\mathbf{F}P(\mathbf{X})d\mathbf{X}. \tag{3.5}$$

A computationally effective way to construct the many-body mobility or resistance tensor is not, however, immediately clear. In the case of dilute suspension of spheres it is possible to construct $\mathcal{M}$ by adding pairwise the two-body mobility matrix $\mathcal{M}_{2B}$ formed by using the Rotne-Prager tensor, Eq. (2.17) and the Faxen law, Eq. (2.18), and taking into account all reflections with desired accuracy. This would lead to a mobility matrix $\mathcal{M}_{RP}$ that takes account correctly the full many-body far-field interaction of the particles but the short range lubrication forces would still be incorrect.

The other possibility is to first produce $\mathcal{R}$ by adding pairwise the two-body resistance matrixes $\mathcal{R}_{2B}$ given by Jeffry and Onishi [86] and then inverting the result. This approach leads to a mobility matrix $(\mathcal{R}_{pairwise})^{-1}$ that does take into account the two-body mobility correctly even at close distances but does not give the correct many-body far-field interaction.

To combine the benefits of the previous two approaches, Brady and Bossis [21] derived the resistance matrix as

$$\mathcal{R} = (\mathcal{M}_{RP})^{-1} + \mathcal{R}_{pairwise} - (\mathcal{M}_{2B}^{-1})_{pairwise}, \tag{3.6}$$

where $(\mathcal{M}_{2B}^{-1})_{pairwise}$ is constructed by inverting just the two particle mobility tensor for each pair of particles and then summing them over all the pairs.

The first analytic calculation of $\langle v_\parallel \rangle$ was done by Batchelor [10]. He used $\mathcal{M}$ constructed by using the Faxen law, Eq. (2.18) and the Rotne-Prager tensor, Eq. (2.17), as follows.

Considering only the translational velocity $\mathbf{v}_i$ of particle i and noting that the rotational motion of the particle is not coupled to the forces, Eq. (3.3) can be reduced to

$$\mathbf{v}^i = \sum_j \mathcal{M}^{ij}_{TT}(\mathbf{r}^{ij})\mathbf{F}^j, \tag{3.7}$$

where $\mathcal{M}^{ij}_{TT}(\mathbf{r}^{ij})$ is the part of the mobility tensor that couples the force $\mathbf{F}^j$ to the translational motion of particle i depending only on the relative position $\mathbf{r}^{ij}$, and has the form

$$\mathcal{M}^{ij}_{TT}(\mathbf{r}^{ij}) = \begin{cases} \mathbf{F}^j \cdot (1 - \frac{a^2}{6}\nabla^2)\mathcal{G}(\mathbf{r}^{ij}), & \text{for } i \neq j; \\ 6\pi\eta a \mathbf{1}, & \text{for } i = j, \end{cases} \tag{3.8}$$

where $\mathcal{G}^{\mathrm{RP}}(\mathbf{r}^{ij})$ is the Rotne-Prager tensor defined in Eq. (2.17) and $\mathbf{1}$ is the second rank unit tensor. The case with $i = j$ simply gives the terminal velocity obtained by the external force acting to the particle i itself.

Another assumption made here is that $P(\mathbf{X})$ can be approximated by the corresponding equilibrium distribution. Assuming that in the dilute limit we can reduce all distribution information to the pair distribution function $g_0(r)$ we get Eq. (3.3) to the form

$$\langle v_\parallel \rangle = V_S + n \int \mathbf{F}^j \cdot (1 - \frac{a^2}{6}\nabla^2)\mathcal{G}(\mathbf{r})(g(\mathbf{r}) - 1)d\mathbf{r}. \tag{3.9}$$

Here the integration is performed over all space and n denotes the particle number density. Subtracting 1 from g_0 is possible since the total volume flow in the suspension is zero, and it is needed to make the integral converging. After calculating the integral we get the result that $\langle v_\parallel \rangle = V_s(1 - 5\Phi)$. Here we have omitted the contribution from the image flow. In his original derivation Batchelor included also the contribution from the first images and obtained $\langle v_\parallel \rangle = V_s(1 - 6.55\Phi)$ [10].

Batchelor's result is only valid for dilute system since the pairwise constructed mobility tensor was used. Later similar calculations have been carried out by using Eq. (3.6) type of mobility tensor with two-body mobility tensor produced using the Rotne-Prager tensor (2.17) and the two-body resistance tensor with results obtained by Jeffrey and Onishi [86]. The

other modification is that the actual hard sphere equilibrium distribution $g_{\mathrm{eq}}(r)$ [135] has been used instead of $g_0(r)$. Such calculations has been provided by Beenakker and Mazur [12], Ladd [103] and by Hayakawa and Ichiki [70]. All these results are reasonably close to the experiments and simulations.

To close the discussion about the $\mathrm{Re}_p = 0$ results for $\langle v \rangle$ we want to return to Eq. (3.9) and consider the integral responsible for the deviation from V_s. The integrated function is essentially a product of the downward component of the velocity field generated by a particle with a relative position $\mathbf{r}$ and the difference between the average density and the pair distribution function.

3.3.2 The Effect of the Container Shape

In a finite container with solid walls the spatial symmetry is broken and the sedimentation velocity could vary. Beenakker and Mazur [13] produced a quasi-static limit calculation for $\langle v_{\|} \rangle$ in a spherical container and found that $\langle v_{\|} \rangle$ was a function of position [13]. Similarly, Geigenmüller and Mazur [58] (and later Bruneau *et al.* [24, 25]) studied the effect of the side walls on the sedimentation velocity. Assuming that particles do not overlap with walls, an *intrinsic convection* flow is formed in the vicinity of the walls due to the inhomogeneous particle density $f(x)$ near the wall. In particular, there is depletion of particles in a distance closer to the wall than the particle radius. In the special case where the suspension is confined between two infinite parallel vertical walls, this convection leads to an average settling velocity that is a function of the position relative to the walls. This phenomenon has been confirmed in the experiments of Peysson and Guazzelli [139].

3.3.3 Average Sedimentation Velocity for Elongated Particles

In striking contrast to the case of spheres, experiments with rod-like non-Brownian particles with $\mathrm{Re} \ll 1$ show that the mean settling velocity does not obey the RZ law even qualitatively. Kumar and Ramarao [98] studied the suspension of glass fibers (of length $\approx 250\mu$m and 50μm, and diameter $\approx 10\mu$m) and found that the fibers had a tendency to flocculate, which significantly slowed down the average velocity. Even when a dispersion agent

was added to the fluid to prevent cluster formation, $\langle v_\parallel \rangle$ decreased drastically when Φ increased beyond about 0.02. These results were corroborated by Turney *et al.* [165] who found by using magnetic resonance imaging that the functional form of $\langle v_\parallel \rangle$ in the suspension of rayon fibers ($320\mu\text{m} \times 20\mu\text{m}$) was significantly different from the RZ picture in the non-dilute limit. In particular, they found that $\langle v_\parallel \rangle$ decreased much more rapidly than the RZ law with $n = 4.5$, up to about $\Phi = 0.13$. The orientation of the fibers was however not measured in either of these experiments.

In the most recent set of experiments, Herzhaft *et al.* [72, 73] studied the suspension of more macroscopic glass rods of dimensions $(0.5 - 3)\text{mm} \times 100\mu\text{m}$. They tracked the motion of single marked rods and measured the rod orientation in addition to the settling velocity. They found that in larger volume fractions $\langle v_\parallel \rangle$ was indeed hindered more drastically than for spheres. However, perhaps the most interesting result was that for small volume fractions $\langle v_\parallel \rangle$ *exceeded* that of an isolated rod. This result indicates that $\langle v_\parallel \rangle$ for fiber-like particles has *non-monotonic* behavior for small Φ. They suggested that this phenomenon could be due to large inhomogeneities in the suspension, in the sense that there would be "fiber packets" which would settle faster than individual fibers [73]. They also observed that during sedimentation the majority of fibers were aligned parallel to gravity with no apparent dependence on either the fiber length or the volume fraction.

There exist some numerical simulations of sedimentation of many-particle fiber suspensions in the limit $\text{Re} = 0$. Mackaplow and Shaqfeh [118] studied particles with a large aspect ratio. They used the slender-body theory (see Ref. [9]) to calculate the average settling velocity for randomly formed static configurations of macroscopic elongated bodies with an aspect ratio of 100. In these studies, they found monotonic decrease of $\langle v_\parallel \rangle$ in the dilute regime. However, in their case the spatial distribution and alignment of the fibers was random and not induced by the true sedimentation dynamics. Ref. [118] and most recently Ref. [27] contain dynamical simulations for $\text{Re} = 0$ based on integrating the particle velocities obtained from the slender-body theory with some modifications. These approaches give a maximum for $\langle v_\parallel \rangle / V_s > 1$ in accordance with the experiments [73], and support the cluster formation mechanism and parallel alignment of fibers in enhancing settling.

3.4 Velocity Fluctuations and Diffusion

We will now proceed to the fluctating part of particle velocities. The size of the fluctuations is described by the second momentum of the velocity distribution. In the quasi-static limit, with no density gradient due to a bottom wall, the mean fluctuations scale with the system size. We will also discuss the higher moments of the velocity distribution and finally discuss the diffusive motion of the sedimenting particles.

3.4.1 Quasi-static Limit

During sedimentation each particle produces a velocity field around it which, in the creeping flow limit, decays as r^{-1} where r is the distance from the particle center. This velocity field influences the motion of the other particles [93]. With random fluctuations in the particle density this hydrodynamic interaction induces, even without Brownian motion, fluctuations around the average velocity $\langle v_{\|} \rangle$ for $\Phi > 0$, which leads to *diffusive* behavior of the particles. In the direction of gravity (negative z axis here), the size of the fluctuations is defined by

$$\sigma(v_z) = \sqrt{\langle v_z^2 \rangle - \langle v_z \rangle^2}, \tag{3.10}$$

where $\delta v_z = v_z + \langle v_z \rangle$ is the one-particle velocity fluctuation where the ballistic average motion has been removed from the velocity component parallel to gravity. The nature and origin of these velocity fluctuations have recently been under intense experimental and theoretical studies [148]. Of particular interest is the dependence of the velocity fluctuations $\sigma(v)$ on Φ and on the dimensions of the container. Early theoretical work concerning 3D systems by Caflisch and Luke [28] predicted that in the limit where inertial effects are negligible, the velocity fluctuations would diverge with the system size as $\sigma(v) \sim \Phi^{1/2}(L/a)^{1/2}$, where L is the linear size of the container. An intuitive way to obtain this result is to consider that a "blob" of N_{ex} excess particles in a volume of linear dimension ρ is sedimenting with relative velocity $V_s N_{\text{ex}} a/\rho$. If the particle distribution is uniformly random, it can be assumed that there exists a blob with $\rho \sim L$ and $N_{\text{ex}} \sim \sqrt{L^3\Phi}$ producing velocity fluctuations with the given scaling [157, 74].

Such divergence has been observed in numerical simulations of Ladd performed in periodic systems [107, 108]. However, in experiments it has been

observed that the velocity fluctuations saturate at a certain system size beyond which the container does not have any effect [130, 156]. In particular, Nicolai and Guazzelli used containers whose width varied from $51a$ to $203a$ and found no systematic increase in the velocity fluctuations [130]. Such results indicate that the size of the region where the particle motion is correlated is somehow reduced to a volume that is not proportional to the size of the container. This has also been observed directly by measuring the spatial velocity correlation length from the sedimenting suspension [156]. This has been recently shown to be the result of the horizontal walls of the container: there is a particle number density gradient which reduces the spatial size of the particle density fluctuations even if the spacing of the side wall diverges [117, 110, 162, 127]. The exact mechanism of the screening is, however, still an open issue [114, 38, 129].

Furthermore, Koch and Shaqfeh [95] have shown that if, instead of a uniformly random particle distribution, there is a sufficient average net depletion of other particles around each particle this also leads to saturating velocity fluctuations. Later Koch [96] showed that if $\mathrm{Re} \approx \mathcal{O}(1)$, the wake behind the particle will suffer such a depletion leading to $\sigma^2(v) \sim \mathcal{O}(\Phi V_s^2(\ln(1/\Phi) + const))$. In the regime $\mathrm{Re}_p < 1$ the expirement done by Cowan, Page and Weitz did not, however, reveal significant Re_p dependence in the velocity fluctuations [37].

An interesting special case is an unisotropic rectangular container. According to Brenner [23], if the walls exert no force on the fluid, it is the largest dimension which controls the behavior of ΔV. However, if no-slip boundary conditions are used, the smallest dimension restricts the growth of the fluctuations. Brenner studied a system that was confined between two vertical walls and noted that depending on Φ and the spacing of the walls L, the sedimenting particles could either be interacting strongly with the r^{-1} interaction or weakly, with an interaction decaying faster. This was based on the results of Liron and Mochon [115], who calculated that due to the particle-wall interaction, the velocity field around each particle decays as r^{-2} or faster whenever $r \gg x$, where x is the distance to the closest wall. If Φ and L are sufficiently small, the particles are typically closer to the walls than to each other and the system is said to be weakly interacting [23]. On the other hand, increasing Φ or L will eventually lead to a system where the particles are closer to each other than to the walls and the system is strongly interacting. Brenner also assumed that in a weakly interacting system, the particles are spaced uniformly but in a strongly interacting sys-

tem they are somewhat depleted from the center of the container since the particle diffusion is largest there due to the larger velocity fluctuations.

In simulations, periodic boundary conditions are often used. Even though no walls are present, additional force is exerted on the fluid by the periodic images. The contribution from the periodic images hinders the fluid velocity produced by the particle motion. Koch showed that in a geometry, where the height of the container is much larger than the other two equal dimensions, the velocity fluctuations are controlled by the smaller dimension [97]. Similar results were also obtained by Ladd using a lattice Boltzmann simulation technique [107].

3.4.2 The higher moments

While the behavior of $\langle v_z \rangle$ has been the subject of intense study [148], there is far fewer studies of the velocity distribution function itself. In the most simple-minded approximation, one would expect the particle velocities v_z to be uncorrelated leading to a Gaussian distribution for $P(v)$ as in the case of ordinary Brownian motion. Interestingly enough, this is not the case. Ichiki and Hayakawa [83] observed in their model simulations of a 2D fluidized bed that at $\Phi = 0.327$ $P(v_z)$ was asymmetric. Both of its branches could be fitted separately to a Gaussian distribution, but the upward branch was more extended.

In the subsequent experiments of Rouyer *et al.* [154] a suspension of spherical particles was studied experimentally by using a quasi-2D fluidized bed. They considered the case of high Péclet and low Reynolds numbers with $\Phi \in [0.08, 0.76]$ and confirmed that $P(v_z)$ was asymmetric. The downward branch was near Gaussian with

$$P(v_z/\sigma(v_z)) \propto \exp[-\beta(|v_z|/\sigma(v_z))^{\xi}], \tag{3.11}$$

where $\xi = 2$. The velocities have been normalized by the average fluctuation $\sigma(v_z)$ from the Gaussian part, and β is a constant. The upward branch was, however, a stretched exponential with the value of ξ decreasing from about 1.8 to 1 when the volume fraction increased from 0.12 to 0.70.

To explain their results, Rouyer *et al.* suggested that the particles can be considered to be "slow" or "fast": In the more dense areas the particles form kind of clusters, where the motion of single particles is Brownian-like.

The motion of the "fast particles" in the more dilute streams between the "clusters" is more correlated and they are typically moving fast upwards. They also studied $P(v_\perp)$ and found it to be non-Gaussian. They pointed out that the correlated feature of the motion of the fast particles should also stretch the tails of the horizontal velocity distribution.

Most recently, Miguel and Pastor-Satorras [126] performed computer simulations for a 2D system (with an additional velocity dependent friction term in order to mimic a quasi-2D experimental setup) using the Oseen tensor method. For $\Phi = 0.01$ they found again that $P(v_z)$ was asymmetric, but this time more stretched in the *downward* direction. They also adopted an argument based on fast and slow particles: The "fast particles" are those in downward streams and the "slow" ones are those caught into the swirls between the streams. Furthermore, they studied the autocorrelation function of the particle velocities and found that after an initial rapid decay region there was a region of slower decay. These two different decaying regions were connected to the two different type of particles.

3.4.3 Diffusion

If, in a long time limit, the average square displacement of a particle depends linearly on time the motion is diffusive [1]. For purely diffusive motion we can define the *tracer* diffusion coefficient D as

$$D = \lim_{t\to\infty} \frac{1}{2Ntd} \langle \sum_{i=1}^{N} (\mathbf{r}^i(t) - \mathbf{r}^i(0))^2 \rangle, \tag{3.12}$$

where $\mathbf{r}^i(t)$ is the position of particle i at time t and d is the number of dimensions. The motion of a sedimenting particle can be divided into ballistic and diffusive parts. The ballistic motion is a result from the action of gravity and is measured in the mean sedimentation velocity. The diffusive part results from the hydrodynamic interaction with other particles and it depends on the mean fluctuations and also how long a time a particle will keep its current direction. The latter is measured by the velocity fluctuation autocorrelation function (VACF)

$$C(t) \equiv \langle \delta v(t) \delta v(0) \rangle, \tag{3.13}$$

with $\delta v(t) \equiv v(t) - \langle v \rangle$. The tracer diffusion coefficient is related to VACF through a generalized Green-Kubo relation [63]

$$D = \frac{1}{d} \int_0^\infty C(t) dt. \tag{3.14}$$

It is clear that for diffusive motion $C(t)$ has to decay fast enough so that the integral in r.h.s. of Eq. (3.14) is be finite. Usually VACF for hydrodynamic system is assumed to decay exponentially, reflecting the lack of memory effects [19]. However, the results on the nontrivial intermediate time dependence of $C(t)$ indicate that this assumption does not hold in strongly interacting dissipative systems [99]. Thus there is no reason *a priori* why $C(t)$ should decay exponentially, either.

The behavior of $C(t)$ in sedimentation has been studied experimentally [131, 154, 14] and by numerical simulations [104]. It has been found that the decay of $C(t)$ is faster with larger Φ. Due to the anisotropy of directions $C_\parallel(t)$ calculated for the velocity component parallel to gravity behaves differently than $C_\perp(t)$ calculated for the perpendicular velocity component. Decaying of $C_\parallel(t)$ is slower than $C_\perp(t)$ in all volume fractions but the difference decreases with increasing Φ. Also the shape of the VACF is different. While $C_\parallel$ remains positive with all t the perpendiucular $C_\perp(t)$ has negative values with larger values of t.

Chapter 4

Numerical Methods

Since hydrodynamics plays an important role in a very large variety of different system with very different length and time scales, starting from organic processes and ending to the models of interstellar matter, also a huge number of different computational methods have been developed. We will here give a brief introduction to some of the methods that could be useful in studying the sedimentation process.

The nature of the sedimentation process sets several requirements for a numerical model. First of all it is necessary that the model can treat non-equilibrium processes. As a consequence of this it is extremely important that the local momentum conservation is fulfilled in the model. Another important requirement is that complicated boundary conditions can be treated effectively.

Here we have divided the possible methods into *mesoscopic fluid models* and *methods based on continuum description of the fluid.*. The latter category is further divided to *Stokesian dynamics* and *Navier-Stokes solvers*. The large amount of different techniques at use reflects two facts. First, the central parameters, *i.e.* Re and Pe, of the problem at hand restrict the use of some methods. Second, none of the methods is universal and can be applied to all cases. With mesoscopic models we refer to a number of techniques derived from the molecular nature of the fluid in small scales. The huge number of fluid particles requires some kind of coarse graining scheme.

By Stokesian dynamics we call here a family of techniques valid on the quasi-static regime. These methods are based to the fact that solving the

3D Stokes equation can be reduced to solving the 2D force density induced to the surface of the particles. The actual Stokesian dynamics [21] refers to a technique where the suspension problem is reduced even further to the point where velocities of the immersed bodies can be directly calculated using the mobility equation (3.3).

In the models based on the continuum description of the fluid, the Navier-Stokes equation (2.5) is solved directly by discretizing the velocity and pressure fields.

The classification is somewhat arbitrary, but suits for the brief description given here. We will next give a short review of the methods in different categories. Finally, we will give a more detailed explanation of the marker technique [76], which is the main technique used to obtain the results explained in this work.

Before discussing these methods in more detail we would like to note that the much used *Brownian Dynamics method* [3] is not considered here as a model for hydrodynamics since the method does not conserve the momentum locally. We have also restricted the review to the methods that provide access to the positions and velocities of individual embedded bodies. We have thus neglected those descriptions where also the particle phase has been coarse-grained, such as in phase-field methods [2], or in methods where both phases are described by continuum equations [85, 11].

4.1 Mesoscopic fluid models

Origin of the continuum fluid dynamics lies in the molecular structure of the fluid and in principle a huge molecular dynamical simulation would provide the same results as the continuum description of the fluid [149, 120]. Such a straight-forward approach would, however, lead to a very unefficient simulation technique since the inter-molecular collisions are much faster than the relevant time scales of the macroscopic bodies. Recently there has been rapid development of various computational methods that are based, at least conceptually, on the molecular structure of the fluid and where the problem of different time scales has been solved by performing a some kind of coarse-graining scheme [92]. Such methods can be called *mesoscopic* to emphasize that the description of the fluid is somewhere between molecular and continuum scales.

For mesoscopic methods it is characteristic that either the molecular degrees of freedom are decimated in the coarse-graining process or the dynamics of the molecules is simplified. Coarse-graining can either be started from actual molecular-level dynamics of a certain physical matter or it can be conceptual and the parameters of the mesoscopic model are adjusted to obtain certain macroscopic properties. Crucial point for all the methods is that the momentum and mass have to be conserved locally. Often this is also a sufficient requirement to obtain a model that would obey the NS equation (2.5) in large length scales.

Currently mesoscopic modeling is under rapid development and it is hard to give a comprehensive list all current variants. We give here just a few examples of different kind of mesoscopic pictures that either have been used to simulate sedimentation or have potential to be used in such processes. First *dissipative particle dynamics* is a molecular dynamic type of method where the particle-particle interaction contains also dissipative and random parts. Each particle is assumed to represent several fluid molecules. In *methods with simplified collisions* the dynamics of the fluid molecules is coarse-grained to suppress the details in the collisions between the fluid molecules. In the *lattice-Boltzmann method* the dynamics is based on the kinetic description of the fluid.

Common to all these methods is that the computational effort does not depend strongly on the number of embedded bodies but the amount of the particles that describe the fluid motion. Different boundary conditions of the simulation region are easy to implement. Usually the thermal Brownian motion is included in the methods in a natural way.

4.1.1 Dissipative Particle Dynamics

Originally the dissipative particle dynamics (DPD) method was described by Hoogerbrugge and Koelman [78]. The idea behind the method is that the fluid motion is modeled by quasi-particles with simplified interactions. The quasi-particles can be interpreted as a representation of a set of fluid molecules with velocity corresponding the collective motion of the molecules. The relative motion of individual fluid molecules is not tracked explicitely. Instead, they form a kind of a heat-bath inducing randomness and dissipation to the quasi-particle dynamics. The main benefit of this coarse-graining is that the interactions can be chosen to be smooth allowing a use of much

larger time step in the simulations [170]. To guarantee the conservation of momentum the force acting to each quasi-particle i is obtained in a pairwise manner [64]

$$\mathbf{F}_i = \sum_{j \neq i} (\mathbf{F}_{ij}^C + \mathbf{F}_{ij}^D + \mathbf{F}_{ij}^D), \tag{4.1}$$

where the force acting between quasi-particles i and j is divided to conservative ($\mathbf{F}_{ij}^C$), dissipative ($\mathbf{F}_{ij}^D$) and random parts ($\mathbf{F}_{ij}^R$). It is also required that $\mathbf{F}_{ij} = -\mathbf{F}_{ji}$. The conservative part of the force corresponds to the interaction due to a pair-potential in traditional molecular dynamics. In DPD the interaction is very soft having a form

$$\mathbf{F}_{ij}^C = a_{ij} w(|\mathbf{r}_{ij}|) \hat{\mathbf{r}}_{ij}, \tag{4.2}$$

where $\mathbf{r}_{ij}$ is the relative position of particles i and j, and $\hat{\mathbf{r}}_{ij}$ the corresponding unit vector. The coefficient a_{ij} defines the maximum interaction between particles i and j. There is some freedom to choose the weight function $w(r)$ but a convenient choice is

$$w(r) = \begin{cases} (1 - r/R_c), & \text{if} \quad r < R_c; \\ 0, & \text{if} \quad r > R_c, \end{cases} \tag{4.3}$$

where R_c defines the cutoff length of the particle-particle interaction. The random part of the interaction is given by

$$\mathbf{F}_{ij}^R = \sigma w(|\mathbf{r}_{ij}|) \zeta_{ij}(t) \hat{\mathbf{r}}_{ij}, \tag{4.4}$$

where the parameter σ defines the strength of the fluctuations and $\zeta_{ij}(t)$ is a Gaussian random variable with $\langle \zeta_{ij}(t) \rangle_{\text{eq}} = 0$ and $\langle \zeta_{ij}(t) \zeta_{kl}(t') \rangle_{\text{eq}} = (\delta_{ij}\delta_{kl} + \delta_{il}\delta_{jk})\delta(t - t')$. In a simulation with a discrete time step Δt this is replaced by $\zeta_{ij}\Delta t$. The weight function in Eq. (4.4) does not necessarily have to be the form given in Eq. (4.3) but it is a convenient choice. The dissipative part of the pair force is proportional to the relative velocity $\mathbf{v}_{ij}$ and has the form

$$\mathbf{F}_{ij}^D = -\gamma w^2(|\mathbf{r}_{ij}|)(\hat{\mathbf{r}_{ij}} \cdot \mathbf{v}_{ij}) \hat{\mathbf{r}}_{ij}, \tag{4.5}$$

where the friction parameter γ is fixed by the fluctuation-dissipation theorem to be equal to $\sigma^2/(2k_BT)$ and the weight function has to be the same as in Eq. (4.4). The interaction between the fluid and solid walls or immersed bodies can be implemented by constructing the solid objects from quasi-particles that are frozen to move like a single rigid body [18, 151]. Once the form of the inter-particle force is known, the system can be simulated

in the spirit of molecular dynamics [3]. It is, however, important to note that extra caution has to be taken in the integration of the particle motion due to the velocity dependent force [168].

Español showed that DPD indeed leads to the fullfilment of the NS equations (2.5) and the continuity equation (2.2), and he also derived the expression for the macroscopic viscosity [44]. Respectively, Flekkøy *et al.* have derived DPD starting from molecular dynamics [52]. In the traditional DPD described here, the energy is not conserved. There are, however, variants that do conserve it [5, 45] making them usable also for cases where heat transfer or thermal convection plays a role. Some other variants of DPD are the *smoothed dissipative particle dynamics*, which provides more leeway to match the dynamics to a certain equation of state [46] and the *Lowe-Andersen thermostat*, where the dissipation is taken into account by changing randomly the velocities of each close pair of particles [116]. The primary gain here is to get rid of the velocity dependence of the dissipative force.

With its variants the DPD method is mostly used to model equilibrium hydrodynamics and it introduces the thermal fluctuations in very satisfactory way. Even though the method can be used in non-equilibrium processes, too [160], we are not familiar with any work where DPD would have been used to model sedimentation. However, DPD could be a useful method to study very low Pe sedimentation.

4.1.2 Methods with Simplified Collisions

Another mesoscopic approach to model the fluid is to simplify the dynamics of the microscopic degrees of freedom, rather than reducing them. In particular, the inter-molecular collision processes can be coarse-grained so that the dynamics of the molecules can be divided to two phases: during the free-streaming the fluid particles are moving along a straight path described by the velocity and in the collision phase the velocities are instantaneously changed according to some rules. An early example of this kind of method is the *direct simulation Monte Carlo* method described by Bird [16].

Recently, Malevanets and Kapral [119] introduced the *stochastic rotation dynamics* method that was based on similar idea. There the whole simulation volume is divided into cells and the collision phase is carried out

separately at each cell by rotating the velocity $\mathbf{v}_i$ of each fluid particle i as

$$\mathbf{v}_i(t + \Delta t) = \bar{\mathbf{v}}_\xi(t) + \hat{\omega}_\xi(\mathbf{v}_i(t) - \bar{\mathbf{v}}_\xi(t)). \tag{4.6}$$

Here $\bar{\mathbf{v}}_\xi(t)$ is the average velocity of particles located in cell ξ after the streaming phase. Each cell is assigned an individual rotation operator $\hat{\omega}_\xi$ that is taken randomly from a certain set Ω of rotation operators. Inside each cell the momentum and energy are conserved during the collision phase. The macroscopic properties of the fluid are set by the choice of Ω. Interaction between the fluid particles and immersed larger bodies can be taken into account also during the collision phase or by a traditional two-body potential.

In the *lattice-gas method* the fluid particle motion is restricted to a lattice [56]. There is also only a discrete set of possible velocities $\{\mathbf{c}_k\}$ which have been chosen so that during the chosen time step Δt particles will travel from the initial lattice point to another one. For a 3D simulation, the most used set of velocities contains 19 possible velocities, with one describing those particles that will occupy the same lattice site during the next time step, six corresponding to the motion to the nearest-neighbor lattice sites, and twelve to the next-nearest-neighbor sites. Thus, nearest-neighbor and next-nearest neighbor sites are said to be linked to describe that the particle distribution can flow between these sites during one time step.

The number of particles at lattice site $\mathbf{x}$ with velocity $\mathbf{c}_k$ in a certain time instant t is given $n_k(\mathbf{x}, t)$, which can only have values 0 or 1. At each time step, before the particles are moved to the new lattice sites, they collide with other particles occupying the same lattice site. The collision is done by randomly changing values of $n_k(\mathbf{x}, t)$ so that $\sum_k n_k(\mathbf{x}, t)$ and $\sum_k n_k(\mathbf{x}, t)\mathbf{c_k}$ does not change, *i.e.* the mass and momentum are conserved. The streaming phase and the collision phase can be combined to give the evolution of the particles as

$$n_k(\mathbf{x} + \mathbf{c_k}\Delta t, t + \Delta t) = n_k(\mathbf{x}, t) + \Omega_k(\{n_k(\mathbf{x}, t)\}), \tag{4.7}$$

where Ω_k is the random collision operator. The lattice-gas method is easy to implement and the computational cost of single lattice point is very low. However, it has been shown that even though true hydrodynamics is obtained by the method, the needed amount of lattice sites could be quite high [144].

4.1.3 Lattice-Boltzmann method

Even though the basis of the Lattice-Boltzmann method (LBM) can be derived from the continuum Boltzmann equation [71] we will describe it here as a generalization of the lattice gas method [56]. We will here briefly describe the basic elements of LBM. A more complete representation can be found in the reviews of Chen and Doolen [31], or Ladd and Verberg [109].

In LBM the idea of the lattice-gas simulation is advanced to a more mesoscopic description of the fluid. The boolean variable n_k is replaced by a real valued one describing the local velocity distribution of the particles occupying the given lattice site. The density of the fluid is defined as $\rho_l(\mathbf{x},t) = \sum_k n_k(\mathbf{x},t)$. Note that ρ_l is now a function of time and position since we do not require strict non-compressibility.

The collision phase is also altered and the collisions are not stochastic incidents anymore but coarse-grained processes of larger set of particles with deterministic outcome. Instead of making a random change the collision operator is now changing $n_k(\mathbf{x},t)$ closer to the local equilibrium distribution n_k^{eq} with the same density and momentum density, *i.e.* n_k^{eq} obeys $\sum_k n_k^{\mathrm{eq}} = \sum_k n_k(\mathbf{x},t)$ and $\sum_k n_k^{\mathrm{eq}}\mathbf{c}_k = \sum_k n_k(\mathbf{x},t)\mathbf{c}_k$. By assuming that the initial distribution is not far away from the equilibrium distribution one can linearize the collision operator and Eq. (4.7) can be written in form

$$n_k(\mathbf{x}+\mathbf{c_k}\Delta t, t+\Delta t) = n_k(\mathbf{x},t) + \sum_{k'} M_{kk'}(n'_k(\mathbf{x},t) - n_{k'}^{\mathrm{eq}}), \tag{4.8}$$

where the collisions are handled by a matrix $M_{kk'}$ obeying the relations $\sum_i M_{kk'} = 0$ and $\sum_k \mathbf{c}_k M_{kk'} = 0$. The most simple choice of $M_{kk'}$ is

$$M_{kk'} = -\frac{1}{\tau}\delta_{kk'}, \tag{4.9}$$

where parameter τ describes how fast the local equilibrium is reached and defines the viscosity as $\eta = \rho(2\tau-1)/6$ [30]. To obtain better accuracy in fluid boundaries Ladd has introduced a more general form of M_{ij} [106]. Equation (4.8) can be completed by a term corresponding to the interaction of an external force.

A simple way to satisfy a static boundary condition is to use a bounce-back rule to those particle distributions that would otherwise move outside the fluid region. This means that if the boundary node $\mathbf{x}'$ has a distribution

$n_k(\mathbf{x}', t)$ with such a $\mathbf{c}_k$ that $\mathbf{x}' + \mathbf{c}_k \Delta t$ lies outside the fluid domain, it is replaced in next time step with the distribution $n_{\hat{k}}(\mathbf{x}', t)$, where $\mathbf{c}_{\hat{k}} = -\mathbf{c}_k$. The bounce-back rule was generalized by Ladd to take into account also the momentum exchange between the fluid and moving boundaries [106]: For an immersed moving body it is required to apply the bounce-back rule separately to both the interior and the exterior of the moving body for each link intersected by the boundary. Considering a pair of lattice sites $\mathbf{x}$ and $\mathbf{x}' = \mathbf{x} + \mathbf{c}_k \Delta t$ connected by a link that is cut by a particle surface, the bounce-back rule comes to form

$$\begin{aligned} n_{\hat{k}}(\mathbf{x}, t + \Delta t) &= n_k(\mathbf{x}, t) + B(\mathbf{c}_k \cdot \mathbf{v}_b); \\ n_k(\mathbf{x}', t + \Delta t) &= n_{\hat{k}}(\mathbf{x}', t) + B(\mathbf{c}_{\hat{k}} \cdot \mathbf{v}_b), \end{aligned} \tag{4.10}$$

where $\mathbf{v}_b$ is the velocity of the boundary at the location of the intersection and B is a coefficient depending on the density of the body and the detailed lattice structure. The interaction of two immersed bodies has to be completed by adding a short term lubrication interaction to take into account directly the hydrodynamic interaction of bodies with a distance (from surface to surface) less than the lattice constant.

While thermal fluctuations were fundamentally present in the lattice-gas model, they have been averaged out in the standard LBM. It is, however, possible to add a random part to the collision operator to obtain fluctuations to the flow field corresponding to the required temperature [105]. It is also possible to add a term to the r.h.s. of Eq. (4.8) to produce the action of an external force to the fluid.

The lattice-Boltzmann method is valid for a large range of Re_p and Pe although the thermal fluctuations do not appear naturally. The method scales linearly with the number of lattice sites and is relatively easy to implement. The method has been one of the most successful to simulate the particle flow or sedimentation especially in the finite Re regime. The method has been used to study the sedimentation of a few bodies by Qi [145] and by Feng and Michaelides [50]. Xu and Michaelides have studied the sedimentation of several bodies in a 2D channel using Re_p up to 10 [171]. Ladd and his co-workers have applied LBM to various problems related to the sedimentation of spheres with using up to 32000 particles [108, 109]. Qi has used LBM to simulate fluidization of several tens of rectangular bodies in 2D [146] and 3D [147].

4.2 Stokesian dynamics

As described in Chapter 2 the quasi-static Stokes equation (2.8) can be solved analytically and it is thus possible to obtain the hydrodynamic interaction between suspended bodies directly without explicitely solving the motion of the surrounding fluid. In the general case the problem reduces to solving the force density induced to the surface of the particles from the 2D integral equation (2.16) [93]. Some recent numerical methods to study a suspension of arbitrary shaped particles have been developed by Fan *et al.* [47] using the boundary-element method and by Pozrikidis [143] using the spectral-element collocation point method [91].

If the immersed bodies have a high degree of symmetry the numerical methods to obtain the hydrodynamic interaction can be further simplified by using the multipole expansion. The problem is reduced to constructing the many-body $\mathcal{M}$ or $\mathcal{R}$. One of the best-known implementation of such a technique is *the Stokesian dynamics* method developed by Brady and Bossis [21]. The method is based to the resistance tensor created as described in Eq. (3.6) using the Rotne-Prager tensor (2.17) to describe the two-body mobility, and the results of Jeffery and Onishi [86] for the two-body resistance tensor.

The dynamical simulation of sedimentation can be performed by first solving the hydrodynamic forces and torques acting on the bodies based on the current positions and velocities of the bodies. The dynamics of N solid bodies are now given by

$$\mathbf{m} \cdot \frac{d}{dt}\mathbf{V} = \mathbf{F}^{\mathrm{h}} + \mathbf{F}^{\mathrm{ext}}, \tag{4.11}$$

where $\mathbf{m}$ is a $6N \times 6N$ diagonal matrix containing the masses and moments of inertia of the N particles. The $6N$ dimensional hydrodynamic force vector $\mathbf{F}^{\mathrm{h}}$ is given by Eq. (3.4) and $\mathbf{F}^{\mathrm{ext}}$ contains all the external forces and torques acting to the particles. The time evolution of the immersed bodies can be calculated by numerically integrating Eq. (4.11). This approach has a certain analogy to the standard Molecular Dynamics method [3] except that here the interaction between the macroscopic suspended particles is more complicated. Another possibility is to consider the system as a mobility problem and solve the particle velocities directly based on the external forces acting to the particles. By assuming that the inertia of the bodies does not

play any role, the system can also be considered as a mobility problem and the particle velocities are directly given by Eq. (3.3).

In order to take into account thermal fluctuations it is also possible to add a stochastic part to the motion of the bodies. During a small time step Δt the general change to particle coordinates is given by

$$\Delta \mathbf{X} = \mathcal{M} \cdot \mathbf{F}^{\text{ext}} + k_b T \nabla \cdot \mathcal{M} \Delta t + \xi(\Delta t), \tag{4.12}$$

where $k_b T$ is the temperature and the stochastic function $\xi(\Delta t)$ has the following properties

$$\langle \xi(\Delta t) \rangle = 0, \quad \langle \xi(\Delta t) \xi(\Delta t) \rangle = 2 k_b T \mathcal{M} \Delta t, \tag{4.13}$$

which can be derived by assuming that the fluctuation-dissipation theorem is satisfied.

Stokesian dynamics (as well as the other boundary integral methods) has a number of desirable properties. It is numerically less time consuming than solving the full Navier-Stokes equation (2.5) and the computational costs depend only on the number and complexity of the immersed bodies. Stokesian dynamics can thus be used to study the behavior of immersed bodies in an unbounded fluid (periodicity or container walls will provide additional complications). Due to the matrix inversions and calculation of $\xi(\Delta t)$ the standard Stokesian dynamics method scales as $\mathcal{O}(N^3)$. There are, however, novel techniques to reduce the scaling to $\mathcal{O}(N \log N)$ (non-Brownian case) or $\mathcal{O}(N^{1.25} \log N)$ (Brownian case) [159] but they also increase the complexity of the method. The method is also strictly limited to the case $\mathrm{Re} = 0$.

Ladd has carried out sedimentation simulations [108] using a somewhat older version of the method [122] for up to 256 particles. Similarly, Miguel and Pastor-Satorras used a two-dimensional modification of the method to study sedimentation in a thin slab [126]. Koch has produced static simulations with similar ideas by generating random particle configurations and calculating the particle velocities by constructing the mobility tensor using the periodic version of the Oseen tensor [69] and used up to 200 particles [97]. Brenner produced dynamical simulations with walls in one direction by using a slightly modified Oseen tensor for point-like particles (to get rid of the singularity) and summation described by Liron and Mochon [115] to take account the no-slip boundary conditions. Finally, Mucha *et. al* [127]

simulated the sedimentation of over 4 million point-like particles using a method scaling as $\mathcal{O}(N \log N)$.

To study the suspension of elongated bodies Claeys and Brady used a method similar to Stokesian dynamics. The bodies were prolate spheroids and the mobility tensor was created using the multipole expansion for a spheroid [32, 33, 34]. Fan *et al.* simulated fiber suspension by using the slender body approximation [9] to model the far-field interaction and a lubrication theory to the near-field. Similar method was used by Mackaplow, Shaqfeh and Butler to simulate sedimentation of fibers [118, 27]. Finally, Yamamoto and Matsuoka simulated elastic fiber suspension by connecting spherical particles together with springs [173, 174].

4.3 Navier-Stokes solvers

The most straight-forward approach to solve a problem that can be described by the continuum fluid dynamics is to find out the numerical solution to the Navier-Stokes equation (2.5) and the equation of continuity (2.2) itself with the given boundary conditions. Due to the importance of the fluid dynamics in engineering sciences there has been a long period of intense studies to develop such methods as documented extensively in the literature [51, 177].

To all the techniques in this category it is common that the field variables (here the fluid velocity $\mathbf{u}$ and the pressure p) have to be discretized. This means that each field is defined by giving its value in a discrete and finite set of lattice sites. If the values of the fields are needed in off-lattice positions they can be obtained by interpolating from the near-by lattice points. The lattice could be either regular or irregular. Regular lattices have repeated patterns and can be described by a set of lattice constants *e.g.* the 3D regular cartesian lattice points can be described as $\mathbf{x}_{n_1,n_2,n_3} = \Delta x(n_1\hat{\mathbf{e}}_1 + n_2\hat{\mathbf{e}}_2 + n_3\hat{\mathbf{e}}_3)$.

The next step is to replace the partial differential equations (2.5) and (2.2) by a finite set of algebraic equations related to the discretized fields. From all the variants to do this we want to mention the *finite difference method* (FDM), the *finite volume method* (FVM) and the *finite element method* (FEM). In FDM the spatial derivatives are replaced by their discrete counterparts. There are many possibilities to do this but a simple and intuitive

possibility for a cartesian regular lattice is to make the replacements

$$\begin{aligned} \frac{\partial \Psi(\mathbf{x}_0)}{\partial x_\alpha} &\rightarrow \frac{\Psi(\mathbf{x}_0 + \Delta x \hat{\mathbf{e}}_\alpha) - \Psi(\mathbf{x}_0 - \Delta x \hat{\mathbf{e}}_\alpha)}{2\Delta x}; \\ \frac{\partial^2 \Psi(\mathbf{x}_0)}{\partial x_\alpha^2} &\rightarrow \frac{\Psi(\mathbf{x}_0 + \Delta x \hat{\mathbf{e}}_\alpha) - 2\Psi(\mathbf{x}_0) + \Psi(\mathbf{x}_0 - \Delta x \hat{\mathbf{e}}_\alpha)}{(\Delta x)^2}, \end{aligned} \tag{4.14}$$

where Ψ is an arbitrary discretized field. Once all the spatial derivatives in Eqs. (2.5) and (2.2) have been replaced by their differential counterparts, we are left with a set of ordinary differential equations with one equation for each lattice site.

In FVM the simulation volume is divided into small polyhedra so that each encloses one lattice site, locating at its center. Now, instead of dealing with the original partial differential equations, we consider their integral representations. For Navier-Stokes equation (2.5) this is given by

$$\frac{\partial}{\partial t} \int_\Omega \mathbf{u} d\Omega + \int_S \mathbf{u}\mathbf{u} \cdot \hat{\mathbf{n}} dS = \rho_l^{-1} \int_S \sigma \cdot \hat{\mathbf{n}} dS + \int_\Omega \mathbf{f} d\Omega, \tag{4.15}$$

where $d\Omega$ is a differential volume element, dS a differential surface element, and $\hat{\mathbf{n}}$ is a unit vector pointing outward from the surface. Equation (4.15) is written separately to each volume element and the surface integrals are divided as separate integrals for each face. As an example of a simple approximation of the integrals one can assume that the volume integral $\int_\Omega \Psi d\Omega$ is replaced by $\Delta\Omega\Psi(\mathbf{x}^c)$ where $\Delta\Omega$ is the total volume of the volume element and $\Psi(\mathbf{x}^c)$ is the value of the field Ψ at the center of the volume element *i.e.* at one of the lattice sites. Similarly, the surface integral $\int_{S_k} \Psi dS$ can be replaced by $\Delta S_k \Psi(\mathbf{x}_k^c)$ where ΔS_k is the area of the face k of the polyhedral volume element. Now $\mathbf{x}_k^c$, the center of face k, is not a lattice point and $\Psi(\mathbf{x}_k^c)$ is obtained by interpolating the valuea from the nearby lattice points. Finally, the surface integrals between two neighboring volume elements have to be matched since the outflow from one volume element is an inflow to the neighboring elements. We want to emphasize that the discretizations presented here are just examples of the simplest, first order approximations. There are numerous possibilities to obtain better approximations leading to smaller discretization errors [51]. Finally, the FEM method can be considered to have a similar idea to the FVM. The integral calculation is improved by computing a weight function for each finite element. The important advantage of FEM is that it can deal with arbitrary geometries.

In order to study time dependent flow, the time derivative has to be discretized too. As a first-order approximation $\partial\Psi(t)/\partial t$ can be replaced by $(\Psi(t+\Delta t)-\Psi(t))/\Delta t$. There are again large variety of methods to do the time-discretization accurately [51].

To produce a method suitable to study dynamics of the suspension one needs three main ingredients. The first one is a method to solve the fluid dynamics which we already discussed. The other is to track the rigid body motion of the immersed bodies. The third one is a scheme to couple these two phases, which in the continuum description means taking into account the no-slip boundary condition between the fluid and the rigid bodies. We will next discuss two main methods to do this. One is using explicit boundary conditions and the other is to obtain the no-slip boundary condition by inducing a suitable force density field to the fluid.

In all the discretization methods described here the traditional way to obtain the boundary conditions is to match the fluid discretization to the geometry of the boundaries. In most cases, and especially in sedimentation, this requires the use of an irregular lattice. Typical flow simulation contains thus two steps: the lattice creation and the solving of the partial differential equations. In the simulation of sedimentation (or any setup with time-dependent boundary conditions) the lattice creation has to be performed at each time step. The dynamics of the immersed solid bodies can be solved with techniques that are familiar from traditional molecular dynamics, but once the bodies have moved, the lattice has to be updated to correspond to the new boundary conditions. Hu *et al.* have developed a code for 2D particle flow [80] which has been used to study the mutual motion of a few settling particles [49] and sedimentation of up to 400 particles [81]. By using fast automatized mesh creation and update methods [88, 87] Johnson and Tezduyar have produced 3D simulations using up to 1000 particles [89, 90]. This simulation required, however, a very large computational capacity. The use of adjusted mesh makes it possible to use a finer mesh in the places where additional computational accuracy is needed, like in between close pairs. Solving the Navier-Stokes equation in an irregular lattice is, however, much more time-consuming than in a regular one.

To reduce the computational cost, several methods have been developed where the boundary condition between the fluid and the immersed bodies are not taken explicitely account and the fluid flow can thus be solved in a regular mesh. In one family of such methods the motion of the fluid phase solved in the whole simulation volume by the lattice based method is

assumed to produce an ambient background flow. The immersed bodies are coupled to the fluid phase by using the multipole expansion for the force (2.19) and torque (2.20) or the Faxen law (2.18) derived in the Re_p=0 limit. Schwarzer implemented such a method by using Eq. (2.19) for the coupling and dividing the corresponding force acting to the fluid only by the lattice points nearest to the particle center [155]. Maxey *et al.* used the same kind of approach with more realistic coupling between the solid bodies and the fluid phase [121, 36]. The weakness of these methods are that the validity of Eq. (2.19) has to be taken as granted. It can only be implemented for bodies of high symmetry.

A more sophisticated approach is the immersed boundary method suggested by Fogelson and Peskin [53] where the fluid is assumed to fill the whole simulation volume but inside the solid bodies the motion of the fluid is forced to coincide with the rigid body motion. In the Fictitious Domain method developed by Glowinski *et al.* [60, 61] the fluid treated by FEM is forced to obtain the motion of the immersed bodies by Lagrange multipliers. The method has been used to study sedimentation of 6400 spherical particles [61, 133]. The method has also been used to simulate the motion of an ellipsoid [132], and there are also some other variants of the method [41].

The method developed by Höfler and Schwarzer [76] is based on similar ideas. In this method the fluid dynamics is solved using FDM and the rigid body motion is obtained by tracking the motion of certain points related to the rigid body motion and by introducing a penalty force if the rigid body motion is violated. This is the method used in most of the work presented here so it is explained in more detail in the following section. The same method has also been used by Fonseca and Herrmann to study the sedimentation of oblate spheroids with non-periodic boundaries [54, 55]. Our implementation of the method performs quite well compared to the other codes capable for similar simulations. As an example let's consider a system with size about 15600 times the volume of single particle containing 2325 particles with particle Reynolds number 0.5. Using 2.2 GHz Optiron processor it would take about 7 CPU minutes to simulate the system one Stokes time (the time it takes from single particle to sedimentate amount of its radius).

There are also some other implementation of similar ideas [161, 128]. Common to all these methods is that they could in principle be used to simulate the suspension of arbitrarily shaped particles. The only complication rising from irregular immersed bodies is that a short-range particle-particle inter-

action has to be introduced to prevent the particles from overlapping. All the methods scale essentially as $\mathcal{O}(N)$. Most naturally they are formulated in the $\mathrm{Pe} = \infty$ limit, but finite thermal fluctuations can be added to the fluid-particle coupling if necessary.

4.4 The marker technique

We will now describe in detail the marker technique developed by Höfler and Schwarzer [76]. This is the method that we have used to obtain most of the result of this thesis. It is based on the continuum description of the fluid and treats the boundary conditions by inducing an additional force distribution to the fluid.

The fluid dynamics is solved using FDM. We discretize Eq. (2.5) on a regular, staggered marker and cell (MAC) mesh to second order precision in space (*cf.*, *e.g.* [138]). The discretized counterpart of ∇ is denoted by $\tilde{\nabla}$. For the time step we use a first order approximation $(\partial/\partial t)\mathbf{u}(t) \to (\mathbf{u}^{n+1}-\mathbf{u}^n)/\Delta t$, where we have adopted a short hand notation $\mathbf{u}^n = \mathbf{u}(n\Delta t)$. Next we perform a splitting by adding and subtracting a term $\mathbf{u}^*$ on the left hand side of the discretized Eq. (2.5). The term $\mathbf{u}^*$ has been chosen so that Eq. (2.5) can be splitted into a system of two equations for the discretized variables $\mathbf{u}^n$, p^n and $\mathbf{f}^n$,

$$\frac{\mathbf{u}^* - \mathbf{u}^n}{\Delta t} = -(\mathbf{u}^n \cdot \tilde{\nabla})\mathbf{u}^n + \frac{\eta}{\rho_l}\tilde{\nabla}^2\mathbf{u}^n + \rho_l^{-1}\mathbf{f}^n, \tag{4.16}$$

$$\frac{\mathbf{u}^{n+1} - \mathbf{u}^*}{\Delta t} = -\tilde{\nabla}p^{n+1}. \tag{4.17}$$

From the first equation, we determine $\mathbf{u}^*$, subject to the required boundary conditions. Forming the divergence of the second equation and using the incompressibility condition $\nabla \cdot \mathbf{u}^{n+1} = 0$, we find a Poisson equation for the pressure

$$\tilde{\nabla}^2 p^{n+1} = \frac{\tilde{\nabla} \cdot \mathbf{u}^*}{\Delta t}. \tag{4.18}$$

Solving the Poisson equation is numerically the most demanding task but there exist efficient methods to solve it in a regular mesh. We used a multigrid method that ensures that the computational effort is proportional to the number of grid points when the system size is increased keeping the grid spacing constant [65]. We note that p^n in the numerical formulation

presented above has some properties which are not shared with the physical pressure. For example, in the presence of a rigid boundary the numerical solution of the system of Eqs. (4.16) and (4.17) does not depend on the value of $\mathbf{u}^*$ on the boundary and we can thus choose any convenient value for the normal pressure derivative, typically zero (*cf.* Ref. [138]). This freedom does not exist for periodic systems. In any case it is convenient to subtract the hydrostatic part of the pressure field away. This is obtained naturally by reducing the gravity away from the force density $\mathbf{f}$. Furthermore, p is not evaluated at the same "time" as the diffusive and convective terms and thus it does not strictly correspond to the physical pressure field [142]. Once p is found we employ Eq. (4.17) to find the updated velocity field $\mathbf{u}^{n+1}$.

The stability criterions of the method requires that the time step has to be chosen such that

$$\Delta t < \frac{1}{2d}\frac{\rho_l(\Delta x)^2}{\eta}, \tag{4.19}$$

where Δx is the lattice constant and d is the dimensionality of the system. The criterion shows that the time step has to be reduced linearly with decreasing Re_p.

There are two main features to take into account in the coupling scheme between the fluid phase and the embedded rigid bodies. First, the no-slip boundary condition on the particle surface has to be satisfied without compromising the efficiency of the fluid solver. Second, the forces $\mathbf{F}_i^{\mathrm{h}}$ and torques τ_i^{h} exerted by the fluid on particle i have to be calculated. Ideally, smooth bodies should never touch due to the divergent lubrication forces on close approach. However, on a finite grid, we cannot resolve this divergence and we must introduce additional forces $\mathbf{F}_i^p$ and torques τ_i^p to model the close contact of particles, as will be described in detail later.

Newton's equation of motion for the center of mass of body i reads

$$m_i\dot{\mathbf{v}}_i = \mathbf{F}_i^{\mathrm{h}} + \mathbf{F}_i^p - \frac{\Delta\rho g m_i}{\rho_p}\hat{\mathbf{e}}_z, \tag{4.20}$$

where $\mathbf{v}_i$ is the velocity of the center of mass and m_i is the mass of particle i. Since we have removed hydrostatic pressure from the fluid equations, we need to introduce a buoyancy term into the particle equations. Together with the weight of the bodies, it forms the third term on the right hand side of Eq. (4.20).

For the angular velocity ω_i of the rigid bodies, we obtain

$$\mathbf{I}_i\dot{\omega}_i = \tau_i^{\mathrm{h}} + \tau_i^p, \tag{4.21}$$

where the torques and angular velocity are computed with respect to the center of mass, and $\mathbf{I}_i$ is the inertial tensor of the body i.

The general idea behind the marker technique is to represent the rigid bodies via a manipulation of the body force term $\mathbf{f}$ in Eq. (2.5). To this end, we consider $\mathbf{f}$ to be a spatially distributed (fictitious) constraint volume force which causes the fluid to move as a rigid body "inside" the particles. Observed from the outside, the rigid body region imposes the same constraints as a true rigid particle at the same location, thus giving rise to the same stresses at the "interface." The no-slip condition is satisfied to the same degree as the equation of motion for the fluid and its discretization guarantee continuity. The forces and torques on the particles are equal to specific moments of the constraint force distribution, so that we can avoid the explicit integration of the stress over the particle surface which is otherwise necessary in order to compute F_i^{h} and τ_i^{h}.

In order to determine the fictitious body force numerically, we use an explicit penalization technique which integrates seamlessly with the fluid solver.

First, we introduce a rigid particle *template* T_i as the set of all spatial points inside the volume occupied by the body i. Now T_i has, at all times, the same shape as the corresponding physical body and its position and orientation changes with time as the body moves. We identify the position and orientation of the T_i by its center of mass $\mathbf{x}_i(t)$ and by rotation matrix $\mathbf{O}_i(t)$.

We will next define another region Ω_i as the set of all fluid elements corresponding the region initially defined by the volume of the body *i.e.* at $t = 0$ we have $\Omega_i = T_i$. Later on, the time evolution of Ω_i does not follow directly T_i, but instead at a later time instant Ω_i corresponds to the same fluid elements that have been moved according to Eq. (2.5). To express the difference between the time evolution of T_i and Ω_i we define a time dependent displacement field as

$$\boldsymbol{\epsilon}_i(\tilde{\mathbf{x}}) = \mathbf{x}_i(t) + \mathbf{O}_i(t) \cdot \tilde{\mathbf{x}} - \mathbf{X}(t), \tag{4.22}$$

for all $\tilde{\mathbf{x}} \in T_i$. Here the notation $\tilde{}$ means that we refer to the coordinates measured in axes that are fixed to the template. With $\mathbf{X}(t)$ we refer to the coordinates of the fluid element identified by $\mathbf{X}(0) = \mathbf{x}_i(0) + \mathbf{O}_i(0) \cdot \tilde{\mathbf{x}}$. The evolution of the template and the fluid regime is now coupled by inducing a coupling force field

$$\mathbf{f}_i^c(\mathbf{x} + \boldsymbol{\epsilon}_i(\mathbf{O}_i^{-1}(t) \cdot [\mathbf{x} - \mathbf{x}_i])) = -k\boldsymbol{\epsilon}_i(\mathbf{O}_i^{-1}(t) \cdot [\mathbf{x} - \mathbf{x}_i]), \tag{4.23}$$

to Eq. (4.16). Note that $\mathbf{f}_i^c$ is zero for all $\mathbf{x} \notin T_i$. The coefficient k defines the stiffness of the coupling.

To implement the coupling force numerically we represent T_i as a discrete set of marker points with coordinates $\{\tilde{\boldsymbol{\xi}}_{il}\}$ with $l = 1, \ldots, n_i$. Correspondingly we have n_i fluid markers with coordinates $\{\boldsymbol{\xi}'_{il}(t)\}$, whose time evolution is determined by $\mathbf{u}(\boldsymbol{\xi}'_{il}(t))$. For each i and l we now get a point force

$$\mathbf{f}_{il}^c = -k'[(\mathbf{x}_i(t) + \mathbf{O}_i(t) \cdot \tilde{\xi}_{il}) - \boldsymbol{\xi}'_{il}], \tag{4.24}$$

acting to the point $\boldsymbol{\xi}'_{il}$. This can be interpreted as a spring connecting the template marker and the fluid marker with a spring constant k'. We impose each point force $\mathbf{f}_{il}^c$ onto the fluid by dividing it between the six nearest grid points. Its sign ensures that the effect on the fluid will tend to be a reduction of the modulus of ϵ_i. If the external stresses are bounded, then ϵ_i remains bounded and approaches zero as the spring constant k' increases. If k' is sufficiently large then the internal time scale associated with building up the reaction force is short compared to the physical time scale a/V_s which determines how fast the fluid velocity can change. On times scales longer than a/V_s we can thus consider the no-slip boundary condition as being satisfied.

Correspondingly the total coupling force and torque acting to the template i can be calculated as

$$\mathbf{F}_i^c = -\sum_{l=1}^{n_i} \mathbf{f}_{il}^c; \tag{4.25}$$

$$\boldsymbol{\tau}_i^c = -\sum_{l=1}^{n_i} \mathbf{f}_{il}^c \times \mathbf{O}_i(t) \cdot \tilde{\boldsymbol{\xi}}_{il}. \tag{4.26}$$

The templates T_i also serve to include the inertial contributions of the physical particles which arise when particle and fluid densities differ. We define m_i^f as the fluid mass "inside" the particle and the "missing" mass $m_i^t = m_i - m_i^f$. The templates then execute rigid body motion according to the equation of motion,

$$m_i^{\mathrm{t}} \dot{\mathbf{v}}_i = \mathbf{F}_i^p - m_i^{\mathrm{t}} g \hat{\mathbf{e}}_z + \mathbf{F}_i^c. \tag{4.27}$$

We note that, by itself, due to the different mass and additional force term $\mathbf{F}_i^c$, Equation (4.27) is *not* equivalent to the particle equation of motion (4.20). Also, for neutrally buoyant particles the inertial term in (4.27)

vanishes and we must compute instead the template position directly (which appears implicitly in $\mathbf{F}_i^c$) from the force and the torque in equilibrium.

To obtain the total force acting to the body we have to add the total forces acting to the template and to the region Ω_i of the fluid. According to Eq. (2.11) the latter is

$$\mathbf{F}_i^{\text{fluid}} = \oint_{\partial\Omega_i} \boldsymbol{\sigma} \cdot d\mathbf{A} - \mathbf{F}_i^c, \tag{4.28}$$

where the first integral is calculated over the surface of Ω_i and the last term is obtained by integrating $\mathbf{f}_i^c$.

Adding the equation of motion of the template (4.27) and of Ω_i [Eq. (4.28)], we see that the internal constraint forces $\mathbf{F}_i^c$ cancel, leaving only external forces

$$(m_i^t + m_i^f)\dot{\mathbf{v}}_i = m_i\dot{\mathbf{v}}_i = \oint_{\partial\Omega_i} \boldsymbol{\sigma} \cdot d\mathbf{A} + \mathbf{F}_i^p - m_i^t g\hat{\mathbf{e}}_z. \tag{4.29}$$

To the degree that the penalization guarantees that Ω_i has the shape of the modeled particle, the surface integral occurring in Eq. (4.28) is equal to the hydrodynamic force $\mathbf{F}_i^{\text{hd}}$ of Eq. (4.20) for the physical fluid-particle interaction. Noting that $m_i^t = m_i\Delta\rho/\rho_p$ we thus recover the equation of motion (4.20) for a rigid body suspended in the fluid.

The arguments above can be repeated for the angular motion. Considering the i th template to have a moment of inertia $I_i^t = I_i - I_i^f$, we demand that

$$\mathbf{I}_i^{\text{t}}\dot{\boldsymbol{\omega}}_i = \boldsymbol{\tau}_i^p + \boldsymbol{\tau}_i^c, \tag{4.30}$$

where $\boldsymbol{\tau}_i^p$ refers to the torque arising from the short range body contacts. In analogy to (4.28) we obtain the total hydrodynamic torque on the "inside" fluid if we operate with $\mathbf{r}_i\times$ on the momentum equation (4.28) and then integrate over Ω_i. Adding the resulting equation to (4.30), the torques due to the constraints cancel in the limit of large k' and we recover the relation for the angular motion of the particle (4.21).

So far we have not restricted the shape of the immersed bodies, or T_i, in any way. To produce the fluid-body coupling for bodies with arbitrary shape, we need just a method to distribute the marker positions $\{\tilde{\boldsymbol{\xi}}\}$ over the template. In principle there are many possible ways to do it. We want to make few remarks. First, it is important that the markers have roughly same density than the lattice points. Otherwise the body is either leaking or

the fluid motion has too many constraints. Second, if the body has certain symmetry, it is natural to try to use the same symmetry in distributing the markers.

We must still specify the force $\mathbf{F}_i^p$ due to close pair interaction. At sufficiently low Reynolds numbers, we know from lubrication theory that the presence of the fluid prevents smooth particle surfaces from touching. At very small distances, when particles approach each other on a path perpendicular to their surface at a fixed velocity, the stresses necessary to displace the fluid are inversely proportional to the distance between the surfaces. These forces are captured correctly only on scales larger than the grid resolution. Since we will here work with dilute systems in terms of the volume fraction, we consider close particle encounters to be rare. We thus do not attempt to model lubrication forces, but introduce an elastic restoring force which prevents significant template overlaps. From our experience with suspensions of spheres [76], we think that lubrication effects are not important for the collective settling behavior up to volume fractions of ≈ 0.15

The force between two colliding particles is taken to be proportional to the amount of their mutual virtual overlap. For non-overlapping particles this force is set to zero. As a further justification for using the elastic particle-particle interaction, it can be assumed that the short range diverging lubrication forces deliver the elastic behavior of the particles even if they are not in true contact.

In our work we restricted to study the suspension of spherical and spheroidal particles. For spheres the elastic collision force is trivial but for spheroidal particles it becomes more complicated. To model the collision between two spheroids we have employed the method described by Perram et al. [136, 137], who define a contact function

$$C_{ij} = \max\left\{4\lambda(1-\lambda)\mathbf{X}_{ij}^T\mathbf{G}_{ij}^{-1}(\lambda)\mathbf{X}_{ij}|\lambda \in [0,1]\right\}. \tag{4.31}$$

for two spheroids i and j. Here, $\mathbf{X}_{ij} = \mathbf{x}_i - \mathbf{x}_j$ is the distance between the centers of mass of the spheroids, and the matrix $\mathbf{G}_{ij}(\lambda)$ is defined as

$$\mathbf{G}_{ij}(\lambda) = (1-\lambda)(\mathbf{O}_i^T\mathbf{R}_i^2\mathbf{O}_i)^{-1} + \lambda(\mathbf{O}_j^T\mathbf{R}_j^2\mathbf{O}_j)^{-1}. \tag{4.32}$$

The diagonal matrix $\mathbf{R}_i$ contains half the axes of the respective spheroid i. At contact the function C_{ij} is unity and lower values indicate overlap. The chosen contact function is not isotropic at large particle separations, but this causes no problem, since we set the force to zero for non-overlapping

particles. It is easy to construct the elastic contact potential from C_{ij} and the contact force can be computed from its derivative.

The method is quite efficient and we have produced simulations with up to order 10^5 spherical particles or order 10^4 spheroidal particles. The method is suitable to study systems with $\mathrm{Re}_p \lesssim 10$, although the methods slows down with very small Reynolds numbers. The method does not restrict the shape of the embedded bodies. It does require, however, that a short range contact potential between the bodies can be constructed. We have used a code that has been developed in the Institute of Computer Applications, University of Stuttgart, Germany. A detailed description of the implementation of the code can be found in Refs. [76, 77].

Chapter 5

Results

We will now give the summary of our work related to the sedimentation of monodisperse suspension with finite Reynolds number. In most cases we have chosen $\mathrm{Re}_p = \mathcal{O}(1)$. Our aim is to study the region where the flow is laminar in the particle length scales, but where the system size based Re is large compared to unity.

A direct consequence of a finite Re_p, and the relatively small system sizes we can study with our methodology, is that some corrections have to be made in order to compare the results to the previous work done in the limit $\mathrm{Re}_p \ll 1$ and in larger systems. Our test with a single sedimenting particles show that the finite Re_p corrections are well comparable to Eqs. (2.36) and the correction derived by Breach [22]. Similarly, the finite size effect for the terminal velocity of single sphere follows reasonably well the corrections calculated by Hashimoto [69], and later by Zick and Homsy [176].

To interprete our results we have chosen a strategy to understand the corrections described above as trivial re-scaling of the velocities. To explain the more interesting discrepancies between our results and previous studies in small Reynolds number limit we need to understand the new phenomena rising from the inertial effects, such as the lift force described in Eq. (2.38) or the inertial torque (Eq. (2.40)) affecting sedimenting spheroids. As a consequence of these phenomena it will come evident that the statistical structure of the suspension undergoing sedimentation under finite Re_p conditions cannot be approximated by $g_{\mathrm{eq}}(\mathbf{r})$.

We have not, however, limited our studies to find out how the inertial effects

alter the known $\mathrm{Re}_p = 0$ results but we have also chosen our subjects of study so that they are interesting in their own right.

We will first discuss the particle velocity distribution giving special attention to its non-Gaussian aspects. To explain these we study the relation between the velocity of a test particle and the particle density fluctuations around it. Finally we discuss the particle motion by considering it as a generalized diffusion process.

In the second section we study the effects produced by the container walls and the finite size of the system. We show that the finite Re_p particle-wall interaction enhances the intrinsic convection and show how the sedimentation velocity depends on the system size. We will end the discussion with results concerning the scaling of the velocity fluctuations.

Finally, we consider the sedimentation of spheroidal particles. We explain the non-monotonic average sedimentation velocity by considering the changes in pair correlation function and orientational preferences. We will discuss in detail the orientational transition and its connection to the density fluctuations. In the end we briefly give results concerning the sedimentation of oblate spheroids.

To reduce the parameter space we represent the results in dimensionless units that are quite standard in the field. Units of length are divided by the smallest dimension describing the particle which in the case of a sphere means the radius a. Units of density are divided by by the density of the fluid ρ_l and units of velocity by the Stokes velocity V_s. We want to note that in the finite systems V_s is larger than the sedimentation velocity of a single particle in a given system (denoted by V_0).

We restrict the studies to the steady-state sedimentation. Reaching the steady-state could take a significantly long time and during this initial period the evolution of the system could undergo several different phases. We have thus used several quantities to verify that steady state has been reached in all cases.

5.1 Velocity Distribution of Spheres

A central quantity to study the sedimentation of N particles is the *particle velocity distribution* defined as

$$P(\mathbf{v}) = \langle N^{-1} \sum_{i=1}^{N} \delta(\mathbf{v} - \mathbf{v^i}) \rangle, \tag{5.1}$$

where $\mathbf{v^i}$ is the velocity of particle i. Due to the spatial anisotropy, it is necessary to divide the particle velocities to components parallel and perpendicular to gravity, denoted by $v_\parallel$ and $v_\perp$, respectively. In most works the description of $P(v_\parallel)$ and $P(v_\perp)$ is reduced to their first and second moments, as described in sections 3.3 and 3.4. We will now study these distributions in more detail to fathom also the non-Gaussian behavior of the velocity distributions in the case of finite Re_p sedimentation. The data shown here are for a suspension of monodisperse spherical particles whose density is 2.5 times the fluid density. The size of the system used in this work is $32 \times 32 \times 64$ in units of the radius of the particles, where the larger dimension is in the direction of gravity and periodic boundary conditions are used in all directions. We fixed the fluid viscosity so that the particle Reynolds number $\mathrm{Re}_p \approx 0.5$.

We will first study the shape of the distributions and then explain their non-Gaussian behavior by considering the concentration of other particles in the vicinity of the test particle. Finally, we consider the diffusive motion of the sedimenting particles.

5.1.1 The Shape of the Velocity Distribution Function

Since our main interest here is to study the shape of $P(v)$ we do not use the normal laboratory coordinates where the total volumetric flow vanishes. Instead we measure the particle velocities in a coordinate frame moving downward with a velocity v_f so that $\langle v_\parallel \rangle = 0$. This mimics the fluidized bed experiments with average fluid velocity $(1 - \Phi)^{-1} v_f$ upward. According to its definition, v_f should obey the RZ law of Eq. (3.2) and in Fig. 5.1 we show that in overall this is the case. The difference in small volume fraction Φ can be explained by the inertial effects: As predicted by Koch [96] we found a region of reduced average particle density in the direction of gravity from

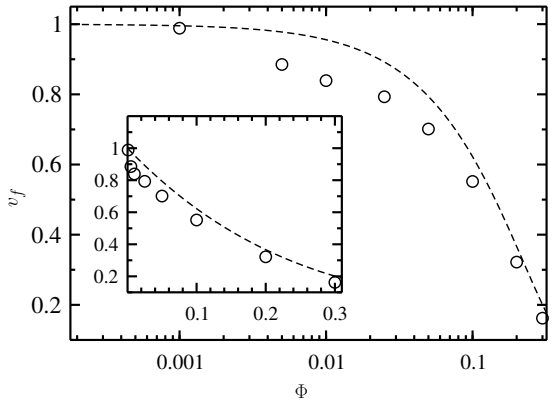

Figure 5.1: The average velocity of the frame v_f as a function of the volume fraction Φ. The frame velocity has been chosen so that that the average particle velocity is zero. The dashed line corresponds to the RZ law with exponent 4.5. The same data are also shown in the inset with linear x axis.

the test particle. This is demonstrated in Fig. 5.2, where we have plotted $\Phi/(3a)\int_{3a}^{6a} g(r,\theta)dr$ as a function of $\cos\theta$ for two different Φ. Here θ is the angle between $\mathbf{r}$ and the direction of gravity. The pair distribution function $g(\mathbf{r})$ is determined by Eq. (3.1) Koch showed also that this depletion regime then reduces the average sedimentation velocity.

The actual velocity distributions $P(v_\parallel)$ from simulations with three different Φ are shown in Fig. 5.3. Two observations can be made immediately. First, the variance (*i.e.* the velocity fluctuations) $\sigma^2(v_\parallel) = \langle v_\parallel^2 \rangle = \int v_\parallel^2 P(v_\parallel) dv_\parallel$ has significantly different values for different Φ. Second, the non-Gaussian features of $P(v_\parallel)$ undergo a systematic change: for the smallest $\Phi = 0.005$ (dashed line), the distribution is non-Gaussian with a longer tail in the direction of downward velocities while for a system with $\Phi = 0.30$[1] the distribution is skewed to the opposite direction.

The velocity fluctuations have been studied intensively as described in subsection 3.4.1 and here we compute $\sigma(v_\parallel)$ and $\sigma(v_\perp)$ just to verify how well our finite Re_p results coincide the results obtained in $\mathrm{Re}_p = 0$ limit. For the velocity fluctuations scaled by v_f we find scaling as Φ^m with $m \approx 0.50$ for $\sigma(v_\parallel)$ and 0.55 for $\sigma(v_\perp)$, which fit well with the previous results [28, 131].

To quantify the non-Gaussian nature of P we have computed also its 3rd

[1]It should be noted that $\Phi = 0.3$ is quite a large value to be treated with our simulation method and thus the results might contain some numerical errors.

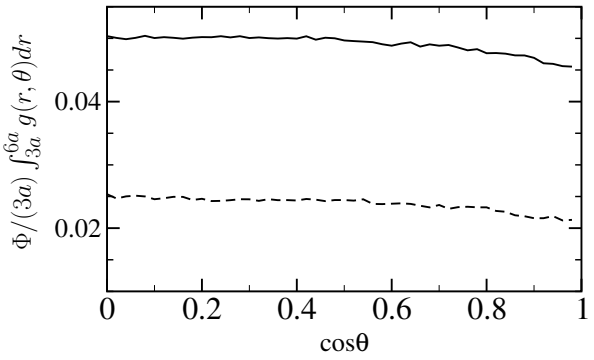

Figure 5.2: The θ dependence of the pair correlation function. See text for details.

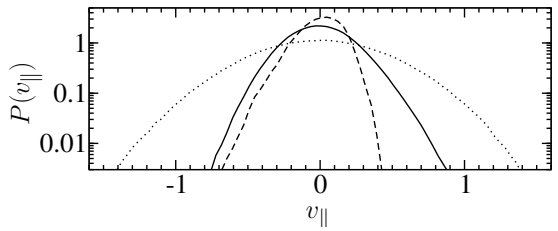

Figure 5.3: The vertical velocity distributions $P(v_\parallel)$ for three different volume fractions: $\Phi = 0.005$ (dashed line), 0.05 (dotted line) and 0.30 (solid line).

and 4th moments. The *skewness* $\gamma_1 = \mu_3/\mu_2^{3/2}$, where $\mu_n(v) = \langle (v)^n \rangle$, measures the asymmetry of the distribution. For symmetric distributions, such as for $P(v_\perp)$, $\gamma_1 = 0$. In Fig. 5.4 (a) we show $\gamma_1(v_\parallel)$ up to $\Phi = 0.3$. The systematic change from negative to positive values of γ_1 is evident, and in accordance with Fig. 5.3 the distribution is symmetric at $\Phi \approx 0.05$.

The *kurtosis,* which describes the weight of the tails of the distribution, is defined as $\gamma_2 = \mu_4/\mu_2^2 - 3$ so that it is zero for a Gaussian distribution. A positive γ_2 denotes that the distribution decays slower than Gaussian distribution. In Fig. 5.4 (b) we show $\gamma_2(v_\parallel)$. We can see that the tails are most extended for small volume fractions, while again around $\Phi \approx 0.05$, $\gamma_2 \approx 0$. For larger Φ, the tails become extended again. For completeness, in the inset of Fig. 5.4 (b) we also show $\gamma_2(v_\perp)$ for the horizontal distribution. It can be seen that its tails are also extended and correlate with the changes in $P(v_\parallel)$. The results have a good qualitative agreement with the previous studies[83, 126, 154].

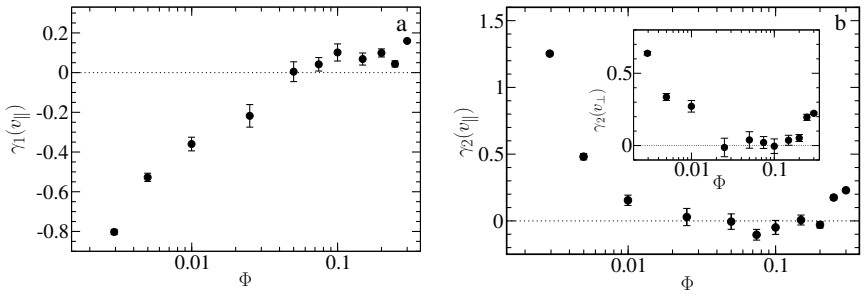

Figure 5.4: (a) The skewness γ_1 of $P(v_\parallel)$. (b) The corresponding kurtosis $\gamma_2(v_\parallel)$. The kurtosis of the horizontal velocities $\gamma_2(v_\perp)$ is shown in the inset.

5.1.2 Local Volume Fraction

Next we will discuss the physical reasons behind the vertical distributions. Since the velocity fluctuations have been associated to the length scale of the particle density fluctuations [28, 74, 157] we will seek the origin of the non-Gaussian distributions from the density fluctuations, too.

To quantify the density inhomogeneities we define a *local volume fraction* ϕ as the number of particles within a certain region Ω_n around a test particle, multiplied by the ratio of the one-particle volume and the volume of the region. The choice of the shape and size of Ω_n is somewhat arbitrary but our aim is to choose Ω_n so that its size corresponds the characteristic size of the particle density fluctuations, if any such size exists. In many works the characteristic size of density fluctuations (or particle clusters) has been used to explain the density fluctuations [74, 156, 157]. Here we have chosen the opposite strategy and have defined the characteristic size so that it explains the velocity fluctuations. The shape of the region was chosen to be spheroidal with a possibly different radius in the direction parallel to the gravity. The size of the region has been chosen such that ϕ correlates as much as possible with the vertical velocity. This can be achieved by maximizing the square of the normalized cross correlation between ϕ and $v_\parallel$, defined by

$$c^2_{v_\parallel,\phi} = \frac{\big(\langle v_\parallel \phi\rangle - \langle v_\parallel\rangle\langle\phi\rangle\big)^2}{\sigma^2(v_\parallel)\sigma^2(\phi)}. \tag{5.2}$$

We found that a spheroidal region of size $11 \times 11 \times 20$ maximizes $c^2_{v_\parallel,\phi}$ with a good degree of approximation for all values of Φ studied here. The values for $c^2_{v_\parallel,\phi}$ vary from 0.20 for $\Phi = 0.005$ to 0.25 for $\Phi = 0.30$.

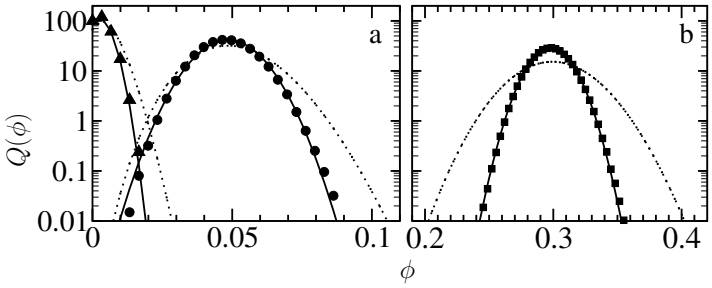

Figure 5.5: The distributions of the local volume fraction from the simulations with $\Phi = 0.005$, 0.05 (triangles and circles in a) and 0.30 (squares in b). Gaussian fits are shown with solid lines. The corresponding distributions for uniformly random configurations are shown with dotted lines.

The local volume fraction distributions $Q(\phi)$ are shown in Fig. 5.5 for different values of Φ. As expected, $Q(\phi)$'s are Gaussian and their maxima coincide with the total volume fraction. However, the distributions $Q(\phi)$ are much narrower than those corresponding to uniformly random configurations. This is in a good agreement with the observed depletion regime in $g(r, \theta)$, and also with the experiments of Lei *et al.* [113] about the particle number fluctuations during sedimentation.

Intuitive explanation for the connection of density and velocity fluctuations is that a region of large local density behaves like a blob of heavier fluid obtaining a downward velocity relative to the surrounding fluid [74, 157]. This is demonstrated in Fig. 5.6 where we show the dependence of the average vertical velocity of particles with fixed ϕ, $\langle v_\parallel \rangle_\phi$, for several different total volume fractions Φ. Based on these data, we can write the total velocity for particle i as $v_\parallel^i = \langle v_\parallel \rangle_\phi + \delta v_\parallel^i$, where $\langle v_\parallel \rangle_\phi \approx c(\Phi - \phi)$ describes the part of the velocity that is determined by ϕ, and $\delta v_\parallel^i$ is the part of velocity that is induced by all the other factors *e.g.* details of the particle configuration (here c is a positive Φ dependent coefficient). To quantify this, we define the remaining *residual velocity fluctuation* (RVF) as $\sigma_\phi(v_\parallel) = \sqrt{\langle \delta {v_\parallel}^2 \rangle_\phi} = \sqrt{\langle {v_\parallel}^2 \rangle_\phi - \langle v_\parallel \rangle_\phi^2}$. These data for different values of Φ are shown in Fig. 5.7. The fluctuations are smallest for small and large volume fractions, and have a maximum around $\phi \approx 0.08$.

We would like to complete the description above by two remarks. First, it is possible to approximate the coefficient c by following the steps proposed by Segré [157]. We start by assuming that a spheroidal blob with the given

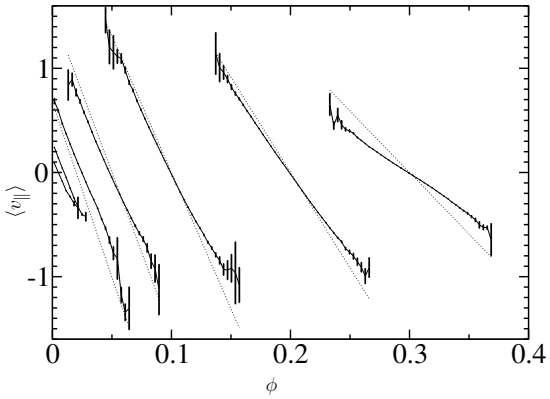

Figure 5.6: The average vertical velocity of the particles as a function of ϕ with fixed total volume fractions (from left to right): $\Phi = 0.005$, 0.01, 0.02, 0.05, 0.10, 0.20, and 0.30. The dotted lines present the relation obtained by the blob model.

size and additional mass density proportional to $(\phi - \Phi)$ is descending (or ascending) relative to the other fluid. The frictional force acting to the blob is obtained from Eq. (2.23) by replacing η with $\eta(\Phi) = \eta(1 - \Phi/0.71)^{-2}$ to take account the increase of friction due to the presence of the other particles [40]. Since in our model the blob occupies a remarkable amount of the total simulation volume the finite size correction is large. We have estimated it to be around 5.3 by using Hasimoto's result [69]. Combining these results it is clear that $\langle v_\parallel \rangle_\phi \propto (\Phi - \phi)$ and the proportionality factor c can be calculated. The values of c, corresponding the blob model, are shown in Fig. 5.6 by thin dotted lines and the agreement to the measured average velocities is remarkably good.

Second, more detailed study of the RVF's shows that the non-Gaussian behavior found in the original $P(v_\parallel)$ has disappeared *i.e.* the skewness and kurtosis calculated from the distribution of $\delta v_\parallel$ with fixed ϕ are most cases negligibly small compared to $\gamma_1(v_\parallel)$ and $\gamma_2(v_\parallel)$. We take this as a further proof that there is a characteristic size of density fluctuations. In this light it might have been better not to fix the size of the region used to calculate ϕ but let it change as a function of Φ.

The behavior of the distributions $P(v_\parallel)$ can now be explained by the ϕ dependence of the RVF's. Namely, the whole function $P(v_\parallel)$ can be obtained by summing up the velocities of all the particles with different ϕ's. Since the $Q(\phi)$'s are Gaussian, and $\langle v_\parallel \rangle_\phi$ depends linearly on ϕ, $P(v_\parallel)$ would be

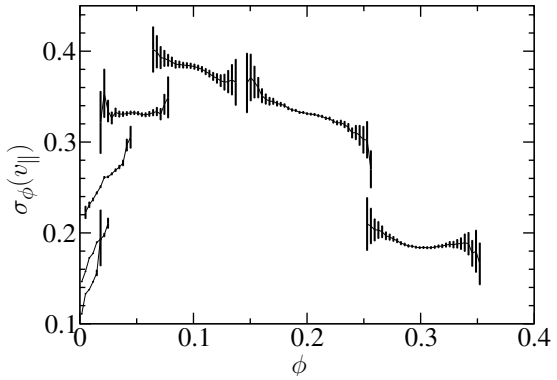

Figure 5.7: The RVF's in the direction parallel to gravity as a function of ϕ. From left to right the data are for fixed values of $\Phi = 0.005$, 0.01, 0.02, 0.05, 0.10, 0.20, and 0.30.

Gaussian, too, if the RVF's did not depend on ϕ. For dilute suspensions we can see from Fig. 5.7 that the RVF's increase strongly with ϕ, which means that the fluctuations in the downward velocity part of $P(v_\parallel)$ are enhanced, in accordance with our data. For the opposite case of suspensions denser than $\Phi \approx 0.05$, the RVF's decrease with increasing ϕ, and thus there are enhanced fluctuations in the opposite (upward) direction. This explains the systematic change in the sign of the skewness of $P(v_\parallel)$ as a function of Φ.

The dependence of the RVF's on ϕ can be understood by considering the region around a test particle. In a system with very low Φ a larger ϕ would produce larger disturbance for the particle and thus lead to a larger RVF. On the other hand in the dense system the motion of the test particle is restricted by the surrounding particles. Thus particles with larger ϕ have a reduced RVF due to the increased blocking.

We note also that the non-Gaussian behavior of $P(v)$ undermines the use of the concept of "temperature" in sedimentation even though it's often used in the context of granular media [29]. Our results also show that the concept of "gravitational temperature" introduced recently by Segrè *et. al.* [157] can only be used to explain the part of $P(v_\parallel)$ coming from the dependence of $v_\parallel$ on local density ϕ.

5.1.3 Diffusion

We will next study the diffusive motion of the sedimenting particles. The tracer diffusion coefficient depends not only by the velocity fluctuations but also how fast the particles are changing their relative motion.

In this subsection we report results that have been obtained with a very simplified two-dimensional FDM model where the fluid-particle coupling has been realized by using Eq. (2.19) to produce a point force acting to the fluid. Details of the model can be found in Ref. [155]. All simulations are done in a square box with linear size $L = 132$ and with particle density $\rho_p = 2$.

To create some confidence that the simple 2D model can describe the sedimentation qualitatively we have plotted in Fig. 5.8 the average sedimentation velocity $\langle v_\parallel \rangle$ and the average velocity fluctuations

$$\sigma^2(v_\parallel) = \langle v_\parallel^2 \rangle - \langle v_\parallel \rangle^2; \quad \sigma^2(v_\perp) = \langle v_\perp^2 \rangle, \tag{5.3}$$

as a function of Φ^2. Here $\langle v_\parallel \rangle$ has been calculated using $\mathrm{Re}_p = 0.02$ and 0.03 and the velocity fluctuations using $\mathrm{Re}_p = 0.02$. Qualitative agreement to 3D simulations is good. The average sedimentation velocity is a monotonous function with clear resemblance to 3D results, although the RZ law is not strictly followed. Note that the low Φ limit results of $\langle v_\parallel \rangle$ are clearly below unity since velocities are normalized by V_s instead of V_0.

Similarly the velocity fluctuations show qualitatively same behavior than in 3D cases by increasing with increasing Φ. The fluctuations parallel to gravity are also much larger than the perpendicular fluctuations.

At this point we note that a careful study of the dilute limit behavior of $\langle v_\parallel \rangle$ reveals a restriction of the simple model used here: since there is no coupling between the fluid and the rotational motion of the particles, no lift force is generated. This is evident in $g(r, \theta)$ shown in Ref. [101] where there is a region of *increased* particle density above the test particle contradicting our results in the previous subsection. Rather than reducing the average sedimentation velocity, this region of increased density enhances $\langle v_\parallel \rangle$ in the dilute limit.

A fundamental quantity characterizing the dynamical behavior of the sedimenting particles is the *velocity (fluctuation) autocorrelation function* (VACF),

[2]Here we have defined the volume fraction as $(4/3)\pi N/(2L^2)$.

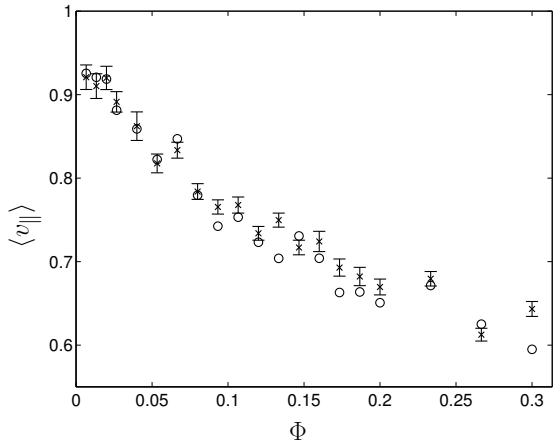

Figure 5.8: The mean sedimentation velocity $\langle v_\parallel \rangle$ as a function of the volume fraction Φ. Crosses and circles denote particle Reynolds numbers 0.02 and 0.03, respectively.

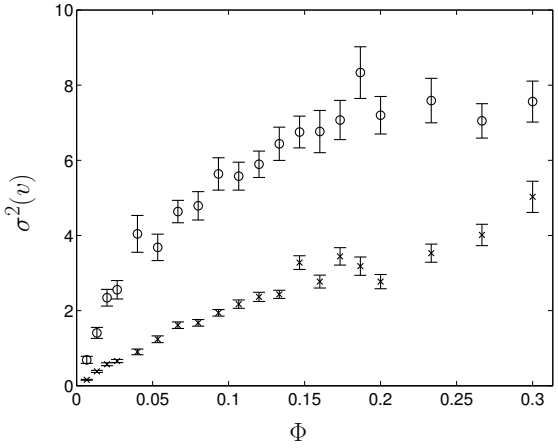

Figure 5.9: Velocity fluctuations of Eq. (5.3) parallel (circles) and perpendicular (crosses) to gravity with $\mathrm{Re}_p = 0.02$.

$C(t)$, defined in Eq. (3.13). With the present anisotropic case, we separate $C(t)$ into its parallel and perpendicular components with respect to gravity $C_\parallel(t)$ and $C_\perp(t)$, respectively. In Fig. 5.10 we show the corresponding (normalized) functions $C_\parallel(t)$ and $C_\perp(t)$ corresponding to the volume fractions $\Phi = 0.0266, 0.0534, 0.133$ and 0.267. The anisotropy is evident in the slower rate of decay of the parallel component which also remains positive for all times with the statistical errors. As the volume fraction increases $C_\parallel$ de-

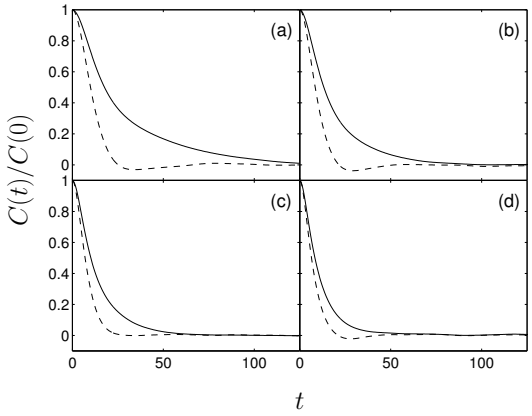

Figure 5.10: Normalized velocity fluctuation autocorrelation functions $C_{\parallel}(t)/C_{\parallel}(0)$ (solid lines) and $C_{\perp}(t)/C_{\perp}(0)$ (dashed lines) for (a) $\Phi = 0.0266$, (b) 0.0534, (c) 0.133, and (d) 0.267 ($\mathrm{Re}_p = 0.02$).

cays more rapidly but also the difference between the two functions becomes smaller. We note that for smaller Φ's our results are in good qualitative agreement with those of Ladd [107] using the lattice Boltzmann approach with periodic boundaries.

The decay rate of the autocorrelation function can be quantified by calculating the autocorrelation time

$$\tau = \int_0^\infty \frac{C(t)}{C(0)} dt. \tag{5.4}$$

The autocorrelation times $\tau_{\parallel}$ and $\tau_{\perp}$ are shown in Figs. 5.11 (a) and (b), respectively. We find that to a good degree of accuracy, $\tau_{\parallel}$ decays in a power law fashion as $\tau_{\parallel} \propto \Phi^{-\alpha}$, with $\alpha = 0.45 \pm 0.05$. Within the accuracy of the data, we find no similar power-law for $\tau_{\perp}$.

The dominance of the hydrodynamic interactions in our model makes it interesting to study the time dependence of the VACF's. It has been recently shown that for a 2D dissipative hard-sphere fluids [99] and some strongly interacting 2D adsorption systems [175, 75, 167], $C(t)$ displays an intermediate power-law decay $C(t) \sim t^{-x}$, where the exponent x typically gets values $1 \lesssim x \lesssim 2$ depending on the range and type of interactions (attractive or repulsive). In the present case, we do not find such simple behavior. However, since by definition $C(t = 0) = \sigma^2(v)$ is finite, we can try to describe the VACF's by

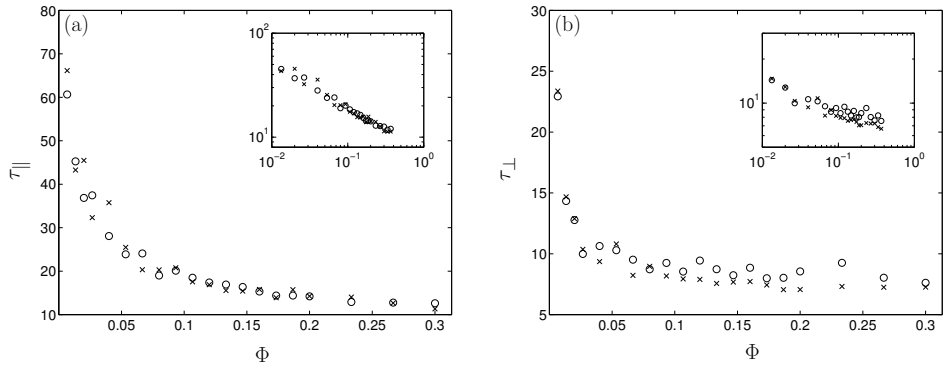

Figure 5.11: The autocorrelation times as a function of Φ for $\mathrm{Re}_p = 0.02$ (circles) and 0.03 (crosses) for (a) $\tau_\parallel$ and (b)$\tau_\perp$. In both cases the inset shows the data on a log-log scale.

$$C(t) = \frac{C(0)}{1 + At^x}, \tag{5.5}$$

which would asymptotically give $C(t) \sim t^{-x}$, for $At^x \gg 1$. In Figs. 5.12 (a) and (b) we show $[C_\parallel(t)/C_\parallel(0)]^{-1} - 1$ and $[C_\perp(t)/C_\perp(0)]^{-1} - 1$ as a function of time t on a log-log scale for several volume fractions Φ. The parallel component of $C(t)$ shows well-defined power law behavior over about two orders of magnitude in time which indicates that Eq. (5.5) is indeed a good approximation for the parallel VACF for the times shown in the figure. The inset of Fig. 5.12 (a) shows results of least squares fitting to the logarithmic data. The effective exponent $x \approx 2$ is almost independent of the volume fraction and in the same range as results for strongly repulsive dissipative systems [75, 167]. For the perpendicular component, the effective power law is not as well-defined, and the exponent $x \approx 2.3$, again indicating that repulsive interactions dominate [75, 167]. In both cases, the late-time behavior becomes eventually exponential as expected.

A fundamental quantity characterizing the dynamics of single particles is the tracer diffusion coefficient D as defined through the Green-Kubo formula of Eq. (3.14). Using the definition of the correlation time τ, this equation can also be written as

$$D = \tau\sigma^2(v). \tag{5.6}$$

In Figs. 5.13 (a) and (b) we show the diffusion coefficients $D_\parallel$ and $D_\perp$ *vs.* Φ corresponding to the parallel and perpendicular correlation functions

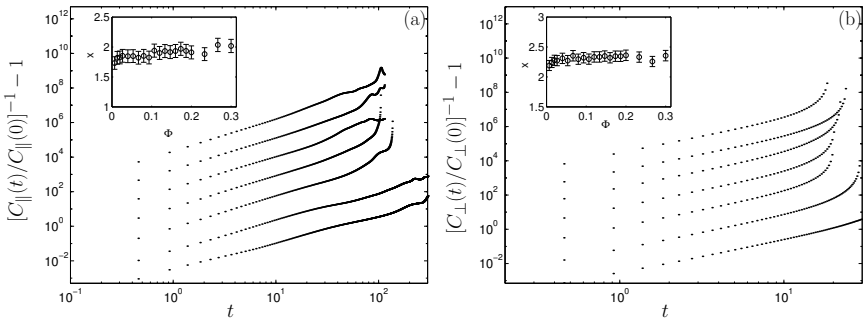

Figure 5.12: Results for (a) $[C_\parallel(t)/C_\parallel(0)]^{-1}-1$ and (b) $[C_\perp(t)/C_\perp(0)]^{-1}-1$ *vs.* t/t_s shown in log-log plots ($\mathrm{Re}_p = 0.02$). The curves show different volume fractions $\Phi = 0.0066,\ 0.0266,\ 0.0667,\ 0.133,\ 0.200,\ 0.267,\ 0.367$, from bottom to top. In each case, inset shows results of least-squares fit of the data to the form t^x. See text for details.

$C_\parallel$ and $C_\perp$, respectively. Due to significant finite size effects of the velocity fluctuations [130, 107], it is difficult to compare their absolute values to other results [105, 131]. However the overall behavior of the two components of D as a function of Φ is similar to the experimental results in 3D [130] with small values of Φ. The parallel component $D_\parallel$ increases first strongly with Φ, and then decreases slightly for larger volume fractions. In the experiments this is also qualitatively observed [130], but the decrease is much more dramatic. Recent experiments in 2D claim that the behavior along the direction of gravity may be super-diffusive [154].

The ratio between the diffusion coefficients in the different directions $D_\parallel/D_\perp$ is shown in Fig. 5.13 (c) for two Reynolds numbers $\mathrm{Re}_p = 0.005$ and $\mathrm{Re}_p = 0.03$. As found experimentally [130], the ratio between the two diffusion coefficients decreases with increasing Φ and depends strongly on Re_p. In our studies the decrease for smaller Re_p is more pronounced than in experiments [130] where the ratio for small Φ is much smaller. The same result has been obtained in other numerical simulations [107] and it has been suggested that the periodic boundaries are at least partially the reason for this. In the experiment the ratio increases with very small volume fractions ($\Phi < 0.10$). From our data we cannot conclusively verify this due to the error bars.

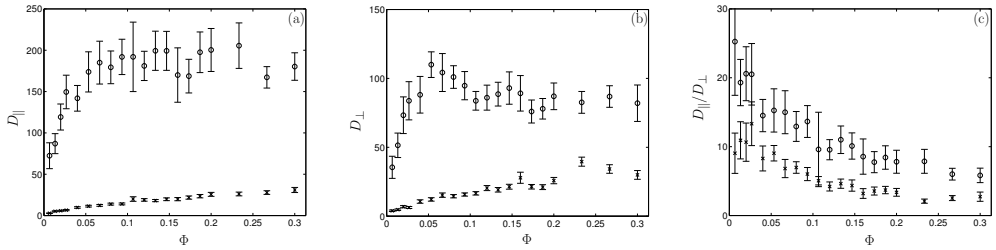

Figure 5.13: (a) Results for the tracer diffusion coefficients $D_{\|}$ (circles) and $D_{\perp}$ (crosses) for (a) $\mathrm{Re}_p = 0.005$ and (b) $\mathrm{Re}_p = 0.03$. (c) The ratio $D_{\|}/D_{\perp}$. The case of $\mathrm{Re}_p = 0.005$ is denoted by circles and $\mathrm{Re}_p = 0.03$ with crosses.

5.2 Sedimentation in Confined Geometry

We have so far neglected discussion about the finite size of the system. However, as explained in section 3.4.1 the velocity fluctuations depend on the system size in many cases. Other question that has not been addressed yet is how the container walls influence the finite Re_p sedimentation.

To answer these questions we will next study a system, where the suspension is confined between two parallel vertical walls while periodic boundaries are used in the other directions. Since the horizontal directions are no more identical we are changing our notation in this section as shown in Fig. 5.14: the direction of gravity is chosen as the negative z axis, the system is restricted by the walls in the direction of the x axis, and the y axis points to the remaining horizontal direction, where periodic boundary conditions are applied. The distance between the walls is denoted by L_x. The linear system size in y and z directions is set to equal and denoted by L_{periodic} $(= L_y = L_z)$.

When the separation of the walls increases the system changes from a quasi-2D setup to a 3D container. We study the influence of the wall friction and the change in the spatial degrees of freedom here, when crossing over from the quasi-2D limit to 3D. All simulations are performed using $\mathrm{Re}_p = 0.5$. We will first examine the particle density distribution between the walls and then discuss the average sedimentation velocity. Finally, we consider the velocity fluctuations and diffusion.

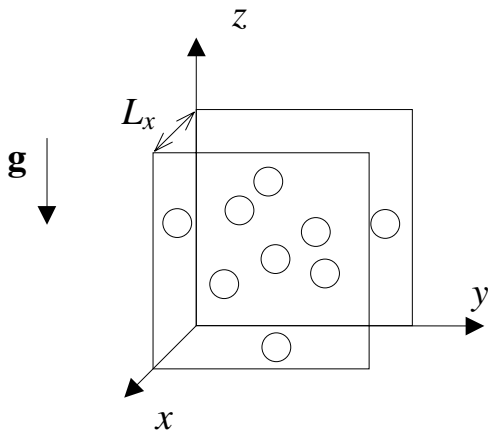

Figure 5.14: A schematic figure of the geometry of a finite aperiodic sedimentation box. The direction of gravity is along the negative z axis, with periodic boundary conditions in both the z and y directions. The confining walls with a variable spacing L_x are placed in the x direction.

5.2.1 Particle density distribution

In Fig. 5.15 we present the particle number density distribution function

$$f(x) = \langle \frac{L_x}{N} \sum_{i=i}^{N} \delta(x - x^i) \rangle \tag{5.7}$$

between the walls with two different values of L_x and Φ. Here x^i denotes the x coordinate of particle i measured from the middle of the system. The data are normalized such that particle density $f(x) = 1$ corresponds to a particle density in an infinite system with a spatially uniform distribution with the same volume fraction. In both quasi-2D (Fig. 5.15 (a)) and $L_x = 23.11$ cases (b) the particles in a dense suspension are distributed quite evenly except for an excess density next to the wall. The vertical dotted line represents the value of x where the particle touches the wall. With wall spacing $L_x = 23.11$ the shape of $f(x)$ in the vicinity of the wall closely follows the Percus-Yevick distribution, which is in a good agreement with the low Re_p results found by Peysson and Guazzelli [139].

As shown for $\Phi = 0.025$ (dashed line in Fig. 5.15 (a)), in the dilute limit $f(x)$ differs from both the low Re_p experiments [139] and the Percus-Yevick distribution. Most conspicuous difference is the distinct depletion layer which

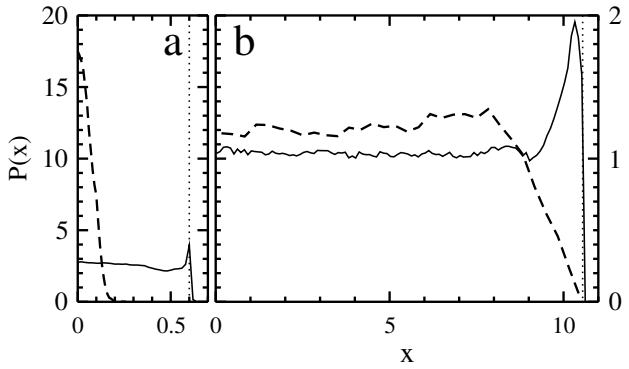

Figure 5.15: Normalized particle number density as a function of the x coordinate measured from the middle of the system: (a) wall spacing $L_x = 3.2$, $\Phi = 0.025$ (dashed line), $\Phi = 0.225$ (solid line). (b) $L_x = 23.11$, $\Phi = 0.025$ (dashed line), $\Phi = 0.152$ (solid line). The vertical dotted line marks the distance of one particle radius away from the wall. Note the difference in the vertical scales between (a) and (b).

extends several particle radii away from the wall. In the case of small L_x, all the particles are concentrated close to the center of the container. To quantify the depletion layer, we define an *effective width* $L_x^{eff} = 4\int_0^{L_x/2} f(x)xdx$. With this, the width of the depletion layer is defined as $\zeta_x = 1/2(L_x - L_x^{eff})$. As can be seen from Fig. 5.16, when Re_p is kept constant, ζ_x is only a function of Φ, provided that the width of the system is large enough. Furthermore there seems to be a power-law scaling $\zeta_x \sim \Phi^{-m}$, with the fitted exponent $m \approx 0.60$.

The existence of the depletion layer and the behavior of ζ_x is easy to understand qualitatively. In a region of finite Re_p, a particle sedimenting between two infinite vertical walls is shown by Vasseur and Cox [166] to migrate away from the closer wall due to a repulsive particle-wall interaction. On the other hand, as discussed in the analysis of moderate Re_p by Koch [96], the particle migrates away from the wake of another particle. It would thus be reasonable to assume that the depletion regime of the steady state distribution $P(x)$ presents a situation where the particles interact with the wall and the other particles with equal strength. Furthermore, with moderate Re_p a particle induces an r^{-1} flow only to its wake whose width is proportional to the square root of the distance from the particle center, suggesting that $\zeta_x \sim \Phi^{-1/2}$. Although a systematic study of the effect of Re_p is beyond the scope of this work, we did additional studies with $\mathrm{Re}_p \neq 0.5$ and

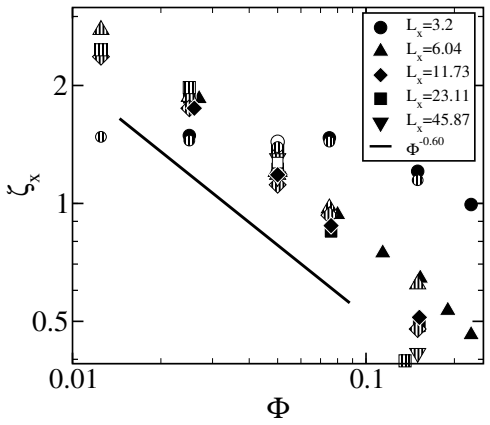

Figure 5.16: The width of the depletion layer as function of the volume fraction Φ. The data for $L_{\text{periodic}} = 22.76, 45.51$, and 91.02 are presented using solid, striped and open symbols, respectively. The solid line presents $\zeta_x \sim \Phi^{-0.60}$. Note that in the quasi-2D limit, ζ_x is almost independent of Φ since the particles are concentrated in the middle of the system. Error bars in this and the following figures are smaller or equal to the size of the symbols when not explicitly shown.

found that $f(x)$, and ζ_x strongly depend on Re_p. For example in the case of $L_{\text{periodic}} = 45.511$, $L_x = 6.044$, and $\Phi = 0.05$ we found that ζ_x increases from 0.95 to 1.43 when Re_p changes from 0.1 to 1.

5.2.2 Average sedimentation velocity

Due to the large depletion layer in low Φ systems it is reasonable to expect enhanced intrinsic convection: it can be assumed that the back flow is partly channeled to the depletion layer and the total volume flow in the particle rich central area is non-zero and pointing downward.

The intrinsic convection is visible in the quantity

$$V(x) = \langle \sum_{i=1}^{N} v_z^i \delta(x - x^i) \rangle / \langle \sum_{i=1}^{N} \delta(x - x^i) \rangle, \tag{5.8}$$

shown in Fig. 5.17 for the same two system widths and volume fractions as in Fig. 5.15. Like in the intrinsic convection found in a $\text{Re}_p = 0$ system [58, 25] the velocity profile follows closely the parabola in the central region of the

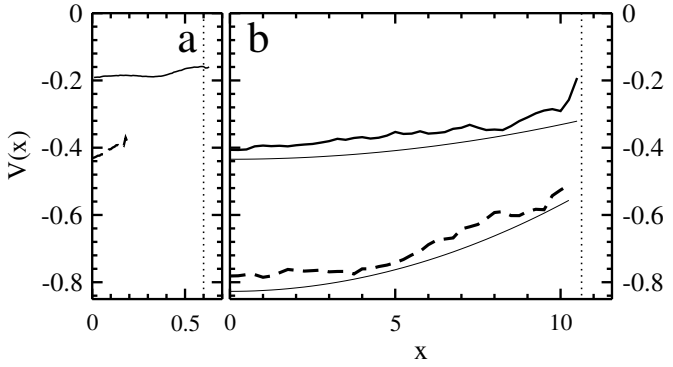

Figure 5.17: Average particle settling velocity as function of the x coordinate measured from the middle of the system: (a) wall spacing $L_x = 3.2$, $\Phi = 0.025$ (dashed line), $\Phi = 0.225$ (solid line). (b) $L_x = 23.11$, $\Phi = 0.025$ (dashed line), $\Phi = 0.152$ (solid line). The vertical dotted line marks the distance of one particle radius away from the wall. The two thin solid lines in (b) are parabolic fits to the data (shifted for clarity).

system with $L_x = 23.11$. The amplitude of the convection is, however, larger and increases significantly with the decreasing Φ.

In Fig. 5.18 we show the normalized average sedimentation velocity $\langle v_z \rangle$ averaged over x for different values of L_x. The first data points at $\Phi = 0$ correspond to the size-dependent one-particle velocity V_0 measured when the particle sediments in the middle of the system. The data are well approximated by the expression

$$V_0 \approx [1 - 0.502(a/L_x) + 0.0523(a/L_x)^3 + \\ + 0.0131(a/L_x)^4 - 0.005(a/L_x)^5]V_s, \tag{5.9}$$

which has been derived for a sphere in the middle of a system between two parallel, infinite walls, with $\mathrm{Re}_p = 0$ [68]. Our values are consistently slightly less than those predicted by Eq. (5.9) due to the finite Re_p effects [68] and the periodic boundaries in the y and the z directions [69]. As expected, with all the values of L_x here the average settling velocity is a monotonically decreasing function of the volume fraction Φ. All the data can be well fitted with the RZ law, but the exponent of the power law n depends on L_x. In the widest (3D) geometry the exponent is found to be 5.5 in good agreement with 3D experiments [131]. On the other hand, for the most narrow case where particle blocking is in effect, $n = 3.5$ which indicates a considerably slower decay in accordance with the previous studies [155].

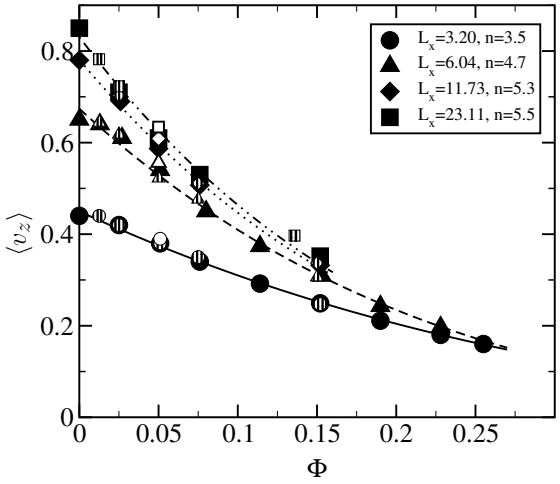

Figure 5.18: The normalized average settling velocity $\langle v_z \rangle$ for different wall spacings L_x. The lines are fits to the data. The data for $L_{\text{periodic}} = 22.76, 45.51$, and 91.02 are presented using solid, striped and open symbols, respectively.

However, our results show that since in Fig. 5.18 the normalization factor V_s is that of an infinite 3D system, the effect of the wall spacing rapidly decreases as a function of Φ, and even for the quasi-2D case it becomes negligible beyond $\Phi \approx 0.2$. An intuitive explanation is that with larger Φ a smaller portion of the particles interact with the walls. Another observation is that in dilute limit the increase of Φ does not reduce the average sedimentation velocity as fast that the RZ law predicts. This can be explained by the fact that the enhanced intrinsic convection reduces the effect of backflow. With increasing volume fraction ζ_x , however, decreases and with larger Φ the RZ law describes the sedimentation velocity accurately.

5.2.3 Velocity Fluctuations

Unlike the average settling velocity, the behavior of the velocity fluctuations is expected to be much more sensitive to changes in the size of the container, due to the dependence of the spatial correlation length of the velocities. Before discussing the velocity fluctuations we study the spatial velocity

correlation function (SVC) of the particles defined as

$$R_{\alpha\beta}(r) = \frac{\langle v_\alpha^i v_\alpha^j \rangle_\beta(r) - \langle v_\alpha^i \rangle_\beta^2(r)}{\langle (v_\alpha^i)^2 \rangle_\beta(r) - \langle v_\alpha^i \rangle_\beta^2(r)}, \tag{5.10}$$

where α and β can denote any of the spatial directions x, y, or z while v_α^i and v_α^j denote the α component of the velocity of particles i and j. With $\langle\cdot\rangle_\beta(r)$ we denote a steady state average over all pairs whose orientation differs less than 5 degrees from the direction of β and have a spatial distance of r. Studying the correlation lengths of $R_{\alpha\beta}(r)$ reveals a complicated interplay of different dimensions of the simulation box with, excluding R_{zz}, no Φ dependence. Most of the time they are in a good agreement with the experiments of Bernard-Michel *et al.* [15], performed in a long tube with a small square cross section.

In all directions our measured $R_{x\beta}(r)$ depends only on L_x provided that $L_x < L_{\text{periodic}}$. The correlation lengths are, however, different in each direction being smallest in the z direction, and largest in the y direction. For the y component of the particle velocities all correlation lengths increase seemingly linearly with increasing L_{periodic}.

The correlation lengths of $R_{zx}(r)$ and $R_{zy}(r)$ seem to depend both on L_x and L_{periodic} even when the former is much smaller than the latter. This time simulations performed with $L_y \neq L_z$ indicate that the correlation lengths depend on L_y even if $L_y < L_z$. The scaling of $R_{zz}(r)$, however, differs significantly from the previous by the fact that the correlation length depends also on Φ. With increasing Φ the correlation length decreases systematically in all cases studied, except in the system with $L_x \leq 6.044$ and $L_{\text{periodic}} = 22.76$ where the correlation length depends on the volume fraction only if $\Phi \geq 0.08$. This result can be understood as a direct consequence of the depletion region above the test particle and is thus a finite Re_p phenomenon.

We will now turn our attention to the velocity fluctuations. Their qualitative behavior as a function of the volume fraction Φ is the same in all directions and with all values of L_x, except in the quasi-2D limit in the x direction. Namely, the fluctuations increase initially with Φ due to the increasing effective particle interactions, but for larger values of Φ mutual blocking effects render $\sigma(v)$ a decreasing function of Φ as seen in numerous previous experiments [172, 157].

In y direction we could not found a clear scaling but in other directions the scaling is quite clear as will be seen in Fig. 5.19 where we present the

velocity fluctuations in the z and x directions, respectively. In both figures we have presented the data obtained by using different L_{periodic} and three different lengths in the periodic dimensions: 22.76, 45.51, 91.02, presented by solid, striped and open symbols, respectively.

In the direction parallel to gravity the size of the velocity fluctuations depends strongly on L_x and only weakly on the other dimensions, especially when the container aspect ratio L_x/L_{periodic} is small. The finite-size scaling follows $\sigma(v_z) \sim L_x^{1/3}$ with good accuracy, except in the quasi-2D limit, as shown in the inset of Fig. 5.19 (a). This is in an apparent contradiction with the prediction of Caflisch and Luke [28] that $\sigma(v_z) \sim L^{1/2}$. When comparing the pairs of systems with approximately the same L_x/L_{periodic}, the increase of velocity fluctuations with the increasing container size does not contradict the prediction of Caflisch and Luke [28] provided that $L_x/L_{\text{periodic}} > 1/8$.

In order to find out the Φ and L_x scaling of $\sigma(v_z)$, it is necessary to normalize the velocity fluctuations with $\langle v_z \rangle$ rather than V_s [156, 15]. In the main plot of Fig. 5.19(a) we show $\sigma(v_z)/\langle v_z \rangle \sim L_x^{1/3}$. We find that in dilute systems, these fluctuations obey a power law $\sigma(v_z)/\langle v_z \rangle \sim \Phi^{\xi}$, with $\xi = 0.41 \pm 0.01$ instead of $\xi = 1/2$ as predicted by Caflisch and Luke [28].

Quite similar to the fluctuations in the direction of gravity, $\sigma(v_x)$ does not scale at all with the periodic dimensions, provided that L_x is smaller than the other dimensions. Such a result is reasonable since the correlation length of the x component of the particle velocities depends only on L_x. The scaling with the wall spacing is, however, somewhat different. Instead of L_x scaling, we find that $\sigma(v_x)/\langle v_z \rangle$ scales reasonably well with L_x^{eff}. In Fig. 5.19 (b), in which normalization with $\langle v_z \rangle$ rather than with V_s was used, we show that $\sigma(v_x)/\langle v_z \rangle/(L_x^{\mathit{eff}})^{1/2}$ scales as Φ^{ξ} with $\xi = 0.47 \pm 0.03$. Since the scaling exponent of Φ and L_x^{eff} is essentially the same this can be interpreted as $L_x^{1/2}(\Phi^{\mathit{eff}})^{1/2}$, where $\Phi^{\mathit{eff}} = \Phi L_x^{\mathit{eff}}/L_x$ is the average volume fraction in the volume occupied by the particles. Again, by only considering containers with approximately the same aspect ratio we note that with fixed L_x/L_{periodic} the scaling of $\sigma(v_x)$ does not contradict the predictions of Caflisch and Luke [28] provided that $L_x/L_{\text{periodic}} > 1/4$.

As mentioned before, the behavior of $\sigma(v_y)$ in the periodic y direction is less clear. We were not able to find any clear scaling law. It seems, however, that in a dilute suspension the wall spacing limits the velocity fluctuations only if $L_x/L_{\text{periodic}} \lesssim 1/4$. At this point $\sigma(v_y)$ has values of the same order as $\sigma(v_x)$ in a container with equal dimensions and any further increase of

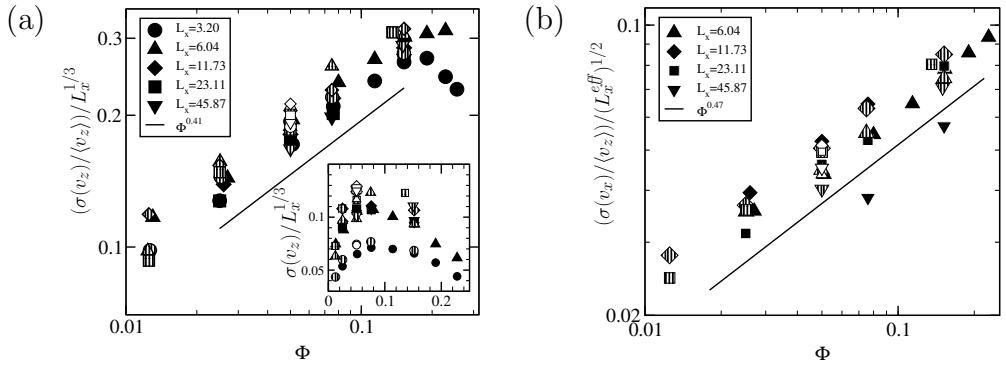

Figure 5.19: (a) Velocity fluctuations in the direction of gravity with different system sizes, normalized by $(1/L_x)^{1/3}$. The solid line corresponds to a power law with exponent 0.41. The solid, striped and open symbols denote $L_{\text{periodic}} = 22.76$, 45.51, and 91.02, respectively. (b) Velocity fluctuations in the x direction perpendicular to the walls, scaled by $\sqrt{L_x^{eff}}$. The solid line corresponds power law with exponent 0.47.

L_x does not affect these values significantly. In a more dense suspension with $\Phi = 0.15$ there is a systematic increase of $\sigma(v_x)$ with increasing L_x.

5.3 Sedimentation of Spheroidal Particles

To expand the study of sedimentation beyond simple spherical particles, a convenient choice is to use spheroidal shapes. The benefits of this choice are that the dynamics of a single sedimenting spheroid is well-known, the shape has a high degree of symmetry, and spherical particles can be considered as a limiting case. Spheroid can be used as a mathematical idealization of both a fiber-like and plate-like bodies. Both are common in nature and exist in many materials.

We have studied the dynamics of the steady state suspension of spheroids using again the marker technique described in section 4.4. A certain spheroidal shape can be described by single additional parameter, the aspect ratio a_r. Considering the motion of an isolated spheroid, it is also important to know the angle θ between its axis of revolution and direction of gravity. Before discussing the sedimentation of suspension with finite Φ we will briefly comment the dynamics of a single spheroidal particle.

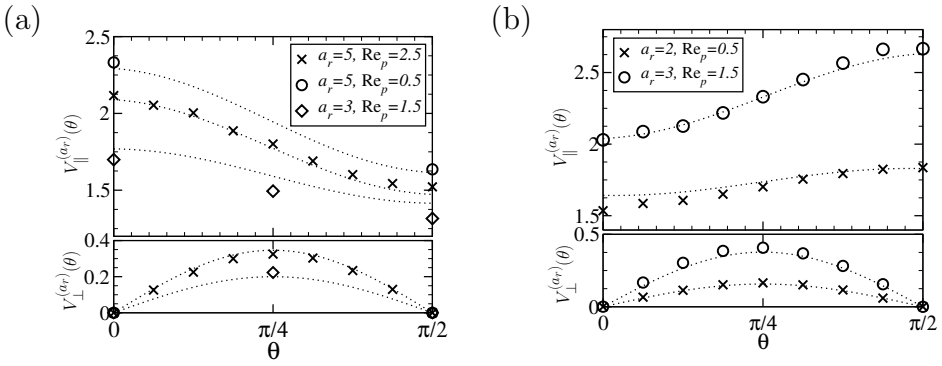

Figure 5.20: Some measured single prolate (a) and oblate (b) spheroid velocities as a function of θ in a periodic container with dimensions $32 \times 32 \times 64$. The velocity component parallel to gravity are shown in the upper subplot and the perpendicular component in the lower. The lines correspond to the theoretical values. Corrections from finite size and Re_p are made for the parallel velocities.

Some measured velocities of prolate spheroids with different a_r and Re_p are shown in Fig. 5.20 (a). The orientation of the spheroid has been fixed in these simulations since otherwise the spheroid tends to turn perpendicular to gravity, as expected according to the results of Galdi and Vaidya [57]. To compare the results to the theoretical predictions we have used the low Re_p limit results presented in Eqs. (2.24) and (2.25) (for prolate spheroid) and Eqs. (2.26) and (2.27) (for prolate spheroid) with a finite Re_p and size corrections. The corrections have been calculated separately and only to the cases with $\theta = 0$ and $\pi/2$ while the off-diagonal corrections are obtained by assuming the functional form of Eqs. (2.24) and (2.26) does not change. The effect from finite Re_p is corrected by using the results of Breach [22] and as a finite size correction we used Hashimoto's result for a periodic array of spheres with matched hydrodynamic radius [69]. The corresponding results for oblate spheroids are shown in Fig. 5.20 (b). The theoretical predictions are shown in Fig. 5.20 with dotted lines. The corrections are made only to the parallel velocity component. The quantitative agreement is excellent and we will now on assume that the single spheroid velocites obtained through simulation have the same angular dependence as in Eqs. (2.24) and (2.26).

We will now proceed to study the case of many spheroids. We will dis-

cuss first the average sedimentation velocity and try to understand its Φ dependence, based on our observations about orientational distribution and spatial density fluctuations. Next we will discuss the reasons behind the transition in the orientation distribution and then we consider the formation of the observed density fluctuations. We will end the section with results concerning oblate spheroids.

5.3.1 The Average Sedimentation Velocity

To measure $\langle v_\parallel \rangle$ we studied spheroids with $a_r = 3$, 5, and 7, keeping the smaller radius fixed. The density of the particles is 2.5 times the fluid density. The system sizes used in this work are $32 \times 32 \times 64$ in units of the smaller radius of the particles, where the larger dimension is in the direction of gravity. Periodic boundary conditions in all directions were used to obtain the steady state which was checked from $\langle v_\parallel \rangle$ and its fluctuations. In our simulations, we have fixed the fluid viscosity so that the particle Reynolds number $\mathrm{Re}_p \approx 0.5 a_r$.

In Fig. 5.21 we show the mean settling velocities for $a_r = 1, 3, 5$, and 7, where we have normalized the velocities by the measured $V_\parallel^{(a_r)}$. At higher volume fractions, all data follow the RZ law rather closely, while at smaller Φ the velocity for spheres decreases faster than predicted by the RZ law, as discussed in subsection 5.1.1. However, the spheroidal particles show *non-monotonic* dependence on Φ, with a clear maximum for each case where $a_r > 1$. Moreover, for the case $a_r = 3$, the maximum at $\Phi_m \approx 0.01$ is larger than $V_\parallel^{(3)}$. The maximum seems to decrease with increasing a_r, and its position moves to slightly higher values of Φ. Maximum of $\langle v_\parallel \rangle$ at finite Φ is exactly what could be expected according to the previous experiments and simulations [73, 27].

In order to consider the potential causes for this non-monotonic behavior we examine how Eq. (3.9) would change if it were generalized to the case of a spheroidal suspension. First, in order to take account that the terminal velocity is a function of θ we have to replace V_s by $\int P(\cos\theta) V_\parallel^{(a_r)}(\theta) d(\cos\theta)$. Here $P(\cos\theta)$ is the orientational distribution. Second, the assumptions made for $g(\mathbf{r})$ might not hold for the spheroidal suspension. According to this simple consideration, if $P(\cos\theta)$ or $g(\mathbf{r})$ depend on Φ this could lead to results differing from the sedimentation of spheres.

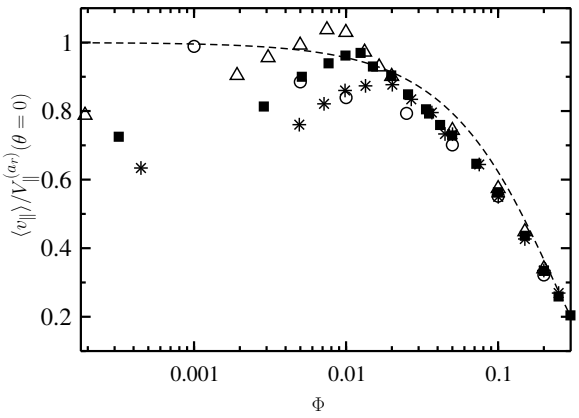

Figure 5.21: The normalized average settling velocity as a function of Φ for aspect ratios $a_r = 1$ ($\bigcirc$), 3 ($\triangle$), 5 ($\blacksquare$), and 7 ($*$). The dashed curve shows the RZ law $(1-\Phi)^{4.5}$. The errors are about the size of the symbols. The first points in the spheroid data correspond to the case of single spheroids.

In Fig. 5.22 (a) we show $P(\cos\theta)$ for various volume fractions for the case $a_r = 5$. In the dilute limit, it can be seen that spheroids prefer the *perpendicular* alignment around $\cos\theta = 0$, in agreement with the theoretical and experimental results for a single prolate spheroid with $\mathrm{Re}_p > 0$. However, when the volume fraction increases the spheroids begin to orient themselves parallel to gravity. It can be seen from the data that the maximum in $\langle v_\parallel \rangle$ occurs around the value of Φ where the distribution function $P(\cos\theta)$ flattens out. To examine the influence of the change in the orientation of *single* spheroids on $V(\Phi)$, we have normalized $\langle v_\parallel \rangle$ by $\int P(\cos\theta) V_\parallel^{(a_r)}(\theta) d(\cos\theta)$. This should cancel out pure single-particle orientational effects. With this normalization the non-monotonic behavior of the settling velocity still remains and the maximum is about 40% higher than for spheres. Also, the data for different a_r scale so that the locations and heights of the maxima at Φ_m are almost identical (see Fig 5.22 (b)).

We will next study the pair correlation function $g(r,\theta) = 2N^{-2}\langle \sum_{i\neq j} \delta(\mathbf{r} - (\mathbf{r^i} - \mathbf{r^j}))\rangle$, where $\mathbf{r^i}$ is the position of the i^{th} particle and θ is the angle between $\mathbf{r}$ and the direction of gravity. The summation is carried out over all the particle pairs. The reason to study the θ dependence of $g(r,\theta)$ is that according to Eq. (3.9) it has significant effect to the average sedimentation velocity and Batchelor's results were obtained by assuming that g does not have any θ dependence [10]. In Figs. 5.23 and 5.24 we show $g(r,\theta)$ for $\Phi = 0.01$ and $\Phi = 0.02$, respectively, calculated from the data obtained

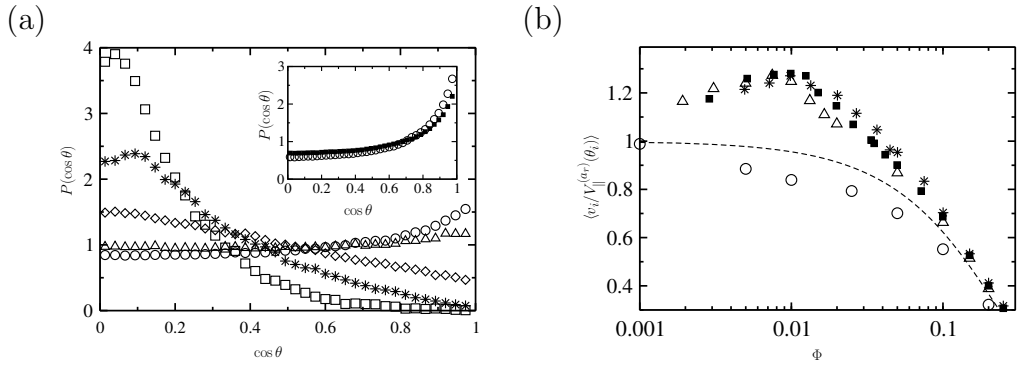

Figure 5.22: (a) The distribution function $P(\cos\theta)$ for spheroids with $a_r = 5$. In the main figure we show data for volume fractions 0.0029 (□), 0.005 (∗), 0.0099 (◇), 0.019 (△), and 0.034 (◯), and in the inset for 0.10 (■), and 0.20 (◯) (b) The scaled average settling velocity as a function of Φ for aspect ratios $a_r = 1$ (◯), 3 (△), 5 (■), and 7 (∗). The data are scaled by $\langle v_\parallel\rangle / \int P(\cos\theta) V_\parallel^{(a_r)}(\theta) d(\cos\theta)$ The dashed curve shows the RZ law $(1-\Phi)^{4.5}$. The errors are about the size of the symbols. The first points in the spheroid data correspond to the case of single spheroids.

from simulations of $a_r = 3$ spheroids in a system with size $64 \times 64 \times 128$. In the case with $\Phi = 0.01$ (and in all values of Φ below that) we can clearly see that there is enhanced particle density below and above the test particle. By inspecting the sedimentation visually we saw that the particles were forming streams. The excess of other particles in directly below the test particle is increasing its downward sedimentation velocity since the velocity disturbance created by the other particles is pointing downward. The pair correlation function is thus providing a qualitative explanation for the large average sedimentation velocities in a dilute suspension. There is, however, a clear change in the qualitative behavior of $g(r, \theta)$ as Φ is increased. In $\Phi = 0.02$ the streaming is not visible any more and also $g(r, \theta)$ has changed drastically. This is in a good agreement with the fact that with large Φ the average sedimentation velocity of spheroids does not differ qualitatively from the average velocity of sedimenting spherical particles.

To investigate this change more quantitavely we integrate $ng(r)$ over the area where $g(r) - 1$ is positive. With n we denote the particle number density. The integral gives a measure on the average number of excess additional particles, N_{ex}, around the reference particle. This integral also

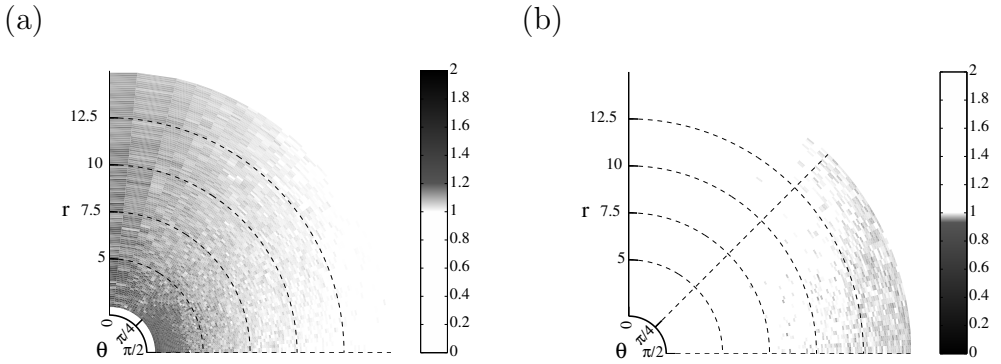

Figure 5.23: The pair correlation function $g(r, \theta)$ of spheroids with $a_r = 3$ in suspension of $\Phi = 0.01$. The size of the system is $64 \times 64 \times 128$. The areas with density higher and lower than the average are shown in (a) and (b), respectively.

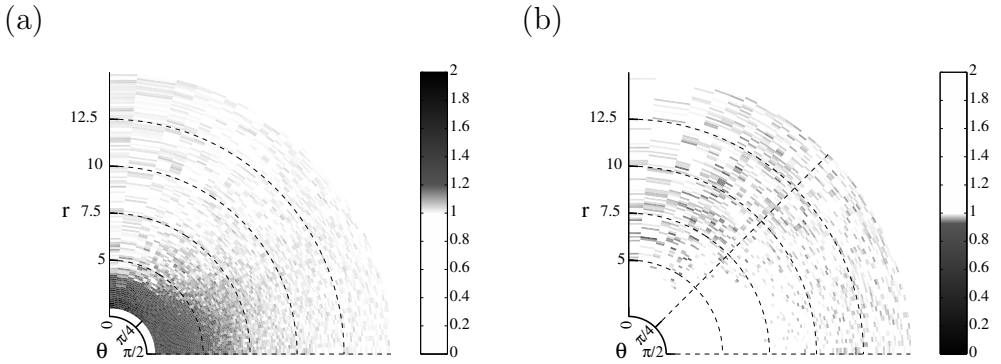

Figure 5.24: The pair correlation function $g(r, \theta)$ of spheroids with $a_r = 3$ in suspension of $\Phi = 0.02$. The size of the system is $64 \times 64 \times 128$. The areas with density higher and lower than the average are shown in (a) and (b), respectively.

measures subsystem density fluctuations through the sum rule [62]. For spheres we find that N_{ex} is almost zero for $\Phi \lesssim 0.1$ and slowly increases with Φ as included by the dotted line in Fig. 5.25. In contrast, for spheroids the density fluctuations have a clear *maximum* which coincides with the maximum of $\langle v_{\parallel} \rangle$ (see Fig. 5.25). The measured N_{ex} also supports the observations [73, 27] that in fiber suspension the density inhomogeneities

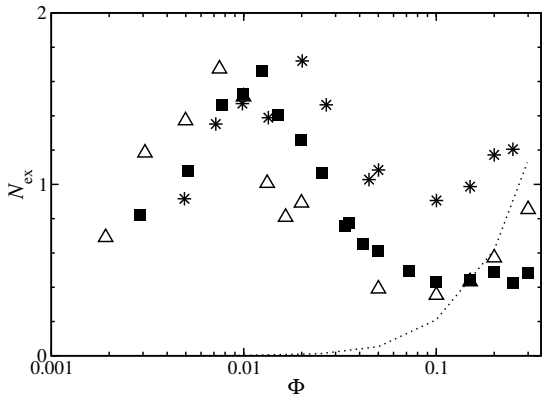

Figure 5.25: The excess particle number $N_{\rm ex}$ around the reference particle with aspect ratios 3 (△), 5 (■), and 7 (∗). The dotted line corresponds the results from spherical particles.

are enhanced and g has significant deviation from $g_{\rm eq}$.

5.3.2 Orientational Transition

In order to study the change in the orientational distribution we define an "order parameter" $\Psi = \langle 2\cos\theta - 1\rangle$, which would have values -1, 0, and $+1$ if all the spheroids in the system were perpendicular to gravity, randomly oriented, or parallel to gravity, respectively. In Fig. 5.26 (a) we show how Ψ depends on Φ. In the dilute regime Ψ increases strongly, while for approximately $\Phi > 0.01 - 0.02$, Ψ changes more slowly. The values of $\Phi_{\rm cr}$ where $\Psi \approx 0$ correspond roughly to where the settling velocity has a maximum. The two regimes are more clear in the "susceptibility" $\chi = [\langle\Psi^2\rangle - \langle\Psi\rangle^2]$ (see Fig. 5.26 (a)).

This indicates the existence of a *non-equilibrium orientational transition*, which can be understood by considering the torques acting to a single spheroid sedimenting in a shear flow. Assuming that we can separate $\tau^{\rm h}$ induced by the shear rate $\dot\gamma$ (given by Eq. (2.23)), and the inertial $\tau^{\rm GV}$ (given by Eq. (2.40)), the spheroid would obtain a certain orientation when the two torques cancels each other. This is demonstrated in Fig. 5.27 where the θ dependence of $\tau^{\rm h}$ and $-\tau^{\rm GV}$ are shown for spheroid with $a_r = 5$. The positive direction of $\tau^{\rm h}$ has been chosen so that it acts to turn the spheroid away from the perpendicular orientation. Since the strength of $\tau^{\rm h}$ is proportional to $\dot\gamma$ it is clear that once the shear rate is large enough, $\tau^{\rm GV}$ cannot

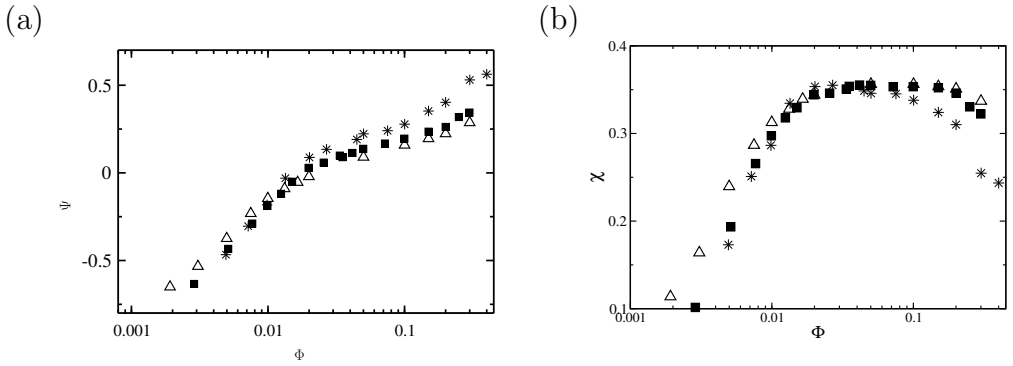

Figure 5.26: (a) The order parameter $\psi = \langle 2\cos\theta - 1 \rangle$ as a function of the volume fraction Φ with aspect ratios 3 ($\triangle$), 5 ($\blacksquare$) and 7 ($*$). (b) The susceptibility χ from the same data.

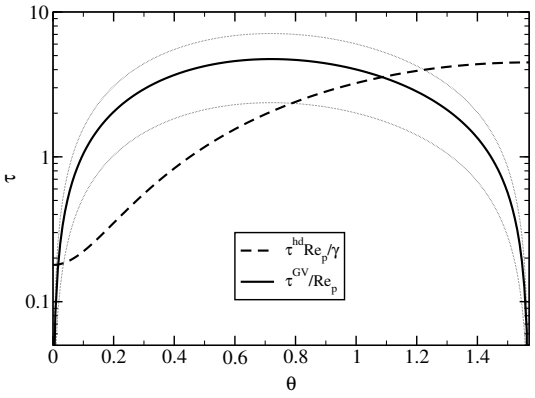

Figure 5.27: The θ dependence of the numerical coefficients in the hydrodynamic torque τ^{h} and the inertial torque τ^{GV}. The thin dotted line corresponds the numerical coefficients of $0.5\tau^{\mathrm{GV}}$ and $1.5\tau^{\mathrm{GV}}$ (see text for details).

cancel it at any θ and the spheroid starts to rotate. Bellow that there is a certain $\dot{\gamma}$ dependent angle where the torques cancels.

Returning to the sedimentation we can assume that a test particle is feeling a shear flow either by being in the wake of other particles or due to the convection created by large scale density fluctuations. At first approximation the former creates a shear rate $\dot{\gamma} \propto r^{-2}$ and the latter $\sigma(v_{\|})/L$ where L is the linear size of the container. Both increase with increasing Φ since the average inter-particle distance decreases and the velocity fluctuations

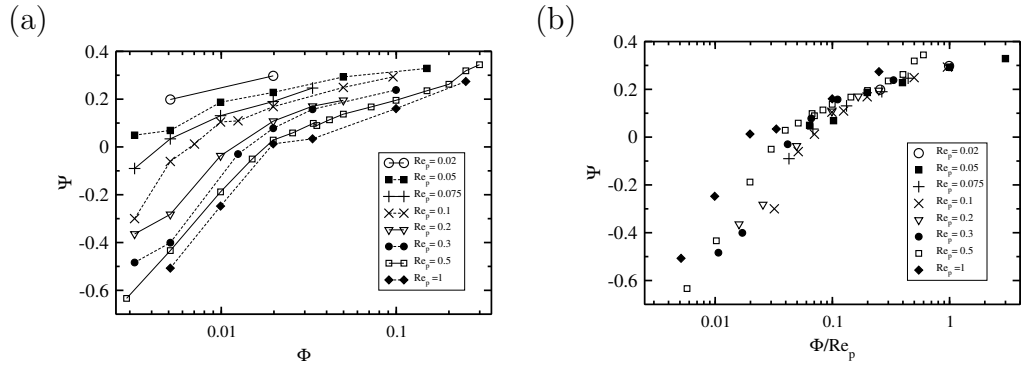

Figure 5.28: (a) The orientational order parameter Ψ as a function of volume fraction Φ with different Re_p. (b) The orientational order parameter Ψ with different Re_p represented as a function of the volume fraction divided by Re_p.

increase. Thus at some value of Φ the typical shear rate experienced by the spheroid increses enough that τ^{h} dominates τ^{GV} and the orientational trajectories resembles the Jeffery orbitals. By assuming that the rotating spheroids have angular velocity qualitatively similar to the Jeffery orbitals we will obtain $P(\cos\theta)$ similar to that observed with large Φ.

Since $\tau^{\mathrm{h}}/\tau^{\mathrm{GV}}$ scales as $\dot{\gamma}\mathrm{Re}_p^{-2}$ it would be reasonable to assume that Φ_{cr} where the transition occurs depends on Re_p. In Fig. 5.28 (a) we show $\Psi(\Phi)$ for spheroids with $a_r = 5$ using several different Re_p. There is a systematic change in the plots with Ψ increasing with increasing Re_p when Φ is kept constant. We note that Ψ represented as a function of the ratio Φ/Re_p has rather universal behavior in the regime of slower growth, which is evident in Fig. 5.28 (b). A quantitative explanation of the scaling would require a more detailed study of the scaling of the average $\dot{\gamma}$.

5.3.3 Density Fluctuations

We will end the discussion of the sedimentation of prolate spheroids by trying to give a plausible explanation for the enhanced density fluctuations occuring in the low Φ sedimentation. Koch and Shaqfeh have shown that in the $\mathrm{Re}_p = 0$ limit the fibers tend to form clusters [94]. Here we restrict our study to the $\mathrm{Re}_p > 0$ case. Assume now that our test spheroid has been drifted to the wake of another particle with the axis of revolution pointing

towards the center of the wake. The shear flow produced by the wake now tends to turn the spheroid away from its perpendicular orientation. Providing that the shear rate is not too high, τ^{GV} will cancel τ^{h} at certain angle θ'. But a spheroid sedimenting with $0 > \theta' > \pi/2$ has also a velocity component pointing toward the center of the wake. This kind of interaction would lead to the formation of long streams of particles as seen by visual inspection and in $g(r, \theta)$ shown in Fig. 5.23.

The stream formation mechanism described above would also give a hint why the streams disappear at around Φ_{cr}. Once the test particle is caught in a wake with local $\dot{\gamma}$ large enough it starts to rotate. Even though it is not clear how the rotating spheroid would behave in the wake of another particle, we can say that at least the simple explanation given above does not hold anymore. Instead, a lift force due to the rotation would emerge which points away from the wake center as in the case of spherical particles [96].

5.3.4 Oblate spheroids

We will complete the results about the spheroidal sedimentation by briefy considering the issue of oblate spheroids. Even though the shape of an oblate spheroid differs from a prolate one, its coupling to the fluid is very similar. There is one notable difference: qualitatively its orientational behavior should be opposite to the one obtained in the sedimentation of prolate spheroids. Thus the inertial torque τ^{GV} tends to turn single settling oblate spheroid parallel to gravity[3]. On the other hand, an oblate spheroid would spend most of the time perpendicular to the shear field if it is rotating without a torque.

If the streaming of prolate spheroids is formed by the mechanism described in the previous subsection it would be reasonable to assume that the streaming would even more drastic in the case of an oblate spheroid. It is thus not suprising that the average sedimentation velocity of oblate spheroids has qualitatively similar behavior as the prolate ones, as seen in Fig. 5.29 (a). Most notable difference is that the maxima of $\langle v_{\parallel} \rangle$ are larger than in the case of prolate spheroids. The transition in the orientational behavior is happening now in the different direction as shown in Fig. 5.29 (b). Now it is, however, impossible to distinguish between the two different regimes.

[3]Note that the orientation is still measured as the angle between the direction of gravity and the axis of revolution.

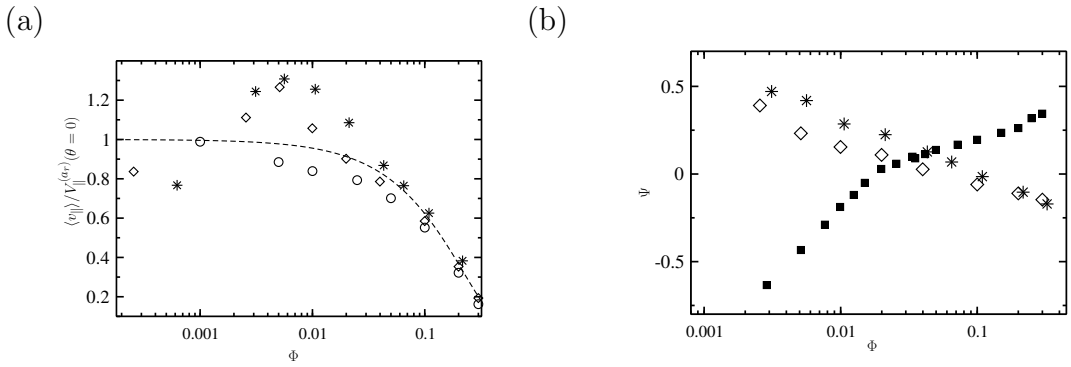

Figure 5.29: (a) The normalized average settling velocity as a function of Φ for oblate spheroids with aspect ratios $a_r = 1$ ($\bigcirc$), 2 ($\Diamond$), and 3 ($*$). The dashed curve shows the RZ law $(1-\Phi)^{4.5}$. The errors are about the size of the symbols. The first points in the spheroid data correspond to the case of single spheroids. (b) The order parameter $\Psi = \langle 2\cos\theta - 1\rangle$ as a function of the volume fraction Φ for oblate spheroids with aspect ratio 2 ($\Diamond$), 3 ($*$). The data for prolate spheroids with $a_r = 5$ ($\blacksquare$) are show for reference.

Chapter 6

Summary and Conclusions

In this work we have studied the mono-disperse sedimentation with such parameters that the Péclet number is infinite and the particle Reynolds number has been chosen so that the flow in particle scales is laminar but that the corresponding container size dependent Reynolds number is large compared to unity.

The chosen parameters make it possible to model the fluid as a continuum and the particles as rigid objects. The main challenge to produce the numerical simulations, based on this description, is related to the complex time-dependent boundary conditions between the fluid and the solid bodies. Here we have introduced an immersed boundary kind of computational method that is capable to simulate arbitrary shaped particles under finite Re_p conditions and have implemented it to the case of spheroidal particles.

We chose to study aspects about sedimentation that have not been previously explained in detail even in the zero Reynolds number limit, such as the non-Gaussian nature of the velocity fluctuations, the memory effects in particle trajectories, the effect of container walls, and the sedimentation of spheroidal particles.

We have focused to the statistical properties of the particles under steady state sedimentation such as the velocity distribution and the pair distribution. Even though in most cases we have not studied systematically the effect of Reynolds number we have seen that one consequence of the finite particle Reynolds number is that the steady state particle distributions differ significantly from the equilibrium distributions. This discrepancy can

be explained by the lift force and other forces whose origin lie in inertial effects.

The non-Gaussian velocity distribution of sedimenting spheres can be understood by the findings that part of the velocity differences can be explained by variations in the local volume fraction, and that the variance of the unexplained part depends also on the local density. The role of the finite Reynolds number to the distribution of the local volume fractions remains, however, unclear and it would require a systematic study of different Re to find it out. Instead it is clear that the observed pair distribution function has an effect to the average sedimentation velocity.

The studies in a confined geometry revealed that the intrinsic convection is enhanced in the finite Re sedimentation due to depletion regions close to the container walls. The average sedimentation velocity was also found to depend on the distance between the walls. Changing the size of the system revealed a complicated connection between system size and the velocity fluctuations. Again, systematic studies with varying Re would be required to found out how the intrinsic convection depends on the inertial effects.

Unlike in the suspension of spherical particles, the average sedimentation velocity of elongated bodies is not a monotonically decreasing function of the volume fraction. Instead, previous experiments and simulations done in low Re_p limit have shown that the average velocity has a maximum at certain Φ. Our simulations show that the same is true also in the sedimentation of prolate spheroids with finite Re_p and the non-monotonic behavior can be connected to the observed changes in pair distribution and orientational preferences.

The preferred orientation changes from perpendicular to parallel to gravity as the volume fraction is increased, and the critical value of the volume fraction Φ_{cr} where this occurs decreases with decreasing Re_p. This can be explained by considering the relative importance of torques from different origin affecting the sedimenting spheroid. At around the same volume fraction where the orientational transition occurs the pair distribution function also undergoes a transition from a situation, where there is excess probability to find other particles above or below the test particle, to the case where the corresponding probability is reduced below the average. Our preliminary results on the oblate spheroids indicate that such a suspension would have the same characteristics as prolate spheroids.

Even though the observed Re_p scaling of Φ_{cr} can be understood qualitatively,

a more quantitative understanding would require further studies. Also the effects from the finite size are not studied in detail, even though it is reasonable to assume that they play some role since the region of non-uniform $g(\mathbf{r})$ is of the order of the system size.

The aspect ratio of the sedimenting spheroids also has an effect. The data suggest that reducing the aspect ratio further would not reproduce smoothly the behavior characteristic to a suspension of spherical particles. Rather, the average sedimentation velocity for a spheroid with a_r close to unity might have an abrupt change from spheroidal behavior (with $\Phi < \Phi_{\mathrm{cr}}$) to spherical behavior (with $\Phi > \Phi_{\mathrm{cr}}$). Furthermore, since any of the mechanisms would require that the particles were uniform, it is possible that studying the sedimentation of almost spherical particles with polydispersity in shape rather than size would also reveal a non-monotonic behavior in the average sedimentation velocity.

As a final remark we would like to note that all the results reported here are obtained under steady state conditions. Before the steady state was reached the system had several stages of evolution which could together take much longer than what it takes for a single particle to fall the length of the system. It would require further studies to give a systematic description of such different stages, too.

Bibliography

[1] T. Ala-Nissila, R. Ferrando, and S. C. Ying, Adv. Phys. **51**, 949 (2002).

[2] T. Ala-Nissila, S. Majaniemi, and K. Elder, in *Novel Methods in Soft Matter Simulations*, Lecture Notes in Physics **640** edited by M. Karttunen, I. Vattulainen, and A. Lukkarinen, (Springer-Verlag, Berlin Heidelberg, 2004).

[3] M. P. Allen and D. J. Tildesley, *Computer Simulation of Liquids* (Clarendon, Oxford, 1987).

[4] T. Allen, *Particle Size Measurement,* 4th edition (Chapmann and Hall, London, 1990).

[5] J. B. Avalos and A. D. Mackie, J. Chem. Phys. **111**, 5267 (1999).

[6] R. C. Ball and J. R. Melrose, Physica A **247**, 444 (1997).

[7] A. J. Banchio and J. F. Brady, J. Chem. Phys. **118**, 10323 (2003).

[8] R. Barnea and J. Mizrahi, Chem. Eng. J. **5**, 171 (1973).

[9] G. K. Batchelor, J. Fluid Mech. **44**, 419 (1970).

[10] G. K. Batchelor, J. Fluid Mech. **52**, 245 (1972).

[11] G. K. Batchelor, J. Flud Mech. **193**, 75 (1988).

[12] C. W. J. Beenakker and P. Mazur, Physica A **120**, 388 (1983).

[13] C. W. J. Beenakker and P. Mazur, Phys. Fluids **28**, 3203 (1985).

[14] L. Bergougnoux, S. Ghicini, E. Guazzelli, and J. Hinch, Phys. Fluids **15**, 1875 (2003).

[15] G. Bernard-Michel, A. Monavon, D. Lhuillier, D. Abdo, and H. Simon, Phys. Fluids **14**, 2339 (2002).

[16] G. A. Bird, Phys. Fluids **13**, 2676 (1970).

[17] J. R. Blake, Proc. Camb. Phil. Soc. **70**, 303 (1971).

[18] E. S. Boek, P. V. Coveney, H. N. W. Lekkerkerker, and P. van der Schoot, Phys. Rev. E **55**, 3124 (1997).

[19] J. P. Boon and S. Yip, *Molecular Hydrodynamics* (Dover, New York, 1980).

[20] G. Bossis and J. F. Brady, J. Chem. Phys. **87**, 5437 (1987).

[21] J. F. Brady and G. Bossis, Ann. Rev. Fluid Mech. **20**, 111 (1988).

[22] D. R. Breach, J. Fluid Mech. **10**, 306 (1961).

[23] M. P. Brenner, Phys. Fluids. **11**, 754 (1999).

[24] D. Bruneau, F. Feuillebois, R. Anthore, and E. J. Hinch, Phys. Fluids **8**, 2236 (1996).

[25] D. Bruneau, F. Feuillebois, J. Bławzdziewicz, and R. Anthore, Phys. Fluids **10**, 55 (1998).

[26] B. Bunner and G. Tryggvason, J. Fluid Mech. **466**, 53 (2002).

[27] J. Butler and E. S. G. Shaqfeh, J. Fluid Mech.

[28] R. E. Caflisch and J. H. C. Luke, Phys. Fluids **28**, 759 (1985).

[29] C. S. Campbell, Ann. Rev. Fluid Mech. **22**, 57 (1990).

[30] H. Chen, S. Chen, and W. H. Matthaeus, Phys. Rev. A **45**, R5339 (1992).

[31] S. Chen and G. D. Doolen, Annu. Rev. Fluid Mech. **30**, 329 (1998).

[32] I. L Claeys and J. F. Brady, J. Fluid Mech. **251**, 411 (1993).

[33] I. L Claeys and J. F. Brady, J. Fluid Mech. **251**, 443 (1993).

[34] I. L Claeys and J. F. Brady, J. Fluid Mech. **251**, 479 (1993).

[35] R. Clift, J. R. Grace, and M. E. Weber, *Bubbles, Drops, and Particles* (Academic Press, New York, 1978).

[36] E. Climent and M. R. Maxey, Int. J. Multiphase Flow **29**, 579 (2003).

[37] M. L. Cowan, J. H. Page, and D. A. Weitz, Phys. Rev. Lett. **85**, 453 (2000).

[38] S. L. Dance, M. R. Maxey, Phys. Rev. E **68**, 031403 (2003).

[39] R. H. Davis and A. Acrivos, Ann. Rev. Fluid Mech. **17**, 91 (1985).

[40] G. G. de Kruif, E. M. F. van Iersel, A. Vrij, and W. B. Russel, J. Chem. Phys. **83**, 4717 (1985).

[41] S. Dong, D. Liu, M. R. Maxey, and G. E. Karniadakis, J. Comput. Phys. **195**, 695 (2004).

[42] P. Duru and E. Guazzelli, J. Fluid Mech. **470**, 359 (2002).

[43] A. Esmaeeli and G. Tryggvason, J. Fluid Mech. **377**, 313 (1998).

[44] P. Español, Phys. Rev. E **52**, 1734 (1995).

[45] P. Español, Europhys. Lett. **40**, 631 (1997).

[46] P. Español, Phys. Rev. E **67**, 026705 (2003).

[47] X.-J. Fan, N. Phan-Thien, and R. Zheng, Z. Angew. Math. Phys. **49**, 167 (1998).

[48] X.-J. Fan, N. Phan-Thien, and R. Zheng, J. Non-Newtonian Fluid Mech. **74**, 113 (1998).

[49] J. Feng, H. H. Hu, D. D. Joseph, J. Fluid Mech **261**, 95 (1994).

[50] Z. Feng and E. E. Michaelides. int. J. Multiphase Flow **28**, 479 (2002).

[51] J. H. Ferziger and M. Perić, *Computational Methods for Fluid Dynamics*, 3rd edition (Springer-Verlag, Berlin Heidelberg, 2002).

[52] E. G. Flekkøy, P. V. Coveney, and G. D. Fabritis, Phys. Rev. E **62**, 2140 (2000).

[53] A. L. Fogelson, and C. S. Peskin, J. Comput. Phys. **79**, 50 (1988).

[54] F. Fonseca and H. J. Herrmann, Physica A **343**, 447 (2004).

[55] F. Fonseca and H. J. Herrmann, Physica A **345**, 341 (2005).

[56] U. Frisch, B. Hassalacher, and Y. Pomeau, Phys. Rev. Lett. **56**, 1505 (1986).

[57] G. P. Galdi and A. Vaidya, J. Math. Fluid Mech. **3**, 183 (2001).

[58] U. Geigenmüller and P. Mazur, J. Stat. Phys. **53**, 137 (1988).

[59] D. Gidaspow, *Multiphase flow and Fluidization* (Academic Press, London, 1994).

[60] R. Glowinski, T. W. Pan, T. I. Hesla, and D. D. Joseph, Int. J. Multiphase Flow **25**, 755 (1999).

[61] R. Glowinski, T. W. Pan, T. I. Hesla, D. D. Joseph, and J. Périaux, J. Comput. Phys. **169**, 363 (2001).

[62] N. Goldenfeld, *Lectures on Phase Transitions and the Renormalization Group* (Addison-Wesley, Reading, 1992)

[63] R. Gomer, Rep. Prog. PHys. **53**, 917 (1990).

[64] R. D. Groot and P. B. Warren, J. Chem. Phys. **107**, 4423 (1997).

[65] W. Hackbusch, *Multi-Grid Methods and Applications* (Springer, Heidelberg, 1985).

[66] J. M. Ham, S. Thomas, E. Guazzelli, G. M. Homsy, and M.-C. Anselmet, Int. J. Multiphase Flow **16**, 171 (1990).

[67] J. P. Hansen and I. R. McDonald, *Theory of simple liquids* (Academic press, London, 1986).

[68] J. Happel and H. Brenner, *Low Reynolds Number Hydrodynamics* (Englewood Cliffs, New Jersey, 1965).

[69] H. Hasimoto, J. Fluid Mech. **5**, 317 (1959).

[70] H. Hayakawa and K. Ichiki, Phys. Rev. E **51**, R3851 (1995).

[71] X. He and L.-S. Luo, Phys. Rev E **55**, 6333 (1997).

[72] B. Herzhaft, E. Guazzelli, M. B. Mackaplow, and E. S. G. Shaqfeh, Phys. Rev. Lett. **77**, 290 (1996).

[73] B. Herzhaft and E. Guazzelli, J. Fluid Mech. **384**, 133 (1999).

[74] E. J. Hinch, in *Disorder and Mixing* edited by E. Guyon, J.-P. Nadal, and Y. Pomeau (Kluwer Academic, Dordrecht, 1988).

[75] T. Hjelt, I. Vattulainen, T. Ala-Nissila, and S. C. Ying, Surf. Sci. **449**, L255 (2000).

[76] K. Höfler and S. Schwarzer, Phys. Rev. E **61**, 7148 (2000).

[77] K. Höfler, *Simulation and Modeling Mono- and Bidisperse suspensions,* Ph.D. thesis, University of Stuttgart (2000).

[78] P. J. Hoogerbrugge and J. M. V. A. Koelman, Europhys. Lett. **19**, 155 (1992).

[79] M. Hoyos, J. C. Bacri, J. Martin, and D. Salin, Phys. Fluids **6**, 3809 (1994).

[80] H. H. Hu, D. D. Joseph, and M. J. Crochet, Theoret. Comput. Fluid Dynam. **3**, 285 (1992).

[81] H. H. Hu, Int. J. Multiphase Flow **22**, 335 (1996).

[82] W. T. Hung, A. F. Collings, and J. Low, Phys. Med. Biol. **39**, 1855 (1994).

[83] K. Ichiki and H. Hayakawa, Phys. Rev. E **52**, 658 (1995).

[84] T. Ihle and D. M. Kroll, Phys. Rev. E **67**, 066706 (2003).

[85] R. Jackson, in *Fluidization,* edited by D. Harrison, J. F. Davidson, and R. Clift (Academic press, London, 1985).

[86] D. J. Jeffrey and Y. Onishi, J. Fluid Mech. **139**, 261 (1984).

[87] A. A. Johnson and T. E. Tezduyar, Comput. Methods Appl. Mech. Engrg. **119**, 73 (1994).

[88] A. A. Johnson and T. E. Tezduyar, Int. J. Num. Meth. Fluids **24**, 1321 (1997).

[89] A. A. Johnson and T. E. Tezduyar, Comput. Methods Appl. Mech. Engrg. **145**, 301 (1997).

[90] A. A. Johnson and T. E. Tezduyar, Comput. Mech. **23**, 130 (1999).

[91] G. E. Karniadakis and S. J. Sherwin, *Spectral/hp Element Methods for CFD* (Oxford University Press, New York Oxford, 1999).

[92] M. Karttunen, I. Vattulainen, and A. Lukkarinen (eds.), *Novel Methods in Soft Matter Simulations*, Lecture Notes in Physics **640** (Springer-Verlag, Berlin Heidelberg, 2004).

[93] S. Kim and S. J. Karrila, *Microhydrodynamics: Principles and Selected Applications* (Butterworth-Heinemann, Boston, 1991).

[94] D. L. Koch and E. S. G. Shaqfeh, J. Fluid Mech. **209**, 521 (1989).

[95] D. L. Koch and E. S. G. Shaqfeh, J. Fluid Mech. **224**, 275 (1991).

[96] D. L. Koch, Phys. Fluids A **5**, 1141 (1993).

[97] D. L. Koch, Phys. Fluids **6**, 2894 (1994).

[98] P. Kumar and B. V. Ramarao, Chem. Eng. Comm. **108**, 381 (1991).

[99] P. B. S. Kumar and M. Rao, Phys. Rev. Lett. **77**, 1067 (1996).

[100] M. L. Kurnaz and J. V. Maher, Phys. Rev. E **53**, 978 (1996).

[101] E. Kuusela, *Microscopic Dynamics of Sedimentation*, Master's thesis, University of Helsinki (1997).

[102] A. J. C. Ladd, J. Chem. Phys. **88**, 5051 (1988).

[103] A. J. C. Ladd, J. Chem. Phys. **93**, 3484 (1990).

[104] A. J. C. Ladd, Phys. Fluids A **5**, 299 (1993).

[105] A. J. C. Ladd, Phys. Rev. Lett. **70**, 1339 (1993).

[106] A. J. C. Ladd, J. Fluid Mech. **271**, 285 (1994).

[107] A. J. C. Ladd, Phys. Rev. Lett. **76**, 1392 (1996).

[108] A. J. C. Ladd, Phys. Fluids **9**, 491 (1997).

[109] A. J. C. Ladd and R. Verberg, J. Stat. Phys. **104**, 1191 (2001).

[110] A. J. C. Ladd, Phys. Rev. Lett. **88**, 048301 (2002).

[111] H. Lamb, *Hydrodynamics,* 2nd edition (Dover, New York, 1945).

[112] L. D. Landau and E. M. Lifshitz, *Fluid Mechanics,* 2nd edition (Butterworth-Heinemann, Oxford, 1987).

[113] X. Lei, B. J. Ackerson, and P. Tong, Phys. Rev. Lett. **86**, 3300 (2001).

[114] A. Levine, S. Ramaswamy, E. Frey, and R. Bruinsma, Phys. Rev. Lett. **81**, 5944 (1998).

[115] N. Liron and S. Mochon, J. Eng. Math. **10** 287 (1975).

[116] C. P. Lowe, Europhys. Lett. **47**, 145 (1999).

[117] J. H. C. Luke, Phys. Fluids **12**, 1619 (2000).

[118] M. Mackaplow and E. Shaqfeh, J. Fluid Mech.

[119] A. Malevanets and R. Kapral, J. Chem. Phys. **112**, 7260 (2000).

[120] M. Mareschal, M. M. Mansour, A. Puhl, and E. Kestemont, Phys. Rev. Lett. **61**, 2550 (1988).

[121] M. R. Maxey, B. K. Patel, E. J. Chang, and L.-P. Wang, Fluid Dyn. Res. **20**, 143 (1997).

[122] P. Mazur and W. Van Saarloos, Physica A **115**, 21 (1982).

[123] K. V. McCloud, M. L. Kurnaz, and J. V. Maher, Phys. Rev. E **56**, 5768 (1997).

[124] K. V. McCloud U. Cardak, and M. L. Kurnaz, and J. V. Maher, e-print, cond-mat/0408473.

[125] J. B. McLaughlin, J. Fluid Mech. **224**, 261 (1991).

[126] M.-C. Miguel and R. Pastor-Satorras, Europhys. Lett. **54**, 45 (2001).

[127] P. J. Mucha, S.-Y. Tee, D. A. Weitz, B. I. Shraiman, and M. P. Brenner, J. Fluid Mech. **501**, 71 (2004).

[128] Y. Nakayama and R. Yamamoto, e-print, cond-mat/0403014.

[129] N.-Q. Nguyen, A. J. C. Ladd, Phys. Rev. E **69**, 050401(R) (2004).

[130] H. Nicolai and E. Guazzelli, Phys. Fluids **7**, 3 (1995).

[131] H. Nicolai, B. Herzhaft, E. J. Hicnh, L. Oger, and E. Guazzelli, Phys. Fluids **7**, 12 (1995).

[132] T.-W. Pan, R. Glowinski, and G. P. Galdi, J. Comput. Appl. Math. **149**, 71 (2002).

[133] T.-W. Pan, D. D. Joseph, R. Bai, R. Glowinski, and V. Sarin, J. Fluid Mech. **451**, 169 (2002).

[134] N. A. Patankar, Int. J. Multiphase Flow **28**, 409 (2002).

[135] J. K. Percus and G. J. Yevick, Phys. Rev. **110**, 1 (1958).

[136] J. W. Perram and M. S. Wertheim, J. Chem. Phys. **58**, 409 (1985).

[137] J. W. Perram, J. Rasmussen, E. Præstgaard, and J. L. Lebowitz, Phys. Rev. E **54**, 6565 (1996).

[138] R. Peyret and T. D. Taylor, *Computational Methods for Fluid Flow* Springer Series in Computational Physics (Springer, Berlin, 1983).

[139] Y. Peysson and E. Guazzelli, Phys. Fluids **10**, 44 (1998).

[140] Y. Peysson and E. Guazzelli, Phys. Fluids **11**, 1953 (1999).

[141] O. Pinkus and B. Sternlicht, *Lubrication theory* (McGraw-Hill,New York, 1961).

[142] C. Pozrikidis, *Introduction to Theoretical and Computational Fluid Dynamics* (Oxford University Press, New York, 1997).

[143] C. Pozrikidis, J. Comput. Phys. **156**, 360 (1999).

[144] S. A. Orszag and V. Yakhot, Phys. Rev. Lett. **56**, 1691 (1986).

[145] D. Qi, J. Fluid Mech. **385**, 41 (1999).

[146] D. Qi, Int. J. Multiphase Flow **26**, 421 (2000).

[147] D. Qi, Int. J. Multiphase Flow **27**, 107 (2001).

[148] S. Ramaswamy, Adv. Phys. **51**, 297 (2001).

[149] D. C. Rapaport and E. Clementi, Phys. Rev. Lett. **57**, 695 (1986).

[150] L. E. Reich, *A Modern Course in Statistical Physics,* 2nd edition (Wiley Interscience, New York, 1998).

[151] M. Revenga, I. Zúñiga, and P. Español, Comput. Phys. Commun. **121-122**, 309 (1999).

[152] J. F. Richardson and W. N. Zaki, Trans. Inst. Chem. Eng. **32**, 35 (1954).

[153] J. Rotne and S. Prager, J. Chem. Phys. **50**, 4831 (1969).

[154] F. Rouyer, J. Martin, and D. Salin, Phys. Rev. Lett. **83**, 1058 (1999).

[155] S. Schwarzer, Phys. Rev. E **52**, 6461 (1995).

[156] P. N. Segrè, E. Herbolzheimer, and P. M. Chaikin, Phys. Rev. Lett. **79**, 2574 (1997).

[157] P. N. Segrè, F. Liu, P. Umbanhower, and D. A. Weitz, Nature **409**, 594 (2001).

[158] P. N. Segrè, Phys. Rev. Lett. **89**, 254503 (2002).

[159] A. Sierou and J. Brady, J. Fluid Mech. **448**, 115 (2001).

[160] T. Soddemann, B. Dünweg, and K. Kremer, Phys. Rev. E **68**, 046702 (2003).

[161] H. Tanaka and T. Araki, Phys. Rev. Lett. **85**, 1338 (2000).

[162] S. Y. Tee, P. J. Mucha, L. Cipelletti, S. Manley, M. P. Brenner, P. N. Segrè, and D. A. Weitz, Phys. Rev. Lett. **89**, 054501 (2002).

[163] A. Tiehm, V. Herwig, and U. Neis, Wat. Sci. Tech. **39**, 99 (1999).

[164] D. J. Triton, *Physical Fluid Dynamics,* 2nd edition (Clarendon Press, Oxford, 1999).

[165] M. A. Turney, M. K. Cheung, R. L. Powell, and M. J. McCarthy, AIChE J. **41**, 251 (1995).

[166] P. Vasseur and R. G. Cox, J. Fluid Mech. **80**, 561 (1977).

[167] I. Vattulainen, T. Hjelt, T. Ala-Nissila, and S. C. Ying, J. Chem. Phys. **113**, 10284 (2000).

[168] I. Vattulainen, M. Karttunen, G. Besold, and J. M. Polson, J. Chem. Phys. **116**, 3967 (2002).

[169] M. Vergeles, P. Keblinski, J. Koplik, and J. R. Banavar, Phys. Rev. Lett. **75**, 232 (1995).

[170] P. B. Warren, Curr. Opin. Colloid In. **3**, 620 (1998).

[171] Z.-J. Xu and E. E. Michaelides, Int. J. Multiphase Flow **29**, 959 (2003).

[172] J.-Z. Xue, E. Herbolzheimer, M. A. Rutgers, W. B. Russel, and P. M. Chaikin, Phys. Rev. Lett. **69**, 1715 (1992).

[173] S. Yamamoto and T. Matsuoka, J. Chem. Phys. **100**, 3317 (1994).

[174] S. Yamamoto and T. Matsuoka, J. Chem. Phys. **102**, 2254 (1995).

[175] S. C. Ying, I. Vattulainen, J. Merikoski, T. Hjelt, and T. Ala-Nissila, Phys. Rev. B **58**, 2170 (1998).

[176] A. A. Zick and G. M. Homsy, J. Fluid Mech. **115**, 13 (1982).

[177] O. C. Zienkiewicz and R. L. Taylor, *The Finite Element Method; Volume 3: Fluid Dynamics*, 5th edition (Butterworth-Heinemann, Oxford, 2000).

[178] Y. Zimmel , in *Ullmann's Encyclopedia of Industrial Chemistry,* 5th edition, **B1** edited by W. Gerhartz, B. Elvers, M. Ravenscroft, J. F. Rounsaville, and G. Schulz (VCH Publisher, New York, 1988).